

Optics and Quantum Electronics

Academic Staff

Prof. James G. Fujimoto, Prof. Erich P. Ippen, Professor Franz X. Kärtner

Research Staff, Visiting Scientists and Affiliates

Dr. Guoqing Chang, Dr. Yueli Chen, Dr. Yu Chen, Dr. Giovanni Cirimi, Prof. Helder Crespo, Dr. Edilson Falcao-Filho, Dr. Peter Fendel, Dr. Vasileios Gkortsas, Dr. Iwona Gorczynska, Dr. Mikhail Gubin, Dr. Katherine Hall, Prof. T.W. Hansch, Dr. Klaus Hartinger, Dr. Kyung-Han Hong, Dr. R. Holzwarth, Dr. Taegeun Kim, Dr. Florian Loehl, Dr. Frank Ludwig, Prof. Uwe Morgner, Dr. Jeffrey Moses, Dr. Amir Nejadmalayeri, Dr. David Phillips, Dr. Milos Popovic, Dr. Benjamin Potsaid, Dr. Dominik Pudo, Dr. Daniel Ripin, Dr. Luciano Socci, Dr. Hideyuki Sotobayoshi, Dr. Dimitri Tyurikov, Dr. Tobias Wilden, Prof. Ronald Walsworth, Prof. Zhigang Zhang, Dr. Chao Zhou

Graduate Students

Gilberto Abram, Desmond Adler, Andrew Benedick, Siddharth Bhardwaj, Jonathan Birge, Hyunil Byun, David Chao, Jeff Chen, Li-Jin Chen, Jung-Ho Chung, Jonathan Cox, Marcus Dahlem, Umit Demirbas, Yu Gu, Vasileios Gkortsas, Shu-Wei Huang, Anatoly Khilo, Jung-Won Kim, Chien-Jen Lai, Hsiang-Chieh Lee, Duo Li, Jonathan Liu, Jonathan Morse, Ali Motamedi, Marco Ornigotti, William Putnam, Michelle Sander, Hanfei Shen, Aleem Siddiqui, Tsung-Han Tsai

Technical and Support Staff

Dorothy A. Fleischer, Donna L. Gale

Research Areas and Projects

Ultrashort Pulse Laser Technology

1. Overview of Recent Advances in Ultrafast Ti:Sapphire Lasers and Frequency Comb Systems
2. Octave-spanning, Dual-output 2.166 GHz Ti:Sapphire Laser
3. Designing Optimal Dispersive Mirrors by Minimizing Phase Distortion Power
4. High Repetition Rate, 0.5-1.0 GHz, Femtosecond Fiber Lasers
5. Strong Bandwidth and Efficiency Improvements by Passive Pulse Shaping in Cavity-Enhanced OPCPA
6. Generation of Sub 7-fs Pulses at 800 nm from a Blue-pumped Optical Parametric Amplifier at Degeneracy
7. High Repetition Rate Fundamentally Mode-locked Erbium Fiber Ring Laser
8. Single-Mode Diode Pumped Cr:Colquiriite Lasers
9. MW Peak Powers from Femtosecond Cr:Colquiriite Lasers
10. Development of GHz Repetition Rate Cr:Colquiriite Lasers

Femtosecond Laser Frequency Combs, Optical Clocks and Phase Control

11. Dynamics of Octave-Spanning Titanium: Sapphire Lasers
12. HeNe-CH₄ based Frequency Combs and Clocks Based on an Octave Spanning 1GHz Ti:sapphire Oscillator
13. Blue Astro-Comb for Precision Calibration of Astrophysical Spectrographs
14. High Power High-Repetition-Rate Femtosecond Fiber Amplifier Development
15. Erbium Fiber Laser Repetition Rate Lock to a Methane-Stabilized HeNe Reference
16. Long Term, Ultrafast, Fiber Optic Timing Distribution with Polarization Maintaining Output

Ultrafast Phenomena and Quantum Electronics

17. Spatial Hole Burning in Actively Mode-locked Quantum Cascade Lasers
18. Ultrafast Nonlinearities in Proton-bombarded InGaAs/GaAs Saturable Bragg Reflectors

Attosecond Science

- 19. Broadband Optical Parametric Chirped Pulse Amplification
- 20. Temporal Optimization of Ultrabroadband Optical Parametric Chirped Pulse Amplification
- 21. High-average-power Picosecond Green Laser Based on a Frequency-doubled Hybrid Cryogenic Yb:YAG Amplifier
- 22. Conversion Efficiency Scaling of High Harmonic Generation

Attosecond Photonics

- 23. Attosecond-Timing-Precision Photonics
- 24. Attosecond Resolution Timing Jitter Measurements with Periodically Poled KTP Waveguides
- 25. High-Speed Silicon Electro-Optic Mach-Zender Modulators
- 26. Silicon Microring Resonator Filter Banks for Photonic Analog-To-Digital Conversion

Nanophotonics

- 27. Design of Silicon Photonic Microcavities for Optical Switching
- 28. Post-Fabrication Thermal Trimming of an Eleven-Channel Second-Order Silicon Microring Resonator Filterbank

Frequency Swept Lasers

- 29. Frequency Swept Lasers and Fourier Domain Mode Locking (FDML)

Ultrashort Pulse Laser Technology

Overview of Recent Advances in Ultrafast Ti:Sapphire Lasers and Frequency Comb Systems

Sponsors

Office of Naval Research (ONR), Contract N00014-02-1-0717
 Air Force Office of Scientific Research (AFOSR), FA9550-07-1-0014
 Sandia National Laboratories, Contract 777117

Project Staff

Andrew Benedict, Li-Jin Chen, Dr. Noah Chang, Jonathan Birge, Michelle Sander and Professor Franz X. Kärtner

Ultrafast Ti:Sapphire lasers continue to be an important research area especially with the recent emergence of applications to high harmonic generation, astronomical spectrograph calibration and two photon microscopy to name only a few. Supporting these applications, Prof. Kärtner's group has produced several important results over the past year, with the following paragraphs serving to highlight these results.

Work on the 1-GHz Ti:Sapphire frequency comb and clock has culminated this past year with a high precision measurement of the Allan Deviation of the frequency comb's output spectrum [1]. The system uses a methane stabilized HeNe laser as its absolute frequency reference to generate a broadband absolute frequency source with a bandwidth exceeding one octave. The Allan deviation measurement has shown that the stability of the reference laser was completely transferred to all lines of the Ti:Sapphire comb resulting in a measured frequency stability of 3×10^{-14} in a 20 s measurement period. This result is complimented by the extremely low pulse repetition rate phase noise of the system which was measured to be less than 10 fs when integrated over a 0.02 s period. These results are made all the more appealing by the relatively compact size of the frequency comb system which could be collapsed into a 2 m³ volume with a minimum of engineering. This device now stands ready to assist our community in evaluating other systems developed at MIT.

Complimenting the results of the 1-GHz Ti:Sapphire comb and clock is a carrier envelope phase stabilized 2-GHz laser [2]. This laser is unique thanks to its next generation double chirped dispersion compensating mirrors (DCMs) and because it has the highest pulse repetition rate to date with an octave spanning spectrum. The DCMs are unique since they are designed to allow the central pulse forming portion of the spectrum to circulate in the laser cavity, yet they allow the portions of the laser spectrum used for f-2f self referencing to leak out past the mirror surface. This results in a carrier envelope stabilized laser with an output beam which is undistorted by beam splitters. Another strong attribute of this system is the laser's large output power and high pulse repetition rate which combine to give a power per line of more than 200 nW over a bandwidth of more than 400 nm.

In our quest to find the limits of octave spanning operation of Ti:Sapphire lasers, work has begun on a 10-GHz laser [3] similar to the two previous lasers. The current approach is to continue with a ring laser topology using DCM mirrors. Initial results include narrowband mode locking with more than 250 mW output power. The promise of this laser is for it to be simply a small box that is placed at the output of a pump laser and functions as a "frequency conversion" device, shifting the single frequency pump laser to a broadband output centered near 800nm.

One of the initial applications for the 10-GHz laser will be for use in an Astro-Comb [4]. As reported last year, using frequency combs to calibrate astronomical spectrographs is a natural application of the frequency comb's strengths. However, the mode spacing of most frequency combs is not coarse enough to be resolved by astronomical spectrographs, so mode filtering is necessary to artificially increase the mode spacing to turn a frequency comb into an Astro-Comb.

Last year the first laboratory demonstration of an Astro-Comb was made using the direct output from the 1-GHz Ti:Sapphire laser. This year we have frequency doubled the output spectrum of the 1-GHz Ti:Sapphire laser and have optimized the system design based on experience gained from the first demonstration. The initial results from this short wavelength Astro-Comb show both good side mode suppression and low dispersion of the filter cavity, both characteristics being necessary for high precision spectrograph calibration. Further, a system identical to that reported last year has been installed at the Fred Lawrence Whipple Observatory on Mt. Hopkins in Arizona to test the viability of such a system as installed in a real observatory. Initial reports from that experiment shows good system stability and operability as well as spectrograph calibration capability exceeding that of the installed spectrograph.

None of these lasers or frequency comb systems would be possible without careful design of the dispersion compensating mirrors. Over this past year a new algorithm has been developed which enables a more intuitive design process for the DCMs. Previous methods for designing DCMs involved iterating mirror designs for minimization of the group delay dispersion (GDD) with the underlying assumption that minimizing this quantity would reduce the energy removed from a pulse upon reflection from a mirror. This is important because pulse energy is related to the saturable absorber action which controls the Kerr lens mode locking mechanism. As discussed in this year's annual report, a method for directly defining the effect of GDD in terms of pulse energy has been derived [5]. This new algorithm has also been numerically demonstrated to design mirrors which give much lower losses per reflection than mirror designs that merely minimize GDD. Based on this success, actual coatings based on this process are being designed and are expected to be available for testing by the end of the year.

Finally, work on understanding the mechanisms which control the carrier envelope phase (CEP) in Ti:Sapphire lasers has also been completed [6]. The CEP is an important parameter for both time domain and frequency domain applications. Control of the CEP is usually achieved by amplitude modulation of the Ti:Sapphire pump laser, which results in a shift in the CEP. As demonstrated in this year's annual report, we conducted numerical evaluations for the laser cavity, which was modeled with gain saturation, self-phase modulation, saturable absorber action, higher order dispersive terms and measured transfer functions for the dispersion compensating cavity mirrors, to study the temporal and spectral dynamics of these lasers. This model was then extended to investigate the impact of self-steepening on the pulse shaping mechanism and the carrier-envelope phase dynamics. The result is a numerical model which gives good agreement with experimental measurements of the coupling between pump power and CEP shift paving the way for even more detailed design of future laser systems.

References

1. A. Benedick, D. Tyurikov, M. Gubin, R. Shewmon, I. Chuang, and F. X. Kärtner, "Compact, Ti:sapphire-based, methane-stabilized optical molecular frequency comb and clock," *Opt. Lett.* 34(14): 2168-2170 (2009).
2. L.-J. Chen, A. J. Benedick, J. R. Birge, M. Y. Sander, and F. Kärtner, "Octave-spanning, dual-output 2.166 GHz Ti:sapphire laser," *Opt. Express* 16(25): 20699-20705 (2008).
3. A. Bartels, D. Heinecke, and S. A. Diddams, "Passively mode-locked 10 GHz femtosecond Ti:sapphire laser," *Opt. Lett.* 33(16): 1905-1907 (2008).
4. C.-H. Li, A. J. Benedick, P. Fendel, A. G. Glenday, F. X. Kartner, D. F. Phillips, D. Sasselov, A. Szentgyorgyi, and R. L. Walsworth, "A laser frequency comb that enables radial velocity measurements with a precision of 1 cm s⁻¹," *Nature* 452(7187): 610-612 (2008).
5. J. R. Birge and F. X. Kartner, "Design of Optimal Dispersive Mirrors for Femtosecond Enhancement Cavities and Compressors by Minimizing Phase Distortion Power," in *Conference on Lasers and Electro-Optics/International Quantum Electronics Conference*, OSA Technical Digest (CD) (Optical Society of America, 2009), CThDD1.
6. M. Y. Sander and F. X. Kartner, "Carrier-Envelope Phase Dynamics of Octave-Spanning Titanium:Sapphire Lasers," in *Conference on Lasers and Electro-Optics/International Quantum Electronics Conference*, OSA Technical Digest (CD) (Optical Society of America, 2009), CMN4.

Octave-spanning, Dual-output 2.166 GHz Ti:sapphire Laser

Sponsors

Defense Advanced Research Projects Agency (DARPA), HR0011-05-C-0155
Air Force Office of Scientific Research (AFOSR), FA9550-07-1-0014

Project Staff

Li-Jin Chen, Andrew Benedick, Jonathon R. Birge, Michelle Y. Sander, and Prof. Franz X. Kärtner

Optical frequency combs and pulse trains from self-referenced laser oscillators are versatile tools for stable and accurate measurements in frequency metrology, optical arbitrary waveform generation (OAWG) [1] and calibration of astronomical spectrographs [2]. To enable more compact and powerful frequency comb systems, ultra-broadband laser oscillators operating at high repetition rates are highly desirable. In this work, a self-referenced octave-spanning Ti:sapphire laser with a repetition rate of >2 GHz is demonstrated while maintaining a CE beat note of >50 dB measured with a 100-kHz RBW, which shows to our knowledge both the highest repetition rate and ~ 20 dB improvement (using 100-kHz RBW) of the CE beat note for a gigahertz-repetition-rate phase-stabilized laser oscillator.

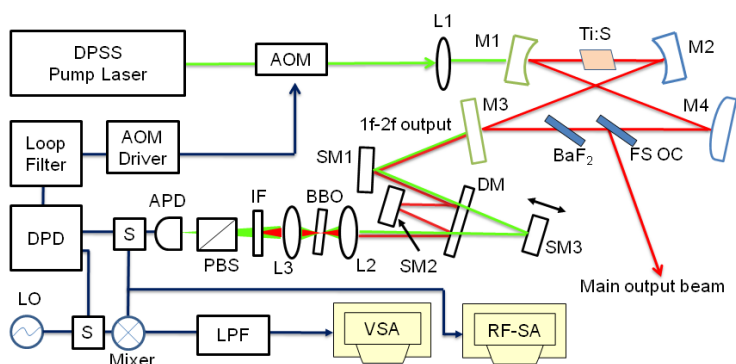


Figure 1: Setup of the CE phase-stabilized 2.166-GHz Ti:sapphire laser.

The laser and 1f-2f interferometer setup are shown in Fig. 1. We use a 4-mirror Kerr-lens-mode-locked (KLM) ring cavity consisting of two dispersion-matched pairs of broadband double-chirped mirrors. The DCMs used here are designed to have a smooth average group delay and negative group delay dispersion (GDD) from 650 to 1100 nm to compensate for the positive dispersion of all other intracavity elements in this spectral range of interest. The coating on M3 (same as M1), is designed to transmit 50% of the intracavity power around f and $2f$ components, which allows the main output to be completely separated from the 1f-2f output (coupled out from M3) so that the main pulses are not affected by any extracavity manipulations needed for CE-phase stabilization.

Figure 2 shows the radio-frequency (RF) spectra of the directly detected pulse trains and the optical output spectra. The clean RF-spectrum indicates stable fundamental mode locking with a repetition rate of ~ 2.166 GHz. At 10.5 W of pump power the laser generates a total output power of 812 mW including a main output of 750 mW and a 1f-2f output of 62 mW. For comparison, the calibrated spectra displaying power spectral density for both outputs are shown in the same plot. The spectral components of the 1f-2f output below 600 nm and above 1120 nm, although containing only a few percent of the total power, are stronger than the main output. The power leaving the 1f-2f output port within a 10 nm bandwidth located at 580 nm and 1160 nm, the wavelengths used for the CE-lock, are 0.884 mW and 4.49 mW, respectively, which is more than enough power for subsequent self-referencing. The result matches perfectly with our DCM design and also shows that we can generate the necessary 1f-2f components in a very simple and efficient way without affecting the main output of the laser.

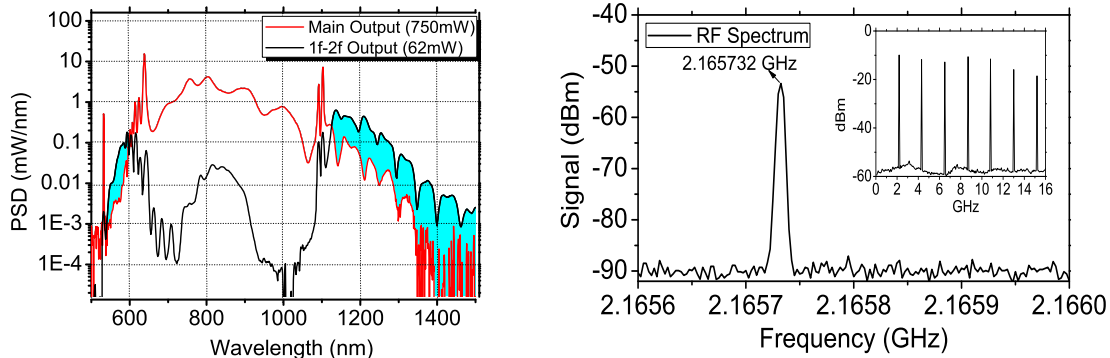


Figure 2: Laser output spectra (left) and RF spectra (right).

The CE-offset frequency (f_{ceo}) is locked to a local oscillator (LO) set at 20 MHz through a phase-locked loop (PLL) (see Fig. 1). The residual phase noise of our system was obtained by splitting the CE-beat note signal and mixing one part of it directly with the local oscillator signal using a broadband analog mixer. The output from the mixer was filtered by a 10-MHz low-pass filter and fed into a vector signal analyzer (VSA) for measuring the one-sided power spectral density (PSD) of the residual CE fluctuations, S_{ϕ} (see red curve in Fig. 3). The accumulated phase error integrated from 0.1 Hz to 1 MHz is 0.187 rad. This is equivalent to a timing jitter of 79 as at the center wavelength of 800 nm, which is slightly better than earlier-constructed Ti:sapphire combs pumped by a multimode laser. Since multimode pump lasers are known to have significantly higher relative intensity noise than single-mode pump lasers at high frequencies, where the feedback loop of the PLL already has low gain for stability reasons or is already outside the loop bandwidth, the CE-phase noise can be further suppressed by switching to a single-frequency pump source.

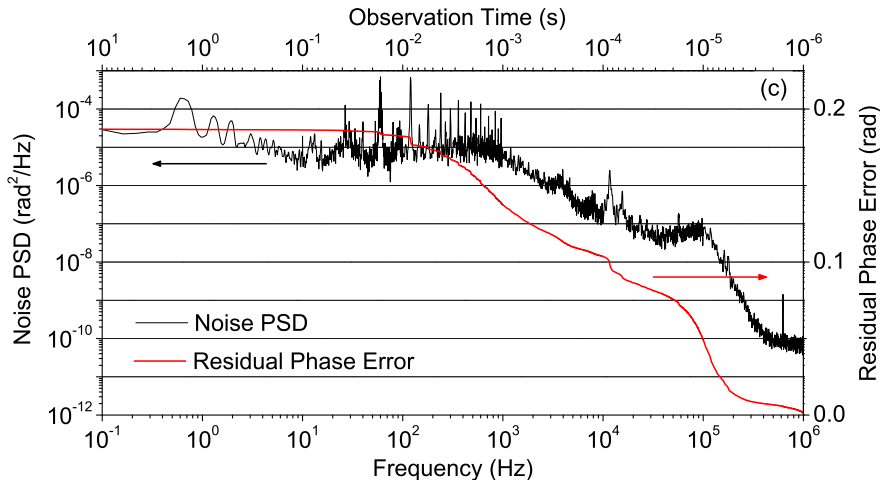


Figure 3: Power spectral density (PSD) of the residual carrier-envelope phase fluctuations (black curve) and integrated carrier-envelope phase error (red curve). The accumulated phase error integrated from 0.1 Hz to 1 MHz is 0.187 rad.

References:

- Z. Jiang, D. E. Leaird, and A. M. Weiner, "Line-by-line pulse shaping control for optical arbitrary waveform generation," *Opt. Express* 13, 10431-10439 (2005).
- C.H. Li, A. Benedick, P. Fendel, A.G. Glenday, F.X. Kartner, D.F. Phillips, D. Sasselov, A. Szentgyorgyi, and R.L. Walsworth, "A laser frequency comb that enables radial velocity measurements with a precision of 1 cm s⁽⁻¹⁾," *Nature* 452, 610-612 (2008).

Designing Optimal Dispersive Mirrors by Minimizing Phase Distortion Power

Sponsors

Air Force Office of Scientific Research (AFOSR), FA9550-07-1-0014

Project Staff

Jonathan Birge and Professor Franz X. Kärtner

Typically, phase sensitive mirrors (and, in fact, most phase sensitive optical devices, for that matter) have been designed by seeking to minimize the spectrally integrated deviation of the group delay dispersion (GDD) from the GDD desired. While this technique works adequately for small relative bandwidths (the domain in which the concept of GDD first arose), where a second-order series expansion of phase is valid, it does not always yield optimal results with the kinds of large relative bandwidths accessible with modern mode-locked laser systems.

To be specific, a minimum integrated GDD design is not necessarily optimal when the phase imparted upon reflection has oscillations whose period is shorter than the pulse bandwidth. Such oscillations are caused by light that is dispersed well away from the main reflected pulse. As shown by Steinmeyer [1], the amplitude of such GDD oscillations is proportional to the square of the delay between these so-called “satellite pulses” and the main pulse. In the majority of ultrafast optics applications, however, the timing of such satellite pulses is irrelevant; what matters is the power contained in them.

In lieu of mean squared GDD, we propose a new criterion based on the fractional energy lost to phase distortions. We introduce a new spectral parameter, which we will refer to as the phase distortion ratio (PDR):

$$\text{PDR}(\omega) \equiv m^2 \left[\Delta\phi(\omega) - \frac{\Delta\omega^2 + \omega_0^2 - \omega\omega_0}{\Delta\omega^2} \langle \Delta\phi \rangle + \frac{\omega - \omega_0}{\Delta\omega^2} \langle \omega \Delta\phi \rangle \right]^2 \quad (1)$$

where $\Delta\omega$ is the pulse bandwidth, ω_0 the center (mean) frequency, and $\Delta\phi$ the raw computed phase error. The angle brackets denote an optical power weighted mean. Multiplying $\text{PDR}(\omega)$ by the incoming power spectral density and integrating yields the total optical power contained in phase distortions. The complexity of the expression is due to the need to take out an arbitrary constant and linear phase from the raw phase error. Having a closed form expression for the PDR (as opposed to leaving floating phase terms) allows for highly efficient numerical optimization using analytic gradients. In practice, computing the gradient of the PDR is at least 2-4 times faster than working with GDD [3].

For relatively narrow relative bandwidths, less than 1/10, enhancement cavities can be designed for low dispersion by using mirrors based on Bragg stacks. To progress beyond that, however, enhancement cavities with chirped mirrors will have to be used, with intracavity positive dispersion elements introduced. Given the extreme sensitivity of wide bandwidth cavities to resonance shifts, proper design of the mirrors will be imperative to successful implementation, and the performance of the mirrors will be the limiting factor to bandwidth.

Assuming the reflectivity of the mirrors maintains a sufficient cavity Q for field enhancement and/or mode suppression, the dominant mechanism affecting the cavity throughput will be the detuning of cavity resonances due to mirror dispersion imperfection. To second-order, the spectral transmission of a comb through a locked cavity can be shown to be equal to

$$T(\omega) = 1 - \frac{R(\omega)}{[1 - R(\omega)]^2} \text{PDR}(\omega) + O[\text{PDR}^2(\omega)]. \quad (2)$$

An optimal design approach is thus to minimize the power weighted mean PDR of the mirror, subject to the constraint that the mirror reflectivity stays within a band such that sufficient cavity Q is maintained.

To demonstrate the efficacy of PDR optimization of cavity mirrors, we considered the case of an ultra-broadband rate enhancement cavity with a modest Q factor of 400, created by two identical (i.e. non complementary) chirped mirrors. The cavity was assumed to have roughly 100 fs^2 of internal dispersion. Such a cavity would be useful for increasing the mode spacing of a femtosecond comb for high precision astrophysical spectroscopy, as in [2].

First, a double chirped mirror was designed using the standard GDD optimization approach [3]. This mirror was then reoptimized using the criterion in (2), starting from the minimum GDD design to be absolutely fair. These two designs are compared in Fig. 1 left, where it is clear that the GDD optimized design (black) has less GDD ripple than the minimum PDR design (gray), as one would expect.

The theoretical cavity transmission (assuming perfect cavity locking) is shown in Fig. 1 right. Despite the apparent lower dispersion ripple of the GDD optimized mirror, it is virtually useless in the cavity, admitting only a few nanometers of bandwidth before the mirrors dephase the cavity from the comb. The PDR optimized cavity, however, transmits an average of at least 90% over the entire 400-nm bandwidth. Moreover, there is significant room left for improvement in bandwidth and/or Q factor through the use of complementary chirped mirror pairs.

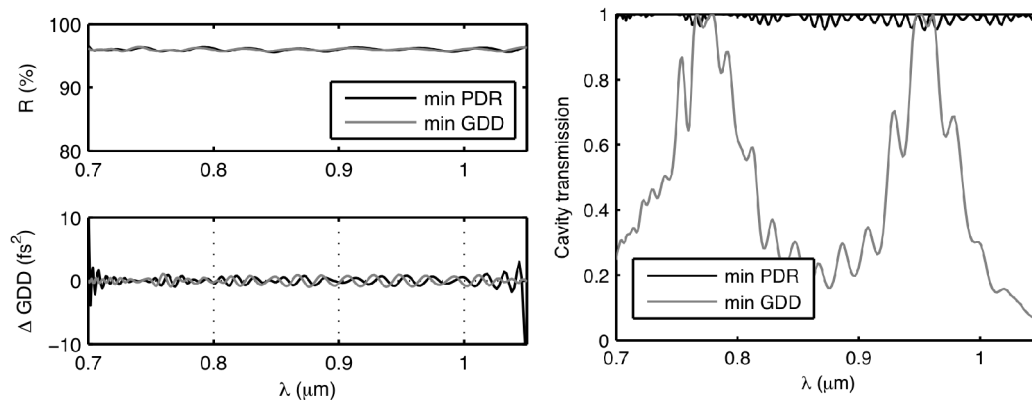


Figure 1: Left: Group delay dispersion of PDR-optimized and standard GDD-minimized filter cavity mirror. Right: Cavity transmission of both mirrors, showing the markedly superior performance of the PDR-designed mirror despite its apparently worse dispersion.

References

1. G. Steinmeyer, "Dispersion oscillations in ultrafast phase-correction devices," *IEEE JQE* **39**, 1027-1034 (2003).
2. C.-H. Li, A. Benedick, P. Fendel, A. Glenday, F. X. Kärtner, D. Phillips, D. Sasselov, A. Szentgyorgyi, and R. Walsworth, "A laser frequency comb that enables radial velocity measurements with a precision of 1 cm s^{-1} ," *Nature* **452**, 610-612 (2008).
3. J. R. Birge and F. X. Kärtner, "Efficient optimization of multilayer coatings for ultrafast optics using analytic gradients of dispersion," *Appl. Opt.* **46**, 2656-2662 (2007).

High repetition rate, 0.5 – 1.0 GHz, femtosecond fiber lasers

Sponsors

DARPA/OAWG HR0011-05-C-0155
DARPA/EPIC W911NF-04-1-0431

Project Staff

Hyunil Byun, Dominik Pudo, Jian Chen, Michelle Sander, Jonathan Morse, Erich P. Ippen, and Franz X. Kärtner

Compact, high repetition rate sources of femtosecond laser pulses are required for a variety of applications, such as frequency metrology [1] and ultrafast sampling [2]. Passive mode-locking enables low-jitter femtosecond pulses and alleviates the need for an optical modulator and low-noise electronic microwave driver. In this report, we demonstrate a simple, inexpensive and low-jitter passively mode-locked femtosecond erbium-doped fiber (EDF) laser using saturable Bragg reflectors (SBRs) at two different repetition rates, 500 MHz and 1 GHz.

1. 500-MHz femtosecond laser [3]

The experimental setup is depicted in Fig. 1 (a). The laser cavity consists of a 20.7-cm section of EDF with group-velocity dispersion (GVD) of $-20 \text{ fs}^2/\text{mm}$. Using an anomalously-dispersive gain fiber eliminates the need for an additional fiber section for dispersion compensation, which would reduce the repetition rate. One end of the cavity is butt-coupled to an SBR, and the other to a dielectric mirror, which acts as the output coupler (OC). The SBR is a commercial unit with 6% modulation depth, 2-ps recovery time and dispersion of $+1000 \text{ fs}^2$ around the operation wavelength. Pump light is provided by a 980-nm laser diode, free-space coupled through a dichroic beamsplitter and focused by an aspheric lens through the output coupler and into the EDF. The output coupler transmits 10% of intracavity power over the wavelength range from 1520 nm to 1640nm with negligible dispersion. The output signal follows the same path in reverse and is separated from the pump by the dichroic beamsplitter.

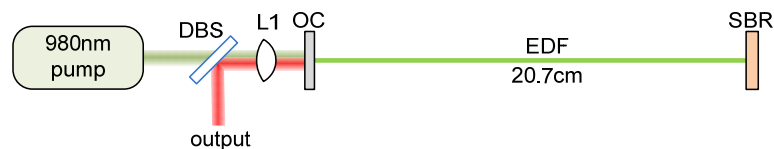


Fig. 1. Experimental setup for the 500-MHz linear soliton laser: DBS, dichroic beam splitter, OC, output coupler, EDF, Er-doped fiber

Fig. 2 (a) and (b) depict the measured optical spectrum and interferometric nonlinear autocorrelation trace (IAC). The optical spectrum analyzer measurement shows a 15.4-nm FWHM optical bandwidth, implying a 168-fs transform-limited FWHM pulse duration, while the autocorrelation measurement results in a 180-fs FWHM duration. The difference is attributed to the non-uniform gain profile of the EDF and the non-uniform dispersion profile of the SBR, causing a slight deviation of the measured optical spectrum from a sech^2 spectrum, as shown in Fig. 2 (a). The above values were obtained with 260 mW of cavity coupled pump power; the intracavity signal power was measured to be 121 mW, which corresponds to 251-pJ intracavity pulse energy. Fig. 2 (c) and (d) shows the radio-frequency (RF) spectrum and single side band (SSB) phase noise. The 60 dB RF signal-to-background ratio, see Fig. 2 (c), indicates excellent energy stability. Fig. 2 (d) shows the SSB phase noise of the fourth harmonic (1.963 GHz) of the laser. The timing jitter integrated from 10 MHz progressively down to 1 kHz is also shown. Over that full interval the net jitter is 20 fs. The phase noise below 1 kHz that follows a slope of -20 dBc/dec can be suppressed by controlling the fiber length with a piezo-based stretcher and locking the rep rate to an electronic oscillator with better long-term stability. The bandwidth

limitations of this approach will likely limit such suppression of phase noise to frequencies below ~ 10 kHz.

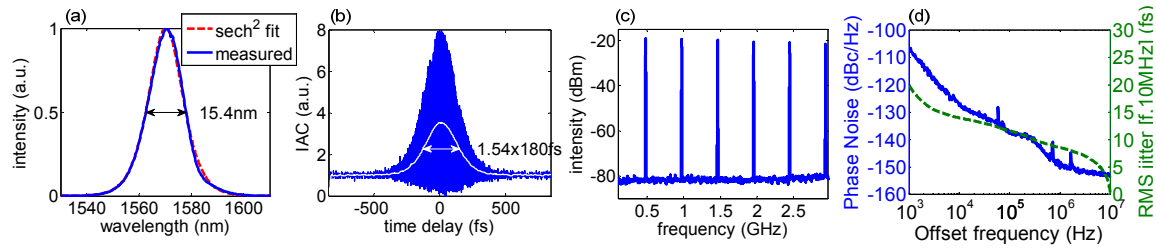


Fig. 2. The measurement results of the 500-MHz EDF laser. (a) Optical spectrum, (b) Interferometric auto-correlation with inferred intensity autocorrelation (white), (c) RF spectrum spanning from 0 to 3 GHz with resolution bandwidth of 10 MHz (d) Single-side-band (SSB) phase noise (solid) and integrated RMS jitter (dotted).

2. 1-GHz femtosecond laser

The pulse repetition rate was scaled up by shortening the cavity length by half. However, as the cavity length decreased, thermal damage on the SBR became an issue such that the laser would only run mode locked for several seconds before the SBR damage became large enough to inhibit lasing. Given a same pump power at the OC, the residual pump power at the SBR almost doubles and the EDF core temperatures at the SBR also increases as the cavity length halves. To prevent thermal damage on the SBR, we spliced a 5-mm long single mode fiber (SMF) to the 10-cm long EDF to function as a thermal insulator. In addition, dielectric coatings were deposited on the SBR to reflect the residual pump power. With the SMF and the coating, the mode-locking operation time significantly increased from only several seconds to several minutes. Fig. 3 describes the setup schematic, measured optical spectrum and RF spectrum, which were taken with a coupled pump power of 230 mW. The output power was 8.8 mW at a repetition rate of 986 MHz, corresponding to 90-pJ intracavity pulse energy with an optical spectrum of 6.2 nm FWHM, which is narrower than the 500-MHz laser proportionally with the pulse energy.

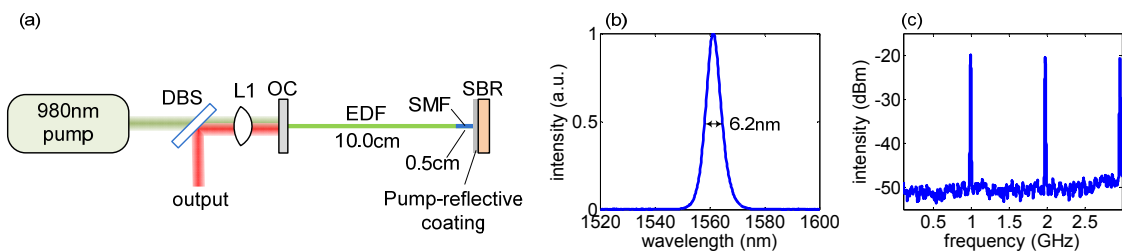


Fig. 3. (a) Experimental setup for the 1-GHz linear soliton laser: SMF, single mode fiber. (b) measured optical spectrum (c) measured RF spectrum.

References

- [1] S. T. Cundiff, "Metrology - New generation of combs," *Nature* 450: 1175-1176 (2007).
- [2] A. Bartels, et al., "Ultrafast time-domain spectroscopy based on high-speed asynchronous optical sampling," *Review of Scientific Instruments* 78(3): 035107 (2007).
- [3] H. Byun, D. Pudo, J. Chen, E.P. Ippen and F.X. Kärtner, "High repetition rate, 491 MHz, femtosecond fiber laser with low timing jitter," *Opt. Lett.*, 33(19): 2221-2223 (2008).

Strong Bandwidth and Efficiency Improvement by Passive Pulse Shaping in Cavity-Enhanced OPCPA

Sponsors

DARPA/OAWG HR0011-05-C-0155

NDSEG - Fellowship

Project Staff

Aleem M. Siddiqui, Dr. Jeffrey Moses, Dr. Kyung-Han Hong, and Professor Franz X. Kärtner

Optical parametric chirped pulse amplification (OPCPA) has emerged as a competitive means for providing the high-power, few-cycle laser sources in the near- and mid- infrared required for high-field laser science. OPCPA allows the direct transfer of energy from a high-power, narrow-band pump source to a broadband signal source via a nonlinear crystal, with typical conversion efficiencies in the 10-20% range for few-cycle signal pulses. The conversion efficiencies are limited by temporal and spatial variations in small-signal gain, due to the bell-shaped intensity profiles and time-varying wave-vector mismatch of the interacting pulses.

We show that in cavity-enhanced OPCPA (c-OPCPA), proposed earlier as a means for storing and recycling pump light in OPCPA [1], the enhancement cavity naturally reshapes the pump pulses for optimal conversion efficiency, even for signal bandwidths exceeding the phase-matching bandwidth of the nonlinear medium. Numerical simulations show that near quantum limited efficiencies can be reached, and the gain bandwidth can exceed the single pass case by ~4 times.

In c-OPCPA, a high-Q cavity for the pump wave contains a parametric amplification crystal and allows light at the signal and idler wavelengths to exit, unreflected. Thus, the device is an enhancement cavity for the pump with a nonlinear loss element, since parametric conversion depends on the stored pump intensity. Light unconverted from pump to signal and idler after a pass through the nonlinear crystal remains in the cavity. Thus, temporal regions with low conversion (due to locally low pump intensity and/or large wave-vector mismatch) exhibit lower loss and therefore develop a higher pump intensity that compensates for the initially low gain. Full conversion is achieved if the total cavity loss, $L(t) = L_{linear} + L_n(t)$, equals the transmission coefficient of the cavity input coupler, T , for all t . In this case there is no reflection from the input coupler. Successful impedance matching depends on the initial conditions of the interaction.

We conducted simulations to analyze the behavior of c-OPCPA with matched pump, signal, and cavity repetition rates, with narrowband pump and broadband chirped seed pulses of equal duration. With each round-trip through the cavity, the intracavity pump electric field is modified in amplitude and phase by (1) propagation through the nonlinear crystal, (2) subtraction of fixed linear losses, and (3) combination with the next pump pulse transmitted through the input coupler. The simulation is run until a steady-state intracavity pump power develops.

Figure 1 shows a simulation result for the case of 10-W, 3-ps, transform-limited pump pulses at 1037 nm and 1-mW, 3-ps, chirped signal pulses at 1550 nm with a bandwidth of 100 nm, which mix in a 5-mm PPLN crystal. The repetition rate is 80 MHz. In Fig. 1 (a) the black and red curves are the incident and intracavity pump profiles, respectively. The blue curve is the chirped signal input (scaled by 5000). Fig. 1 (b) shows the fractional conversion of pump to signal as a function of time, with and without an enhancement cavity (red and black curves, respectively). In the single-pass case, which is near optimal, gain narrowing limits the total conversion efficiency to 37%. The resulting bandwidth of the amplified signal is 38 nm at FWHM, slightly larger than the calculated phase-matching bandwidth of the crystal, 24 nm, because of saturation. In comparison, the c-OPCPA case produces a signal pulse with 92-nm bandwidth and 52% conversion efficiency (Fig. 1 (a), red curve). At the center of the pump pulse (coordinate T1) where the wave-vector mismatch ($\Delta K1$) is zero, the pump intensity of the incident pump pulse is already high enough for significant conversion of energy to the signal and the intracavity intensity

builds up to an intensity slightly lower than that of the incident pulse. At coordinates further from the center (T2, T3), the intracavity intensity builds up more strongly, increasing to compensate for the lower small-signal gain due to the significant wave-vector mismatch, and the higher gain necessary for significant pump depletion due to the lower seed intensity. The above results were limited by impedance matching; the overall conversion efficiency can be increased to 71% by lowering the input signal power to 1 μW , allowing a more optimally impedance matched case.

Figure 2 (a) shows simulation results for quasi-monochromatic pump and signal pulses with varying incident seed power. Since gain is proportional to $\exp(I_p^{0.5})$, a small increase in intracavity intensity, requiring a small increase in enhancement, can increase the gain by an order of magnitude. In Fig. 2 (a), good conversion efficiency is obtained for input seed powers ranging 5 orders of magnitude. The highest conversion efficiency of 56% is achieved with $\sim 1 \mu\text{W}$ of signal power, which allows the best impedance matching. The c-OPCPA technique, therefore, is quite flexible. The ability of the cavity to compensate for reduced seed power is ultimately limited by the amount of enhancement available from the cavity.

Figure 2(b) summarizes simulations of c-OPCPA where the seed spectrum lies outside of the phase-matching bandwidth. In each case, the crystal is phase-matched at 1550 nm, with phase-matching bandwidth indicated by the dashed curve. Seed spectra of 10-nm bandwidth are launched at various center wavelengths. The results indicate that good conversion efficiency is possible over a range of wavelengths between 1.5 and 1.7 microns, covering a bandwidth an order of magnitude larger than the crystal phase-matching bandwidth. Currently, experimental efforts are underway to implement the device.

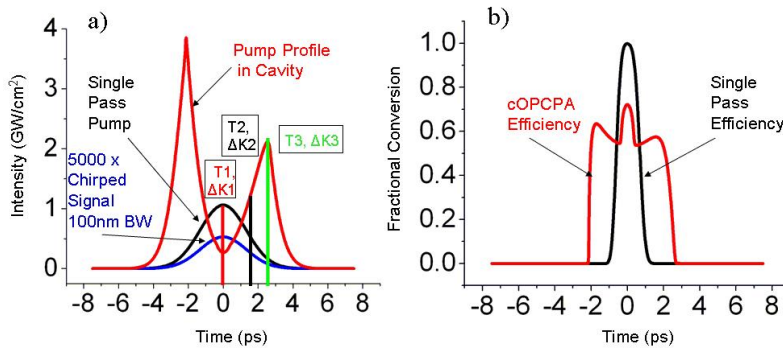


Figure 1: a) Relevant intensity profiles. b) Conversion efficiency across the signal pulse for the c-OPCPA case (wider red curve) and the single pass case (narrower black curve).

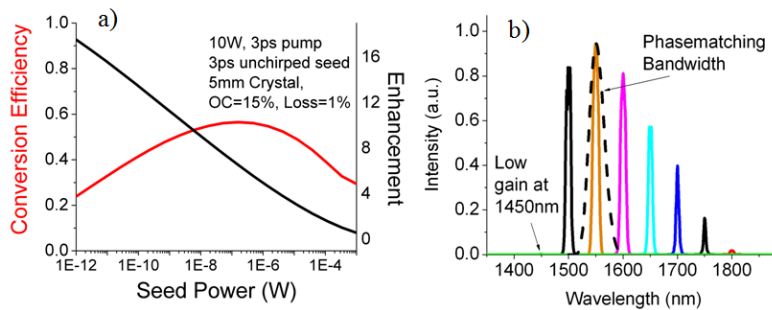


Figure 2: a) Conversion efficiency and enhancement in c-OPCPA as the seed power is varied for a narrowband seed. b) Order-of-magnitude extension of the effective phase-matching bandwidth in c-OPCPA.

References

- [1] F. Ö. Ilday and F. X. Kärtner, "Cavity-enhanced optical parametric chirped-pulse amplification," *Opt. Lett.* **31**, 637 (2006).
- [2] G. Cerullo, S. De Silvestri, "Ultrafast optical parametric amplifiers," *Rev. Sci. Instr.* **74**, 1 (2003).

Generation of Sub 7-fs Pulses at 800 nm from a Blue-pumped Optical Parametric Amplifier at Degeneracy

Sponsors

Progetto Roberto Rocca
DARPA HRS Program via AFOSR FA9550-08-1-0409.

Project Staff

Aleem M. Siddiqui, Dr. Giovanni Cirimi, Daniele Brida, Professor Franz X. Kärtner, and Professor Giulio Cerullo

Optical Parametric Amplifiers (OPAs), thanks to their broad phase-matching bandwidths, allow for dramatic shortening of the duration of the driving pulse. In particular, OPAs pumped by the fundamental frequency (FF) or the second harmonic (SH) of Ti:sapphire and seeded by white-light continuum (WLC) enable the generation of few-optical-cycle pulses in a wide spectral range, from the visible [1] to the near-IR [2]. However, the important spectral range around 800 nm has not yet been covered. In fact, the WLC produced from an 800-nm driving pulse presents a highly structured amplitude and phase profile around the pump frequency. Previous attempts of amplification at 800 nm of a supercontinuum generated in a photonic crystal fiber resulted in ultra-broadband spectra, which were, however, not compressed due to the strong chirp on the seed pulses [3].

In this work, we demonstrate a two-stage OPA scheme for the generation of few-optical-cycle pulses at 800nm starting from a 150-fs amplified Ti:sapphire laser system. First, a FF-pumped near-IR OPA is used to generate either a signal at 1.3 μm or an idler at 1.6 μm , which in turn produces a WLC with well-behaved spectral amplitude and phase around 800 nm. This WLC is then amplified in a broadband degenerate SH-pumped OPA and compressed by chirped mirrors to nearly transform-limited (TL) sub-7-fs duration. We achieve a pulse shortening by a factor of 20 with respect to the driving laser.

Figure 1 depicts the experimental setup. The system starts with an amplified Ti:sapphire laser system producing 150-fs pulses at 1 kHz (Quantronix Integra-C) with less than 0.3% pulse-to-pulse energy fluctuation. A fraction of the pulses is used to drive a two-stage FF-pumped near-IR OPA, employing type II β -barium borate (BBO) crystals and generating signal energies up to 15 μJ tunable from 1.2 to 1.6 μm (corresponding to an idler from 1.6 to 2.4 μm), with rms pulse to pulse fluctuations of 0.5%. This OPA has excellent stability thanks to pump depletion. To facilitate separation of the beams, a slightly non-collinear configuration is used for both OPAs; the non-collinear angle is however kept as small as possible to avoid angular dispersion in the idler beam.

Next, either the signal or the idler (in the latter case after rotating the polarization with a half-wave plate) of the near-IR OPA was used to generate the broadband WLC seed for the SH-pumped degenerate OPA. With the 1.3- μm signal, the WLC was generated in a 3-mm sapphire plate. The SH-pumped degenerate OPA employs a single pass in a 1-mm-thick type I BBO crystal ($\theta=29^\circ$, $\phi=0^\circ$), pumped by 70 μJ of the SH, to amplify the WLC up to 5 μJ . The bandwidth covered the range from 650 to 950 nm. The resulting ultrabroadband spectrum is compressed with 2 bounces on double chirped mirrors with cancelling dispersion ripples and through 1.25 mm of bulk fused silica. A stable pulse, with a near transform limited pulse duration of 6.8 fs at 800 nm was measured with a Second Harmonic Generation Frequency Resolved Optical Gating (SHG-FROG) employing a 10- μm BBO crystal.

Alternatively, we also generated the WLC from the idler of the OPA, tuned to 1.6 μm ; in this case, we used a 2-mm YAG plate instead of the sapphire plate (blue line in Fig. 2 (b)). Owing to the small pump-seed angle and the narrow amplification bandwidth in the near-IR OPA, the angular dispersion of the idler beam is smaller than 1 mrad and is negligible in comparison to its divergence. Thus, the WLC had minimal spatial chirp. The idler of our near-IR OPA is CEP stable since it arises from a difference-frequency generation process between a pump and WLC seed

which are derived from the same 800-nm Ti:sapphire source, thus with the same CEP fluctuations. This CEP stability is expected to be transferred to the WLC and to the amplified pulses [4]. The idler-driven WLC is amplified by the same broadband SH-pumped OPA as the signal-driven one, and gives very similar performance both in terms of output energy and spectrum. Compression was achieved with just 2 bounces off of double chirped mirrors. A near transform limited pulse duration of 6.8 fs at 800 nm was measured with the SHG-FROG and is shown in Fig. 2 (c).

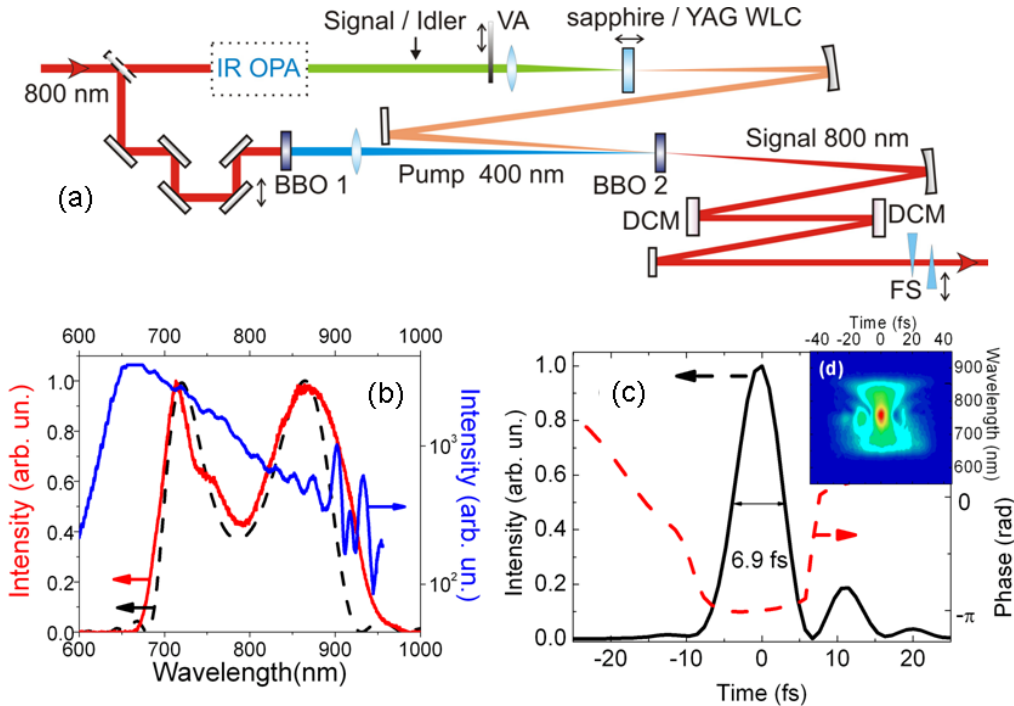


Figure 1: (a) Experimental setup for the generation of few-cycle pulses at 800 nm: BS, beam splitters; VA, variable attenuator; WLC, white light continuum generation with either signal or idler from IR OPA; DCM, double chirped mirror; FS, fused silica glass prisms; BBO 1: second harmonic stage; BBO 2: OPA at 800 nm. (b) Blue line, logarithmic scale: WLC generated by the idler of the near-IR OPA single and seeding the 800 nm OPA. Black dashed line: calculated gain bandwidth curve. Red solid line: amplified spectrum. (c) SHG-FROG trace of the amplified pulses.

References

- [1] A. Baltuška, T. Fuji, and T. Kobayashi, "Visible pulse compression to 4 fs by optical parametric amplification and programmable dispersion control," *Opt. Lett.* **27**, 306-308 (2002).
- [2] D. Brida, G. Cirimi, C. Manzoni, S. Bonora, P. Villorosi, S. De Silvestri and G. Cerullo, "Sub-two-cycle light pulses at 1.6 μm from an optical parametric amplifier", *Opt. Lett.* **33**, 741-743 (2008).
- [3] J. Limpert, C. Agueraray, S. Montant, I. Manek-Höninger, S. Petit, D. Descamps, E. Cormier, F. Salin "Ultra-broad bandwidth parametric amplification at degeneracy," *Opt. Express* **13**, 7386-7392 (2005).
- [4] G. Cirimi, C. Manzoni, D. Brida, S. De Silvestri, and G. Cerullo, "Carrier-envelope phase stable, few-optical-cycle pulses tunable from visible to near IR," *J. Opt. Soc. Am. B* **25**, B62-B69 (2008).

High Repetition Rate Fundamentally Mode-locked Erbium Fiber Ring Laser

Sponsors:

DARPA Contract HR0011-05-C-0155
 DARPA Contract W911NF-04-1-0431
 AFOSR Contract FA9550-07-1-0014

Project Staff:

Jonathan L. Morse, Jeff Chen, Professor Franz X. Kaertner, Professor Erich P. Ippen

Optical arbitrary waveform generation (OAWG) seeks to completely control the time-domain electric field. In the frequency domain, this means complete control of the amplitude and phase of the spectrum. One approach to achieving complete control of the spectrum is to begin with a periodic signal, such as that generated by a mode-locked laser. A periodic signal's modes can be spatially separated by an arrayed waveguide-grating (AWG) and independently modulated in amplitude and phase to produce the arbitrary (and periodic) time-domain waveform.

The need to spatially separate the frequency components places restrictions on the source. As the laser repetition rate (i.e. the mode spacing) decreases, the spectral resolution of the AWG must increase. This leads to a larger AWG, more strict tolerances on waveguide path lengths, and the need for more waveguides for a given spectral bandwidth. Thus the mode-locked laser needs to have the highest possible repetition rate.

One approach to achieving a high repetition rate is to reduce the physical size of the cavity. The intracavity pulse then traverses the cavity more quickly and the temporal spacing between pulses in the output pulse train is reduced. If the average power is kept constant, however, this means that the energy per pulse in the output beam (and in the cavity) decreases inversely proportional to the repetition rate. At some point, the per pulse energy in the cavity will not be enough to maintain the saturable absorber mechanism, and the laser will no longer mode-lock.

To enable ultrashort pulses, both polarization additive-pulse mode-locking (P-APM) and/or saturable Bragg reflector (SBR) mode-locking can be used. These schemes have been applied successfully to soliton [1-3,5] and stretched-pulse [4] fiber lasers. A ring laser taking advantage of both mode-locking mechanisms was previously reported [5]; these results report a system that scales the repetition rate beyond 300 MHz using a novel design.

The laser, illustrated in Figure 1 a), is pumped by two, 750 mW, 980 nm diodes that are polarization multiplexed to output up to 1.2 W. The pump light is coupled into the cavity via free space optics to avoid the need of fiber couplers that would extend the overall cavity length. The gain fiber is pumped through a short-wave-pass 980 nm/1550 nm dichroic mirror. The second short-wave-pass dichroic allows unabsorbed pump to exit the cavity, and the anti-reflection coated silicon flats ensure that no pump light will interfere with SBR operation. The half-wave plate (HWP) controls the output coupling at the polarization beam splitter (PBS). The PBS acts both as the output coupler and the polarization-dependent loss mechanism. The vertically polarized (relative to the optical table) portion of the beam enters the linear arm of the cavity, and is focused on the SBR by an aspheric lens. The linear path includes a quarter-wave plate (QWP) oriented so that the vertically polarized beam returns to the PBS horizontally polarized. After the PBS, a polarizing isolator ensures unidirectional operation. Finally, a HWP and QWP allow control of the polarization state that is launched into the gain fiber.

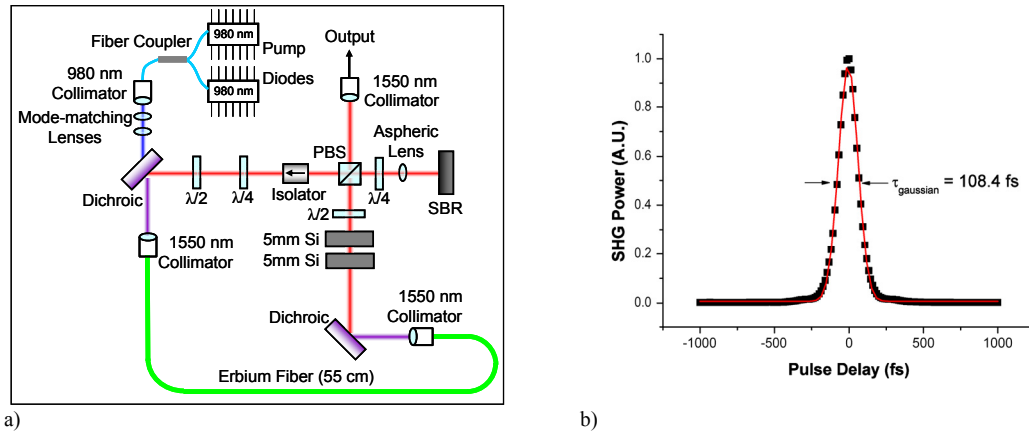


Figure 1. a) Compact cavity mode-locked fiber laser design, b) autocorrelation data with Gaussian fit

The laser was designed to reduce the free space cavity length down to 16 cm, including the double pass in the linear section. This allowed for longer lengths of gain fiber, which enables higher powers and repetition rates.

In typical stretched-pulse erbium fiber ring lasers [4] the normal group-velocity dispersion (GVD) gain fiber is balanced by anomalous GVD single-mode fiber. The net cavity GVD is small, but the alternating sign of the GVD causes the pulse width to stretch and compress dramatically as it traverses the cavity. Alternatively, this design balances the gain fiber's anomalous GVD with the large normal GVD of silicon flats. This enables stretched-pulse operation at a higher repetition rate and accommodates a longer gain fiber length to maintain higher output power.

Mode-locking is achieved through a hybrid scheme that employs a SBR to initiate and P-APM to sustain. The laser is self-starting and stably mode-locks with a SBR mirror in the linear arm. Because the laser does not mode-lock when the SBR is replaced by a silver mirror, the SBR must enable the self-starting. When the polarization launched into the gain fiber is approximately in a linear state, thereby minimizing the nonlinear polarization rotation, mode-locking could not be achieved, which indicates that P-APM is occurring and necessary.

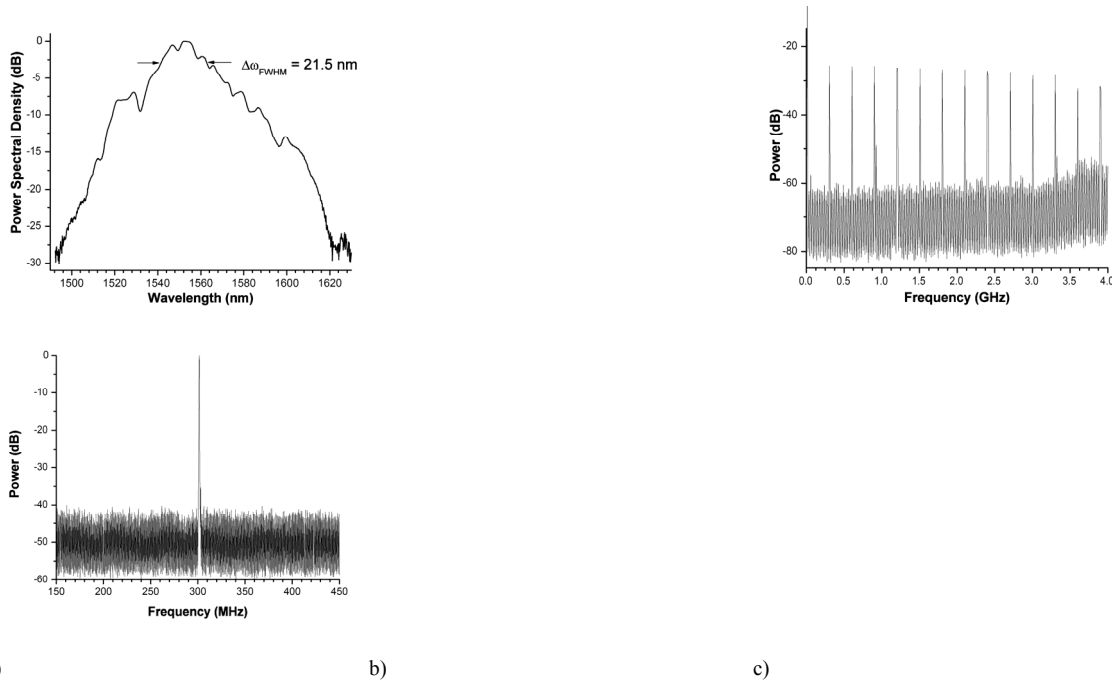


Figure 2. a) optical power spectrum, b) detected RF mode beats, c) detected fundamental RF mode

Figure 1 b) provides an autocorrelation and Gaussian fit of the shortest observed pulse, which corresponds to a 108 fs pulse. This was obtained using $-11,236 \text{ fs}^2$ of GVD to compensate the output pulse chirp. Measurements of pulse duration versus compensating GVD indicate that further optimization should yield pulses as short as 86 fs. Figure 2 a) shows the measured optical power spectrum, which is consistent with a pulse as short as 84 fs. The absence of resonant sidebands and the significant normal chirp of the output pulses indicate that the laser is operating in the stretched-pulse regime.

Figure 2 b) shows the RF spectrum of the laser output. The flat spectral envelope, combined with the smooth optical spectrum verifies single-pulse operation. Figure 2 c) shows the 301 MHz fundamental mode beat, which displays greater than 40 dB of noise suppression and provides further evidence of a clean, single-pulsing mode-locked state. Combined with the 61.1 mW of measured output power, a pulse energy of 203 pJ is demonstrated.

In conclusion, we have demonstrated a fundamentally mode-locked erbium fiber ring laser operating at a repetition rate of 301 MHz, with a pulse energy of 203 pJ, a pulse duration full-width half-maximum of 108 fs and an average output power of 61.1 mW.

References:

1. J Chen, J.W. Sickler, E.P. Ippen, and F.X. Kartner, *High repetition rate, low jitter, low intensity noise, fundamentally mode-locked 167 fs soliton Er-fiber laser*, Optics Letters **32**(11), 1566-1568, (2007).
2. J. Chen, J. W. Sickler, E. P. Ippen, and F. X. Kärtner, *High Repetition Rate, Low Jitter, Fundamentally Mode-locked Soliton Er-fiber Laser*, in Conference on Lasers and Electro-Optics/Quantum Electronics 2007 Technical Digest (Optical Society of America, Washington, D.C., 2007), CThHH3

Chapter 31. Optics and Quantum Electronics

3. T. Wilken, T.W. Hansch, R. Holzwarth, P. Adel, and M. Mei. *Low phase noise 250 MHz repetition rate fiber fs laser for frequency comb applications*, in Conference on Lasers and Electro-Optics/Quantum Electronics 2007 Technical Digest (Optical Society of America, Washington, D.C., 2007), CMR3
4. K Tamura, E. P. Ippen, H. A. Haus, et al. *Opt. Lett.* **18** (13), 1080-1082, 1993
5. H. Byun, J. Sickler, J. Morse, J. Chen, D. Pudo, E. P. Ippen, and F. X. Kärtner, *Femtosecond passively mode-locked fiber lasers using saturable Bragg reflectors*, in Conference on Ultrafast Phenomenon 2008 (2007 European Physical Society) awaiting publication.

Single-Mode Diode Pumped Cr:Colquiriite Lasers

Sponsors

National Science Foundation – BES-0522845 and ECS-0900901

Air Force Office of Scientific Research – FA9550-07-1-0014 and FA9550-07-1-0101

National Institutes of Health – 2R01-CA075289-12 and 5R01-NS057476-02

Project Staff

Umit Demirbas, Duo Li, Jing Wang, Dr. Jonathan R. Birge, Dr. Gale S. Petrich, Dr. Peter Fendel, Prof. Leslie A. Kolodziejski, Prof. Alphan Sennaroglu, Prof. Franz X. Kärtner, Prof. James G. Fujimoto

Among solid-state vibronic lasers, Ti:Sapphire has the broadest tuning range (660-1180 nm), and can directly generate sub-5-fs pulses [1]. However, because direct diode pumping is not currently possible, Ti:Sapphire lasers are typically pumped by frequency-doubled diode-pumped neodymium lasers, which are bulky and cost \$50-100k, making the overall system cost high and limiting wide-spread use.

Cr³⁺-doped colquiriite crystals such as Cr³⁺:LiSAF [2], Cr³⁺:LiSGaF [3], and Cr³⁺:LiCAF [4] are an attractive alternative to Ti:Sapphire. They provide broadly tunable operation around 800 nm, enabling the generation of pulses as short as ~10-fs. Their absorption bands are red shifted to ~650 nm, enabling direct diode pumping with low-cost diode lasers, significantly reducing the total cost of the laser system. Other advantages of Cr:Colquiriites are their low lasing threshold (~10 mW) and high intrinsic slope efficiencies (>50%), enabling efficient laser operation with electrical-to-optical conversion efficiencies exceeding 10%.

In recent years, our group has been working with Cr:Colquiriite gain media, with the aim of developing a low-cost and efficient femtosecond laser technology, which can replace the expensive Ti:Sapphire lasers in selected areas of applications. Here we will summarize our recent experimental results with Cr:Colquiriite gain media both in continuous-wave (cw) and cw mode-locked operation [5-7].

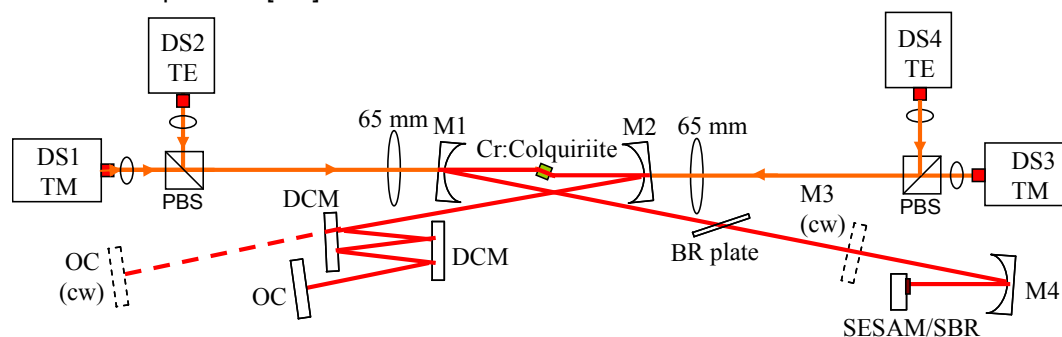


Figure 1. Schematic of the single-mode diode pumped Cr³⁺:Colquiriite laser system. DS1-DS4: Single-mode pump diodes at 660 nm, PBS: polarizing beam splitting cube, M1-M2: pump mirrors with R= 75 mm, M3: flat high reflector, DCM: flat double-chirped mirrors with ~ -50 to -80 fs² dispersion per bounce, SESAM/SBR: semiconductor saturable absorber mirror / saturable Bragg reflector, BR plate: birefringent plate for tuning. Dashed lines indicate the cw laser cavity.

Figure 1 shows an example schematic for a single-mode diode pumped Cr:Colquiriite laser developed in this program. The gain medium was pumped by four linearly-polarized, ~150 mW, AlGaInP single-mode diodes (DS1-DS4), with microlensed output, each costing only \$150. This cheap pump source enables the reduction of the cost of the laser significantly. An astigmatically compensated, x-folded laser cavity consisting of two curved pump mirrors (M1 and M2), a flat end mirror (M3), and a flat output coupler (OC) was used in cw laser experiments.

Figure 2 shows an example of cw laser efficiency curves taken with the Cr:LiSAF and Cr:LiCAF gain medium, using output couplers ranging from 0.5 to 6% transmission. Using the 1.95% output coupler, the Cr:LiCAF laser produced up to 266 mW of output power with ~550 mW of absorbed pump power. The corresponding threshold pump power and the slope efficiency with respect to absorbed pump power were 45 mW and ~54%, respectively. A lasing threshold as low as 5 mW was measured using a 0.05% output coupler. Figure 2 (right) shows representative efficiency curves for the Cr:LiSAF gain medium with the 0.5% and 3.1% output couplers. Thresholds as low as 5 mW were measured with the 0.05% output coupler. The highest cw output power (257 mW) was obtained using a 1.6% output coupler which had a 21 mW lasing threshold and 50% slope efficiency. Slope efficiencies up to 53% were obtained with a 3.1% output coupler. Similar cw performance was also obtained with Cr:LiSGaF gain medium.

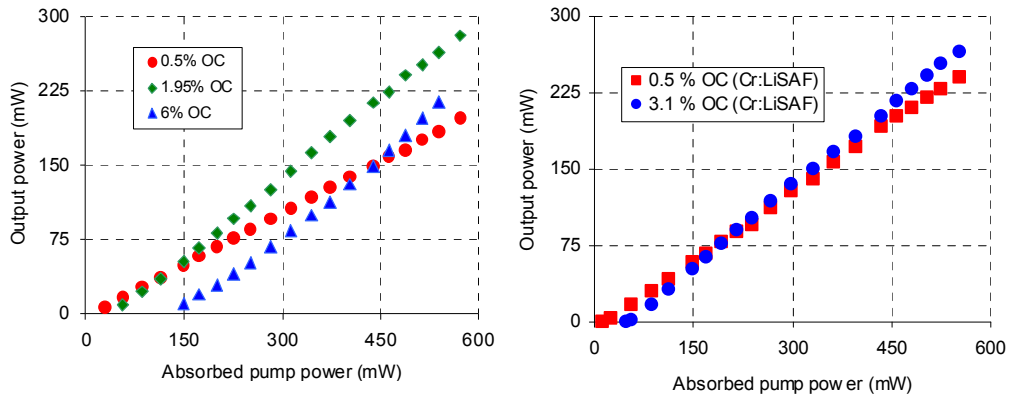


Figure 2: Continuous-wave efficiency curves for the single-mode diode-pumped Cr:LiCAF (left) and Cr:LiSAF (right) lasers.

Figure 3 summarizes the cw experimental results, by showing the measured variation of the cw laser output power with output coupler transmission for all the three gain media. All the results were obtained at an absorbed pump power level of ~550 mW, at room temperature, without applying water cooling to the crystals and diodes. In cw operation, up to 257, 269 and 266 mW of output power was obtained and slope efficiencies of 53%, 62% and 54% were demonstrated, for Cr:LiSAF, Cr:LiSGaF and Cr:LiCAF, respectively. To our knowledge, this the highest output power and slope efficiency obtained from single-mode diode pumped Cr:Colquirite lasers. In addition, the lasers also work with very high efficiency (electrical to optical conversion efficiencies >10%).

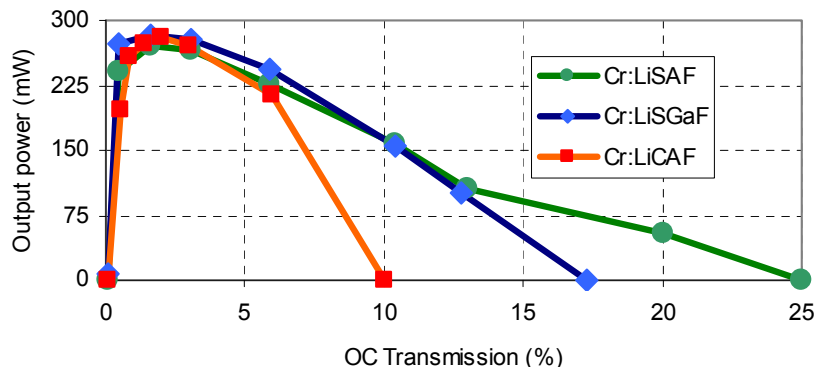


Figure 3: Measured variation of cw laser output power with output coupling (OC) for Cr:LiSAF, Cr:LiSGaF and Cr:LiCAF gain media, at ~550 mW absorbed pump power.

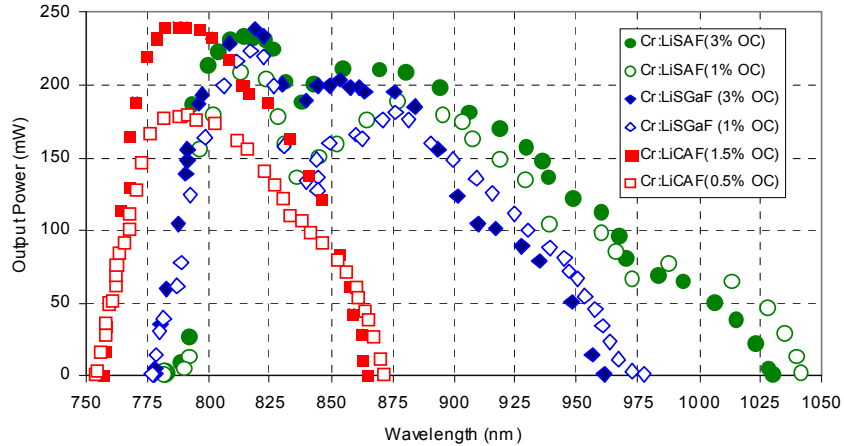


Figure 4. Continuous-wave tuning data obtained with Cr:LiCAF, Cr:LiSAF, and Cr:LiSGaF lasers.

Figure 4 shows the cw tuning ranges obtained for Cr:Colquiriites at an absorbed pump power of ~500 mW. A birefringent filter or a fused silica prism could be used for tuning and the tuning range extended from 775 nm to 1042 nm for Cr:LiSAF, from 777 nm to 977 nm for Cr:LiSGaF, and from 756 nm to 865 nm for Cr:LiCAF. To the best of our knowledge, these are the broadest tuning ranges reported for Cr:Colquiriite gain media to date. Note that with these gain media, the wavelength range from 756 nm to 1041 nm can be continuously covered.

Gain Media	Pulse energy (nJ)	Average output power (mW)	Pulse width (fs)	Repetition rate (MHz)	Central Wavelength (nm)	Dispersion compensation method
Cr:LiCAF	1.4	180	240	130	794	GTI
	0.9	120	45	130	803	DCMs
	1.8	180	70	100	800	DCMs
Cr:LiSAF	1.23	152	85	123	812	GTI
	1.43	164	75	114	850	DCM
	1.7	137	70	80	900	DCM
	1	85	26	85	850	FS Prism pair
	1.85	157	46	85	870	FS Prism pair
	2.31	197	74	85	859	FS Prism pair
Cr:LiSGaF	1.51	127	42	84	816	FS Prism pair
	2.1	181	53	86	867	FS Prism pair
	1.8	155	54	86	820	FS Prism pair
	2.43	196	82	81	815	GTI
Cr:LiSGaF	1.93	146	55	75	860	DCMs

Table 1. List of average output powers, pulse energies and pulse widths obtained with Cr:Colquiriite gain media in cw modelocked operation during this program.

In mode locking experiments, double-chirped mirrors (DCMs), Gires–Tourniois interferometer mirrors (GTIs), or fused silica prism pairs were used for dispersion compensation (Fig. 1 and Table 1). SESAMs/SBRs with low level of nonsaturable loss (~0.5 %) were used to initiate and sustain mode locking. The SESAM mode-locked laser was self-starting, immune to environmental fluctuations and did not require careful cavity alignment, enabling turn-key operation. When modelocked Cr:Colquiriite lasers easily produced sub-100-fs pulses with ~1-2.5 nJ of pulse energy, from standard ~100 MHz repetition rate cavities. With careful dispersion compensation, pulses as short as ~25 fs could be obtained with Cr:LiSAF gain media, and the pulsewidth was limited with the SESAM/SBR bandwidth (Figure 5). Using different SESAM/SBRs, central wavelengths of the spectra can be tuned from ~790 to ~930 nm. Also, each SESAM/SBR enabled 20-30 nm tuning around their central reflectivity bandwidth (Figure 6). The

tuning range was again limited by the SESAM/SBR reflectivity bandwidth. Slightly lower output power levels were obtained with Cr:LiCAF due to the low gain nature of this gain medium. To the best of our knowledge, these are the highest average powers and pulse energies obtained using single-mode diode pumping of Cr:Colquiriites. In addition, electrical to optical conversion efficiency of $\sim 8\%$ was demonstrated in mode-locked operation, which we believe, is one of the highest conversion efficiency ever obtained from femtosecond solid state lasers.

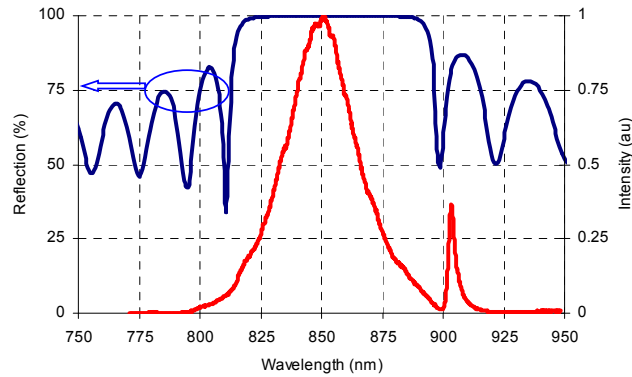


Figure 5. Spectrum for the ~ 26 fs ~ 1 -nJ pulses generated by the single-mode diode pumped Cr:LiSAF laser operating at 85 MHz repetition rate. Calculated reflectivity curve for the SESAM/SBR is also shown. The SESAM/SBR had a central reflectivity around 850 nm. This was the shortest pulses we could get from the laser, and it is clear that pulsewidth is limited by the SESAM/SBR reflectivity bandwidth.

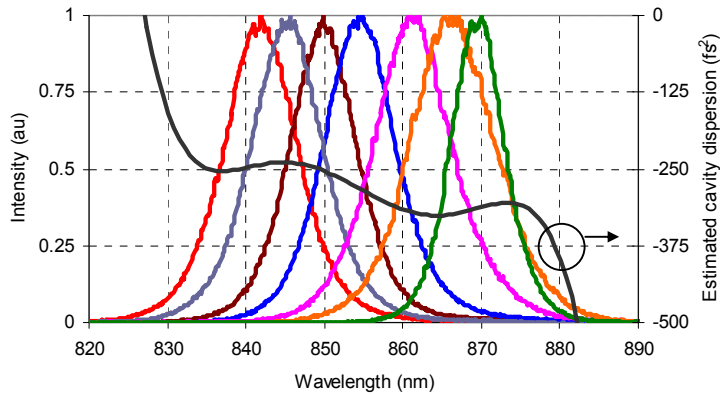


Figure 6. Spectra from the Cr³⁺:LiSAF laser, showing the tunability of the central wavelength from 842 nm to 870 nm, for sub-80-fs pulses. Estimated total cavity dispersion is also shown. The relatively large fluctuation in the GVD curve is mostly due to the SESAM/SBR, which had large GVD deviations from ~ 0 fs² away from the central wavelength (850 nm). We believe the limited GVD and reflectivity bandwidth of the SESAM/SBR restricted the tuning range to ~ 28 nm.

The results obtained so far demonstrate that single-mode diode Cr³⁺:Colquiriite lasers can provide laser performance approaching Ti:Sapphire lasers in both cw and cw modelocked regime. We believe the single mode diode-pumped Cr³⁺:Colquiriite laser system is quite promising because (i) it would significantly reduce the laser cost (the total cost of materials could be below $\sim \$10$ k), (ii) it would also be inexpensive to maintain, (iii) the system has high electrical-to-optical conversion efficiency and could be used in applications where minimal power consumption is critical, (iv) the laser could be made compact and portable (since the diodes and the laser crystal did not require water cooling and the diodes could be run by batteries), and (v) it could enable turn-key operation and would be suitable for use outside the research laboratory environment. Therefore, we believe that tunable cw and fs laser sources based on

Cr^{3+} :Colquiriite gain media have the potential to replace the current expensive Ti:Sapphire technology in several areas of research and application. Future research will focus on obtaining broadband fs tunability and shortening the pulsewidths to ~ 10 fs level, by using broadband SESAM/SBRs[8].

References

- [1] R. Ell, U. Morgner, F. X. Kärtner, J. G. Fujimoto, E. P. Ippen, V. Scheuer, G. Angelow, and T. Tschudi, "Generation of 5 fs pulses and octave-spanning spectra directly from a Ti:sapphire laser," *Optics Letters*, vol. 26, pp. 373-375, 2001.
- [2] S. A. Payne, L. L. Chase, L. K. Smith, W. L. Kway, and H. W. Newkirk, "Laser performance of $\text{LiSAIF}_6:\text{Cr}^{3+}$," *Journal of Applied Physics*, vol. 66, pp. 1051-1056, 1989.
- [3] L. K. Smith, S. A. Payne, W. L. Kway, L. L. Chase, and B. H. T. Chai, "Investigation of the laser properties of $\text{Cr}^{3+}:\text{LiSrGaF}_6$," *IEEE Journal of Quantum Electronics*, vol. 28, pp. 2612-2618, 1992.
- [4] S. A. Payne, L. L. Chase, H. W. Newkirk, L. K. Smith, and W. F. Krupke, " $\text{LiCaAlF}_6:\text{Cr}^{3+}$ a promising new solid-state laser material," *IEEE Journal of Quantum Electronics*, vol. 24, pp. 2243-2252, Nov 1988.
- [5] U. Demirbas, D. Li, J. R. Birge, A. Sennaroglu, G. S. Petrich, L. A. Kolodziejski, F. X. Kaertner, and J. G. Fujimoto, "Low-cost, single-mode diode-pumped Cr:Colquiriite lasers " *Optics Express*, vol. 17, pp. 14374-14388, 2009.
- [6] U. Demirbas, A. Sennaroglu, F. X. Kärtner, and J. G. Fujimoto, "Highly efficient, low-cost femtosecond $\text{Cr}^{3+}:\text{LiCAF}$ laser pumped by single-mode diodes," *Optics Letters*, vol. 33, pp. 590-592, 2008.
- [7] U. Demirbas, A. Sennaroglu, F. X. Kärtner, and J. G. Fujimoto, "Comparative investigation of diode pumping for continuous-wave and mode-locked $\text{Cr}^{3+}:\text{LiCAF}$ lasers " *Journal of Optical Society of America B*, vol. 26, pp. 64-79, 2009.
- [8] S. N. Tandon, J. T. Gopinath, H. M. Shen, G. S. Petrich, L. A. Kolodziejski, F. X. Kärtner, and E. P. Ippen, "Large-area broadband saturable Bragg reflectors by use of oxidized AIAs," *Optics Letters*, vol. 29, pp. 2551-2553, Nov 1 2004.

MW Peak Powers from Femtosecond Cr:Colquiriite Lasers

Sponsors

National Science Foundation – BES-0522845 and ECS-0900901

Air Force Office of Scientific Research – FA9550-07-1-0014 and FA9550-07-1-0101

National Institutes of Health – 2R01-CA075289-12 and 5R01-NS057476-02

Project Staff

Umit Demirbas, Prof. Alphan Sennaroglu, Dr. Kyung-Han Hong, Prof. Franz X. Kärtner, Prof. James G. Fujimoto

The advantages of single-mode diode pumped Cr³⁺-doped Colquiriite laser technology has been described in detail in the previous section. In mode-locking experiments, pumping with four single-mode diodes, Cr³⁺: Colquiriite lasers produce ~50-100 fs pulses with ~1-2.5 nJ of pulse energies and ~20 kW of peak powers from standard ~100 MHz level cavities[1]. The pulse energies and peak powers are limited by the available pump power (a total pump power of ~600 mW available from four single mode diodes).

However, studies in nonlinear optics, pump-probe measurement, micromachining, etc., often require high pulse energy femtosecond sources. To address this need, we have been exploring several different approaches to scale the output energies and peak powers of low-cost Cr³⁺:Colquiriite laser technology. In this section, we will review our recent results, where we have demonstrated ~100nJ level pulse energies and ~MW level peak powers [2, 3] from low-cost Cr:Colquiriite laser systems.

One approach to scale the pulse energies from laser oscillators is to reduce the repetition rate of the cavity. If the average output power is nearly constant, lowering the repetition rate leads to higher output energies, provided that additional nonlinearities in the cavity can be controlled or compensated. Multipass cavities (MPC) can be used to extend the cavity lengths with a relatively compact mirror configuration [4, 5]. Below, we will first review our recent results with an extended cavity Cr:LiCAF laser, where we achieved pulse energies of 10 to 15 nJ and peak powers of 50 to 100 kW [2].

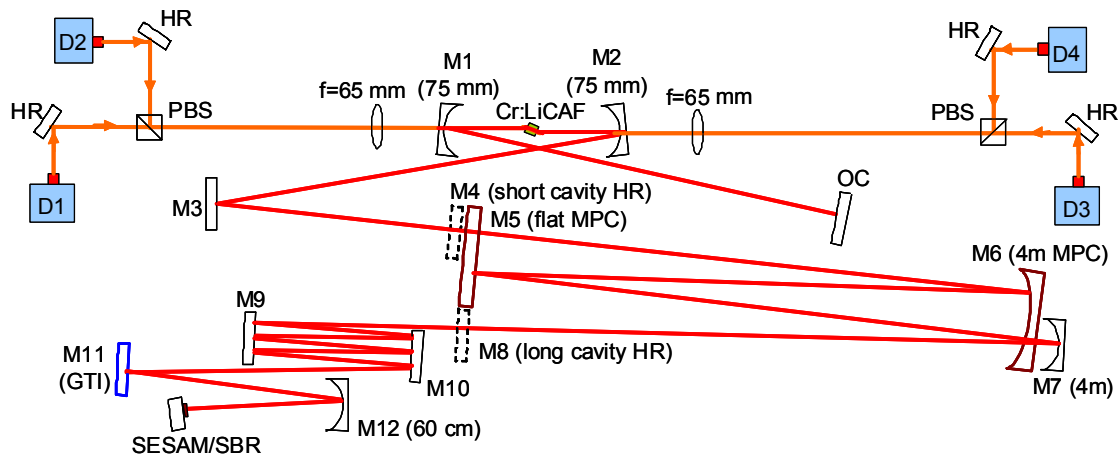


Figure 1. Schematic for the extended-cavity (MPC) single mode diode pumped Cr³⁺:LiCAF laser.

Figure 1 shows the experimental schematic for a short and an extended-cavity (MPC) Cr³⁺:LiCAF laser. The cavity length was extended by removing the high reflecting end mirror M4 and adding a q-preserving MPC consisting of a flat (M5) and curved (M6, R=4 m) high reflector. This reduced the repetition rates to ~10-11 MHz range. GTI and DCM mirrors were used for dispersion compensation. The total round trip dispersion was ~2000 fs². When mode-locked at

the full pump power (~540 mW), the laser produced 9.92 nJ pulses with 95 mW average power at a 9.58 MHz repetition rate (using a 2.4% output coupler). Figure 2 shows the measured optical spectra and autocorrelation. The spectra was centered around 782.7 nm and has a FWHM of ~6.75 nm, which supports ~95.5 fs transform limited pulses, assuming a sech² pulse shape. The autocorrelation was ~151.3 fs FWHM, corresponding to a ~98 fs pulse for sech² pulse shape. The time bandwidth product was ~0.323, close to the transform limit of 0.315. The corresponding peak power was ~101 kW. The spectral side lobe around 809 nm was due to GVD oscillations from the GTI mirror.

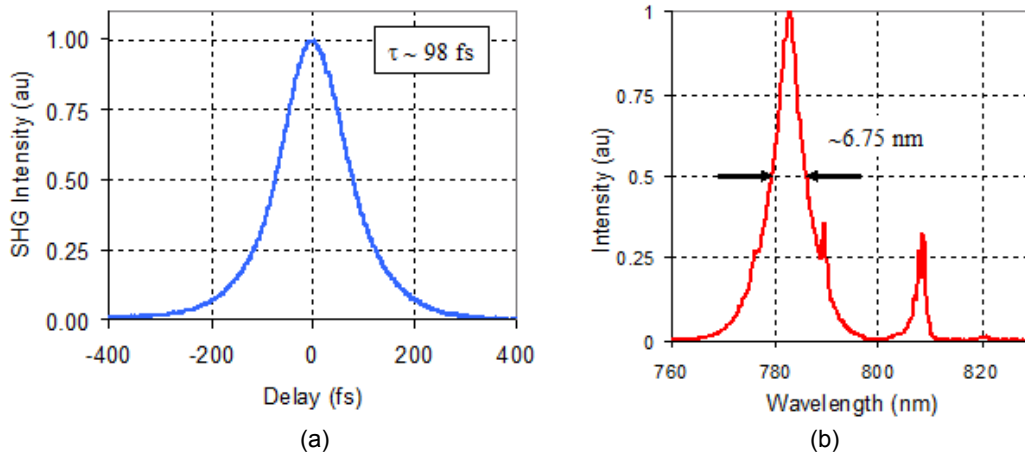


Figure 2. Intensity autocorrelation and optical spectra for the 98-fs, 9.92 nJ pulses (~101kW peak power), corresponding to 95 mW average output power at 9.58 MHz repetition rate.

Another approach to scale the pulse energies is to use cavity dumping [6, 7]. Our group recently demonstrated the first cavity-dumping experiments with a low-cost Cr³⁺:Colquirrite laser [8]. Figure 3 shows the schematic of the cavity-dumped, single-mode diode pumped Cr³⁺:LiSAF laser. A ~3-mm thick, fused silica acousto-optic cavity dumper was placed at Brewster’s angle into a second Z-fold focus, generated by 100 mm radius mirrors. The cavity dumper had a single pass diffraction efficiency of about 30%, and was used in double-pass configuration, where it produced 50-60% dumping efficiencies. A small metallic high reflector was used to pick off the dumped beam after its second pass through the dumper.

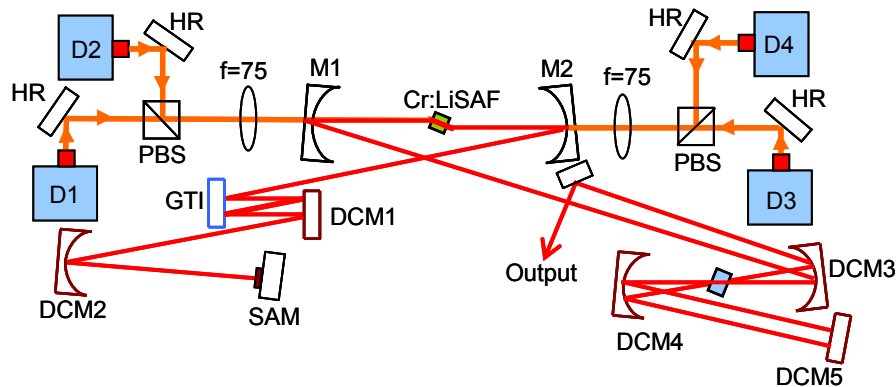


Figure 3. Schematic of the cavity dumped, single-mode diode-pumped Cr³⁺:LiSAF laser system.

Table 1 summarizes the cavity dumping results obtained with the Cr:LiSAF laser. For repetition rates up to 50 kHz, dumping efficiencies of ~50%, and pulse energies of about ~100 nJ could be obtained repeatedly and the dumping process had very little effect on the laser dynamics. The contrast ratio between the dumped output pulses and the neighboring pulses was better than

20:1. The highest pulse energy obtained was 112 nJ, which was obtained at a repetition rate of 10 kHz. For this case, the pulse duration was about ~ 120 fs, corresponding to a peak power of 930 kW. As an example Fig. 4, shows the measured dynamics of intracavity pulse train for dumping rates of 10 and 50 kHz. In both cases, the dumping event generates fluctuations in intracavity pulse energy; however, the laser continues to stably operate in the cw mode-locked regime throughout the process. Dumping at 10 kHz clearly shows the interplay between the population inversion and the intracavity pulse energy first results in an overshoot of intracavity pulse energy, then the pulse energy relaxes back to its steady state value. Note that at 50 kHz dumping rate (and above), the dumping event occurs before the transient decays back.

Dumping frequency (kHz)	Pulse energy (nJ)	Pulse width (fs)	Average power (mW)	Peak power (kW)	Dumping efficiency (%)
10	112	120	1.12	930	56
20	105	120	2.09	870	52
50	98	121	4.9	810	49
100	87	122	8.73	720	44
200	77	124	15.3	620	38
500	68	130	34	520	34
1000	62	143	62	430	31

Table 1: Summary of the cavity dumping results with the single-mode diode pumped Cr:LiSAF laser.

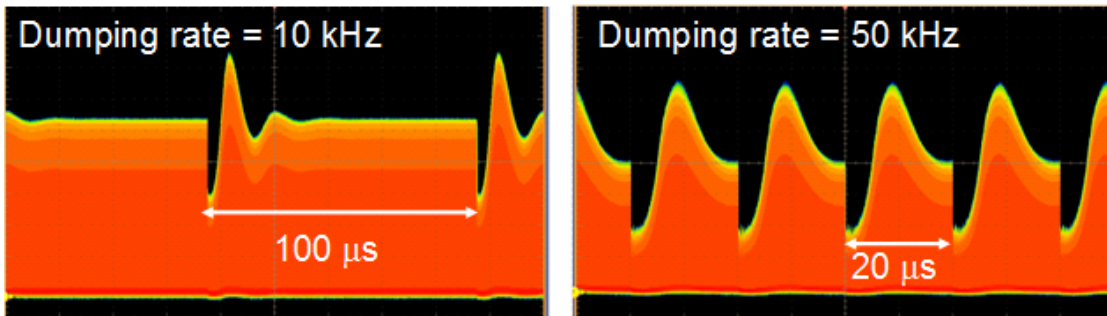


Figure 4: Measured dynamics of intracavity pulse train at dumping rates of 10 kHz and 50 kHz.

The pulsewidths (~ 100 fs) obtained in the MPC and cavity dumped studies were limited by the working range of the saturable absorber mirror, where the intensity is sufficient to produce absorption saturation, but not high enough to produce parasitic two photon absorption. When we tried to reduce the pulse durations below ~ 100 fs, we observed pulse breakup and multiple pulsing type instabilities due to the high incident instantaneous intensity levels on the saturable absorber. In principle it is possible to reduce the pulse break up instabilities of the saturable absorber mirror by increasing the beam spot size on the mirror. However, this has the drawback of (i) increasing the Q-switching tendency, and (ii) makes initiating of mode-locking difficult, which limits the dumping efficiencies (pulse energies) one can get at high repetition rates for the cavity dumped laser.

To our knowledge, this is the first demonstration of cavity dumping of a Cr:Colquiriite laser. Cavity dumping at 10 kHz repetition rates, the laser generated ~ 120 fs long pulses centered around ~ 825 nm, with 112 nJ of pulse energy and ~ 0.93 MW of peak power. At higher dumping rates of up to 1 MHz, reduced pulse energies of 62 nJ could be generated. Pulse durations and energies appear to be limited by q-switching, two photon absorption and other instabilities. Low-cost, compact and efficient Cr³⁺:Colquiriite lasers with \sim MW level peak powers are promising tools for several scientific and industrial applications.

References

- [1] U. Demirbas, D. Li, J. R. Birge, A. Sennaroglu, G. S. Petrich, L. A. Kolodziejski, F. X. Kaertner, and J. G. Fujimoto, "Low-cost, single-mode diode-pumped Cr:Colquiriite lasers " *Optics Express*, vol. 17, pp. 14374-14388, 2009.
- [2] U. Demirbas, A. Sennaroglu, F. X. Kärtner, and J. G. Fujimoto, "Generation of 15 nJ pulses from a highly efficient, low-cost multipass-cavity Cr³⁺:LiCAF laser," *Optics Letters*, vol. 34, pp. 497-499, 2009.
- [3] U. Demirbas, K.-H. Hong, J. G. Fujimoto, A. Sennaroglu, and F. X. Kaertner, "A low-cost cavity-dumped femtosecond Cr³⁺:LiSAF laser producing >100 nJ pulses " *Optics Letters*, 2009, in preparation.
- [4] R. P. Prasankumar, Y. Hirakawa, A. M. J. Kowalevich, F. X. Kärtner, J. G. Fujitimo, and W. H. Knox, "An extended cavity femtosecond Cr:LiSAF laser pumped by low cost diode lasers," *Optics Express*, vol. 11, pp. 1265-1269, 2003.
- [5] A. Sennaroglu, A. M. Kowalevich, E. P. Ippen, and J. G. Fujimoto, "Compact femtosecond lasers based on novel multipass cavities," *Ieee Journal of Quantum Electronics*, vol. 40, pp. 519-528, May 2004.
- [6] M. Ramaswamy, M. Ulman, J. Paye, and J. G. Fujimoto, "Cavity-dumped femtosecond Kerr-lens mode-locked Ti:Al₂O₃ laser," *Optics Letters*, vol. 18, pp. 1822-4, 1993.
- [7] M. S. Pshenichnikov, W. P. d. Boeij, and D. A. Wiersma, "Generation of 13-fs, 5-MW pulses from a cavity-dumped Ti:sapphire laser," *Optics Letters*, vol. 19, pp. 572-574, 1994.
- [8] U. Demirbas, K.-H. Hong, J. G. Fujimoto, A. Sennaroglu, and F. X. Kaertner, "A low-cost cavity-dumped femtosecond Cr³⁺:LiSAF laser producing >100 nJ pulses " *Optics Letters*, 2009, in preparation.

power (Fig. 2). Mode-locking was self-starting and robust to environmental fluctuations. The corresponding peak power was ~ 2.4 kW, which is three orders of magnitude improvement compared to the previous results in the literature. Future research will be aimed at increasing the repetition rate of the laser to multi-GHz level.

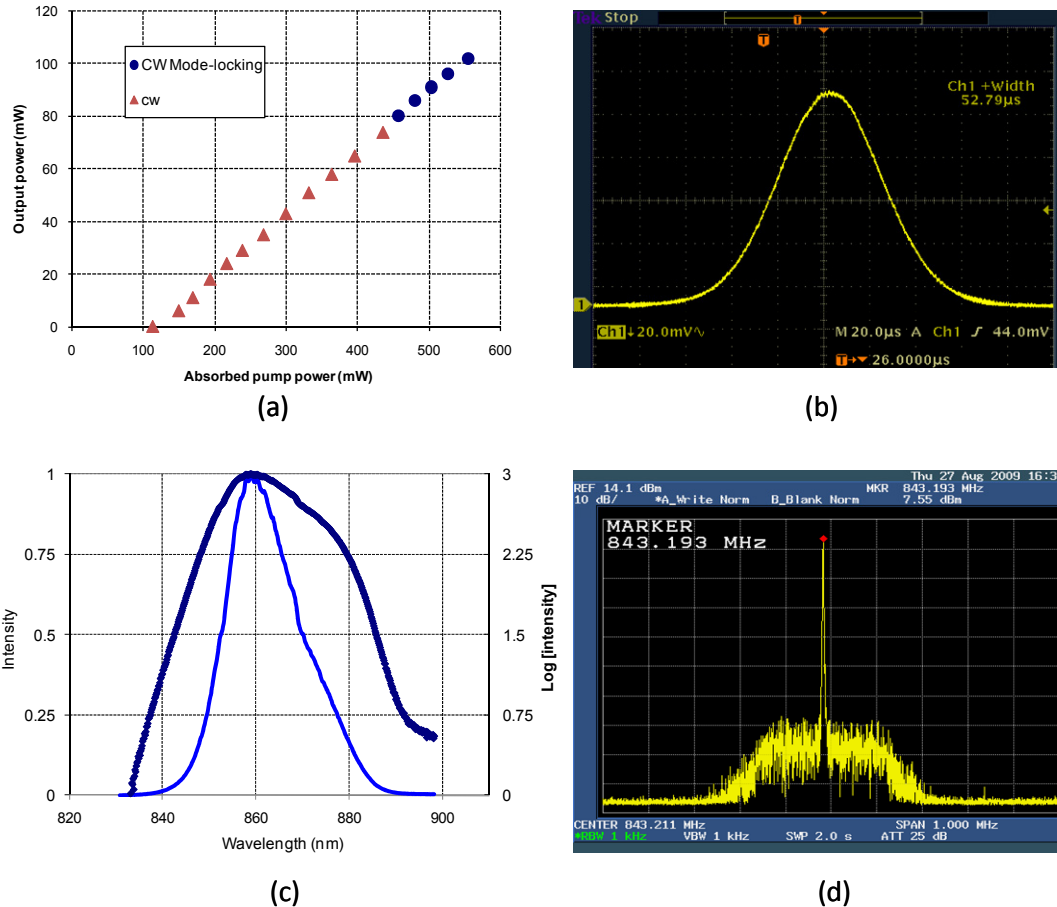


Figure 2. (a) Mode-locking efficiency, (b) autocorrelation trace, (c) optical spectra, (d) RF spectrum for the ~ 50 fs, 0.12 nJ pulses at ~ 843 MHz repetition rate from the single-mode diode pumped Cr:LiSAF laser.

References

- [1] A. Bartels, D. Heinecke, and S. A. Diddams, "Passively mode-locked 10 GHz femtosecond Ti:sapphire laser," *Optics Letters*, vol. 33, pp. 1905-1907, 2008.
- [2] C. G. Leburn, A. A. Lagatsky, C. T. A. Brown, and W. Sibbett, "Femtosecond Cr⁴⁺: YAG laser with 4GHz pulse repetition rate," *Electronics Letters*, vol. 40, pp. 805-807, Jun 24 2004.
- [3] L. Krainer, R. Paschotta, S. Lecomte, M. Moser, K. J. Weingarten, and U. Keller, "Compact Nd:YVO₄ lasers with pulse repetition rates up to 160 GHz," *IEEE Journal of Quantum Electronics*, vol. 38, pp. 1331-1337, 10, October 2002 2002.
- [4] S. C. Zeller, T. Sudmeyer, K. J. Weingarten, and U. Keller, "Passively modelocked 77 GHz Er:Yb:glass laser," *Electronics Letters*, vol. 43, pp. 32-33, 2007.
- [5] A. J. Kemp, B. Stormont, B. Agate, C. T. A. Brown, U. Keller, and W. Sibbett, "Gigahertz repetition-rate from directly diode-pumped femtosecond Cr:LiSAF laser," *Electronics Letters*, vol. 37, pp. 1457-1458, 2001.

Femtosecond Laser Frequency Combs, Optical Clocks and Phase Control

Dynamics of Octave-Spanning Titanium:Sapphire Lasers

Sponsors

Defense Advanced Research Projects Agency (DARPA) grant HR0011-05-C-0155

Air Force Office of Scientific Research (AFOSR), FA9550-07-1-0014

Project Staff

Michelle Y. Sander, Professor Erich P. Ippen and Professor Franz X. Kärtner

To generate ultrashort pulses with octave-spanning spectra at high repetition rates from Titanium:sapphire lasers, the various laser components need to be optimized and a good dispersion compensation reached so that a broadband spectrum can be supported in the cavity. We derived a one-dimensional model which follows the pulse formation in femtosecond laser cavities to improve the design and evaluate different cavity component choices.

The temporal pulse evolution in Kerr-lens mode-locked Ti:sapphire lasers is well described by dispersion managed mode-locking (DMM) 1: In systems where the group delay dispersion (GDD) periodically changes its sign, with small total GDD per round-trip when compared to the absolute GDD in each section, dispersion managed solitary pulses are formed. Due to the encountered GDD and nonlinearities, mostly self-phase modulation, the pulses undergo temporal and spectral broadening and recompression during each cavity round-trip.

Based on the DMM and the Nonlinear Schrödinger Equation we extended this model to include higher-order material dispersion as well as the detailed mirror and output coupler characteristics to reflect the temporal laser dynamics. It is shown that this approach can capture the octave-spanning output spectrum and the generated sub-two-cycle pulses very well, thus allowing for a direct and precise comparison with experimental results.

Figure 1 presents the experimental setup for a prismless ring laser cavity. It features custom-designed, double-chirped mirror (DCM) pairs and wedges of BaF₂ and fused silica (FS) for broadband dispersion compensation 2. The laser generates two outputs: the main output, which can be used as a source for additional applications, and the 1f-2f output, coupled out through one of the DCMs, which allows phase stabilization of the laser independent from the main output.

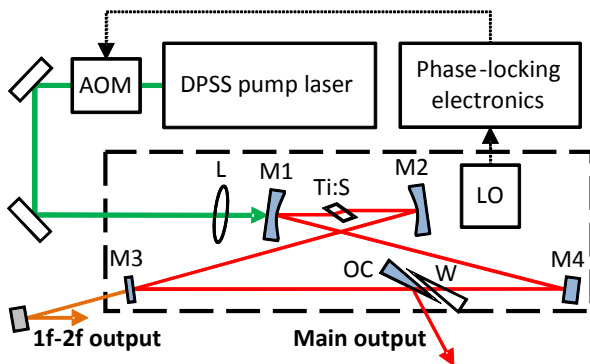


Figure 1: Experimental setup for a 500-MHz Ti:sapphire ring laser 2.

The numerical analysis follows the temporal and spectral breathing through the cavity and takes the localized impact and order of the different components into account. To emphasize the importance of the mirror characteristics, the numerical analysis was conducted for two cases: with

the designed and with the experimentally measured mirror data (these cases have slightly different GD curves, see 3). Fig. 2 shows the output characteristics of the 500-MHz ring laser 2. The main output and the 1f-2f referencing output spectra are illustrated for three different cases: for simulations using the measured or designed mirror characteristics (for the reflectivity and dispersion), and for the experimentally obtained results. The simulated spectra in Figs. 2(a) and 2(b) agree well and, on average, show good agreement with the measured data. The main features in the spectral wings are accurately reproduced and we can predict the optimized power levels achievable for the 1f and 2f output (with 1160 nm and 580 nm 1f and 2f frequencies, respectively) on the chosen normalized scale. When comparing the two numerical results for both the 1f-2f output and the main output, the power spectral density (PSD) with the designed mirrors falls off slightly steeper in the long-wavelength regime (i.e., longer than 1160 nm). As the long wavelengths penetrate deeper into the mirror stacks, they are more prone to fabrication tolerances, which can explain the slight deviations. At the same time, incorporating the measured mirror data enhances the agreement between experiment and simulation even further.

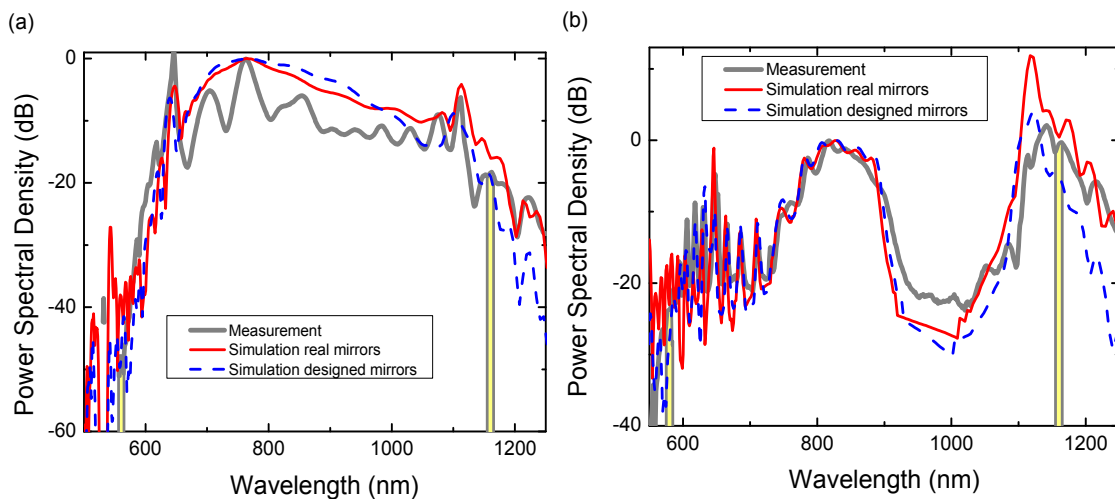


Figure 2: Main output and 1f-2f output spectrum for the 500 MHz ring laser cavity: The measured data is compared with the numerical results, using either the real mirror data or the designed mirror data for the DCMs.

As another important characteristic, the main output pulse was examined after being compressed externally by an additional delay line. Fig. 3 presents the comparison of the numerical result with the retrieved pulse from two-dimensional spectral shearing interferometry (2DSI) measurements 2: the measured pulse shape and pulse duration of 4.9 fs reproduce the obtained simulation results. Thus, we demonstrated that sub-two-cycle pulse generation in Ti:sapphire oscillators can be captured in great detail with the described one-dimensional temporal model.

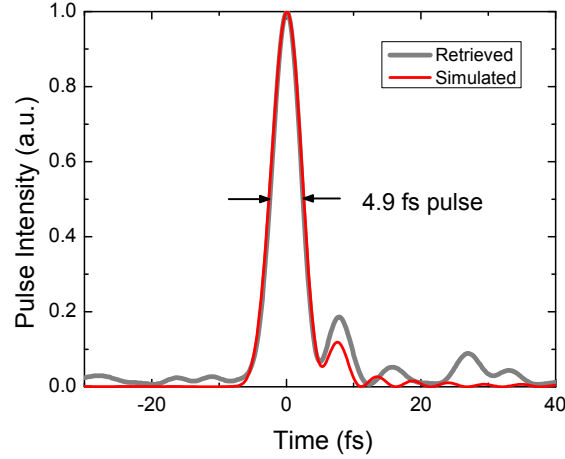


Figure 3: Output pulse of the 500-MHz laser after external compression. The measured pulse is retrieved from 2DSI measurements and shows great agreement with the simulated output pulse.

Having studied the characteristics of the steady state solutions, this model was extended to evaluate the characteristics of the mode-locked laser pulse train, where we focused on the carrier envelope phase dynamics. Due to the difference in phase and group velocity of the pulse a carrier envelope phase shift (CEP) occurs during each cavity round-trip. To build optical clocks this CEP needs to be stabilized and controlled accurately. Most commonly this is achieved via modulation of the pump power, which in turn affects the intracavity power. Thus, the dependency of this phase shift on the intracavity pulse energy was examined in more detail.

A pulse train, $E(t)$, can be expressed as a sum of pulse envelopes multiplied by a carrier wave of radial frequency ω_c , repeating with the round-trip time T_R . In addition, for different energies, the pulse picks up a timing shift τ , which describes the deviations from the round-trip time.

$$E(t) = \sum_n A(t - nT_R - n\tau) e^{j\omega_c(t - nT_R - n\tau)} e^{j\Phi} e^{jn\omega_c\tau} e^{jn\Phi_{CE}}$$

Two different contributions determine the CEP: a linear term, $\Delta\Phi_{CE, Lin}$, arising from the difference in the material phase and group velocity, and a nonlinear term $\Delta\Phi_{CE, NL}$, dominated by nonlinear effects in the crystal. Here, the impact of self-steepening is significant, which introduces an asymmetry into the spectrum and enhances the shorter wavelengths while the longer wavelengths are attenuated.

$$\begin{aligned} \Delta\Phi_{CE} &= \Delta\Phi_{CE, NL} + \Delta\Phi_{CE, Lin} = \Phi + \omega_c\tau + \Phi_{CE} = \Phi + \omega_c\tau + \omega_c L \left(\frac{1}{v_g} - \frac{1}{v_p} \right) = \\ &= \Phi + \omega_c\tau + \omega_c \sum_i L_i \left(\left. \frac{\partial k_i}{\partial \omega} \right|_{\omega_c} - \frac{k_i}{\omega_c} \right) \end{aligned}$$

Taking the derivative with respect to energy and choosing a representation with a fixed carrier frequency, we then obtain the following expression for the carrier envelope shift:

$$\frac{\partial \Delta\Phi_{CE}}{\partial W} = \frac{\partial \Phi}{\partial W} + \omega_c \frac{\partial \tau}{\partial W} = -0.06 \text{ rad/nJ} + 0.23 \text{ rad/nJ} = 0.17 \text{ rad/nJ}$$

Our numerical evaluation leads to unique values for the nonlinear phase shift Φ and the nonlinear timing shift τ for each pulse energy: The phase shift increases with higher energies, as the self-phase modulation gets stronger, from about $-\pi/2$ to $3\pi/2$ for energies between 20 - 70 nJ. The timing shift varies from 3 fs to 8 fs (see 5). In both cases, linear relationships with

respect to the pulse energy are found, which are characterized by slopes of different magnitude and opposite sign. The timing shift derivative of 0.23 rad/nJ is four times larger than the nonlinear phase shift contribution of -0.06 rad/nJ, and the effects partially compensate for each other. Comparing this result with studied soliton lasers, a factor of 2 between the timing shifts and the nonlinear phase contribution was determined by Haus and Ippen [6]. This reduced nonlinear phase in dispersion managed lasers can be explained by pulse breathing, which reduces the peak pulse intensity within the Ti:sapphire crystal so that smaller nonlinear phase shifts are accumulated.

We demonstrated that a one-dimensional numerical analysis, including mirror characteristics and the higher-order dispersion of the intracavity elements, can accurately describe the laser dynamics of octave-spanning lasers that generate sub-two-cycle pulses. By optimizing the dispersion compensation and including the measured mirror reflectivity and group delay, we can predict the best achievable performance in terms of output spectrum, the enhancement of spectral wings, and achievable output pulse shape and duration in an actual experimental setup. In addition, the carrier envelope phase dynamics were analyzed and it was found that the dominant contribution arises from nonlinear timing shifts. In conclusion, the presented numerical model is a powerful tool for the analysis, design, and optimization of laser components and the general design of octave-spanning lasers.

References

1. Y. Chen, F. X. Kärtner, U. Morgner, S. H. Cho, H. A. Haus, E. P. Ippen, J. G. Fujimoto, "Dispersion-managed mode locking," *J. Opt. Soc. Am. B* **16**, 1999–2004 (1999).
2. H. M. Crespo, J. R. Birge, M. Y. Sander, E. L. Falcão-Filho, A. Benedick, and F. X. Kärtner, "Phase stabilization of sub-two-cycle pulses from prismless octave-spanning Ti:sapphire lasers," *JOSA B* **25**, B147–B154 (2008).
3. M. Y. Sander, J. Birge, A. Benedick, H. M. Crespo, F. X. Kärtner, "Dynamics of Dispersion Managed Octave-Spanning Titanium:Sapphire Lasers," *JOSA B* **26**, 743–749 (2009).
4. M. Y. Sander, H. M. Crespo, J. R. Birge, and F. X. Kärtner, "Modeling of Octave-Spanning Sub-Two-Cycle Titanium:Sapphire Lasers: Simulation and Experiment," *Conference on Ultrafast Phenomena*, (European Physical Society and Optical Society of America, 2008), THU11c.
5. M. Y. Sander, E. P. Ippen and F. X. Kärtner, "Carrier-Envelope Phase Dynamics of Octave-Spanning Titanium:sapphire Lasers," *Conference on Lasers and Electro Optics (CLEO)*, Baltimore, MD, June 1-5, 2009, CMN4.
6. H. A. Haus and E. P. Ippen, "Group velocity of solitons," *Opt. Lett.* **26**, 1654–1656 (2001).

HeNe-CH₄ based Frequency Combs and Clocks Based on an Octave Spanning 1GHz Ti:sapphire Oscillator

Sponsors

Defense Advanced Research Projects Agency (DARPA)

Project Staff

Andrew Benedick, Jonathan Birge, Dr. Peter Fendel, Li-Jin Chen, Dr. Oliver D. Mücke, Dr. Richard Ell, Michelle Sander, Professor Franz X. Kärtner

Over the last ten years, frequency combs have emerged as powerful tools for molecular and atomic spectroscopy, astronomical spectrograph calibration, and as low phase noise radio frequency master oscillators. As compared to lower repetition rate fiber and other solid state lasers, high repetition rate Ti:sapphire oscillators need no additional external broadening and the large mode separation enables easier access of the individual comb lines with more power per mode.

We demonstrate here a greatly improved octave spanning 1-GHz Ti:sapphire laser [1] using the most broadband double-chirped mirror pairs, optimized Kerr-Lens modelocking (KLM) and an optimized output coupler. As a result, the laser generates, at 9 W of pump power, 0.6 W – 1 W of output power with an output spectrum of more than one octave as measured on a linear scale, see Fig. 1 (a). The spectrum corresponds to a Fourier limited pulse of 3.5-fs duration. Second harmonic generation with this output in 1 mm of LBO directly generates 1f-2f beatnotes for carrier-envelope phase stabilization with >55 dB signal-to-noise (SNR) in 100 kHz bandwidth [Fig. 1 (b), top trace]. Using the central part of the output spectrum, difference frequency generation (DFG) in a 5-mm long PPLN generates radiation at 3.39 μm . The 3.39- μm radiation is strong enough to result in a beatnote with a single frequency HeNe reference laser of 30 dB, [Fig. 1 (b), bottom trace]. This laser will serve as the clockwork of the HeNe CH₄-based molecular clock [2] with a measured Allan variance approaching 10^{-14} in 100 s and as an absolute femtosecond laser frequency comb for an optical arbitrary waveform generator.

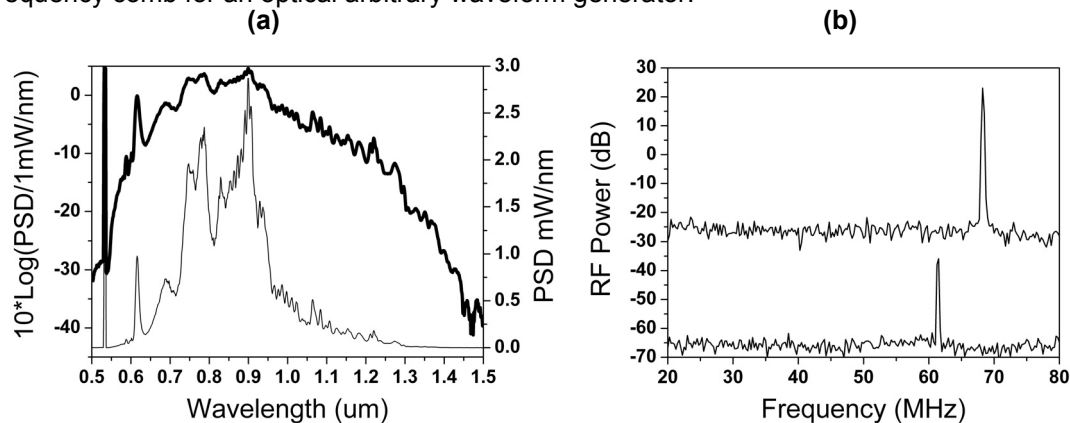


Figure 1: (a) Output spectrum of the 1GHz Ti:Sapphire laser on a logarithmic (top) and linear (bottom) scale, (b) 1f-2f beatnote (top) and 3.39 μm beatnote with HeNe reference laser (bottom).

The laser is a standard KLM four mirror Ti:sapphire ring laser with a 1-GHz repetition rate. The mirrors are double-chirped mirror pairs (DCMPs) and provide precise dispersion compensation together with two thin pieces of BaF₂, a plate and wedge, both inserted at Brewster's angle. Output coupling is achieved by coating one side of the BaF₂ wedge with a coating designed to give 4% output coupling in the center of the spectrum, increasing to >50% output coupling above 1050 nm and below 650 nm. With 9 W of pump power, 600 mW of output power with a FWHM spectrum of >200 nm is achieved (Fig. 1). With the same output coupler coating on a fused silica wedge, more than 1 W output power is extracted with slightly reduced spectral wings.

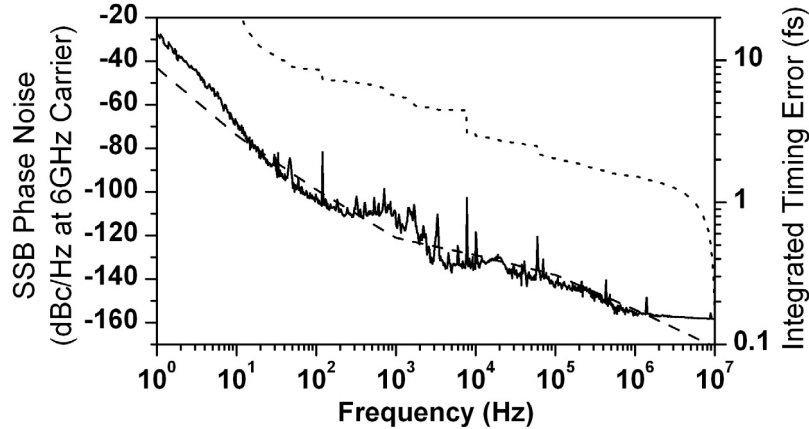


Figure 2. Phase noise measurement of the 6th harmonic of the stabilized Ti:Sapphire's output pulse train using an Agilent 5052A signal source analyzer. The solid line is the measurement result, the dashed line is the instrument's published noise floor, and the dotted line is the integrated phase error starting at 10 MHz.

Phase noise measurement of the pulse repetition rate was made using an Agilent 5052 signal source analyzer, yielding an integrated phase error of less than 10 fs for time periods of more than 0.02 s, limited currently by the measurement device. By using the optical cross correlation technique we expect to measure attosecond level timing instability. The time domain stability of the frequency comb was measured by heterodyning one line of the frequency comb against a diode laser stabilized to a ultra low expansion (ULE) cavity. Using this method we were able to measure the Allan Deviation of the optical spectrum of the frequency comb to be 3×10^{-14} at 20 s gate times. Due to the instability of the ULE cavity used in the comparison, the ultimate performance of the frequency comb is not currently measurable, though it is expected to match the performance of the methane stabilized reference laser, yielding an ultimate stability of 1×10^{-14} at 100 s gate time.

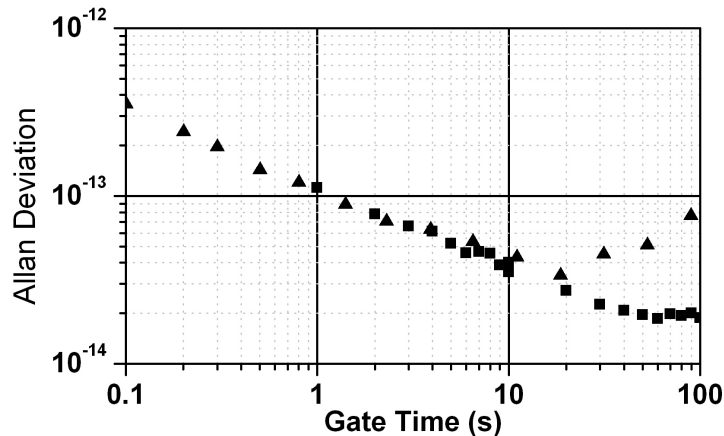


Figure 3. Results of heterodyne type Allan Deviation measurements between the 1-GHz Ti:Sapphire frequency comb system and a ULE cavity stabilized laser diode (triangles), and between two identical CH₄ stabilized HeNe lasers (squares). The divergence of the two traces beyond 20 s is due to uncompensated temperature drifts of the ULE cavity laser.

References

1. A. Benedick, D. Tyurikov, M. Gubin, R. Shewmon, I. Chuang, F. X. Kärtner, "Compact, Ti:sapphire based methane-stabilized optical molecular frequency comb and clock" *Optics Letters* 34 (14): 2168-2170 JUL 15 1 2009.
2. S. Foreman, A. Marian, J. Ye, E.A. Petrukhin, M.A. Gubin, O.D. Mücke, F.N.C. Wong, E.P. Ippen, F.X. Kärtner "Demonstration of a HeNe/CH₄-based optical molecular clock," *Optics Letters* 30 (5): 570-572 MAR 1 2005.

Blue Astro-Comb for Precision Calibration of Astrophysical Spectrographs

Sponsors

Defense Advanced Research Projects Agency (DARPA)

Project Staff

Guoqing Chang, Andrew J. Benedick, Chih-Hao Li, Peter Fendel, Alexander G. Glenday, Franz X. Kärtner, David F. Phillips, Dimitar Sasselov, Andrew Szentgyorgyi & Ronald L. Walsworth

An astro-comb is a broadband optical frequency comb generated from a mode-locked femtosecond laser (known as a “comb-laser”) that is filtered to have the appropriate spectral spacing between comb lines for use with a high-performance astronomical spectrograph, and locked to an atomic clock for long-term stability [1]. Recently, we have developed a Ti:sapphire laser based astro-comb with a stability allowing calibration of astrophysical spectrographs to 1 cm s^{-1} sensitivity². The power of this capability is not limited to exoplanet research – it will open up new discovery space over a broad cross-section of astrophysical problems, including the nature and dynamics of dark energy, as well as the constancy of fundamental constants over cosmological time scales. The first astro-comb operates in the red, $\sim 750\text{--}950 \text{ nm}$, and is well-suited to exoplanet searches around M-dwarf stars. To detect and characterize exoplanets around solar-type host stars, astro-combs at a visible wavelength range are required. Our current effort is to develop a blue astro-comb that covers $\sim 15 \text{ nm}$ bandwidth centered at 420 nm .

The blue astro-comb setup is shown schematically in Fig. 1. The IR-comb covers a spectrum of more than one octave with both the carrier-envelope offset frequency and the repetition rate referenced to frequency standards. Two double-chirped mirrors and a piece of fused-silica plate remove the residual chirp of the near-IR comb to shorten the comb’s pulse duration, which in turn maximizes the frequency-doubling efficiency. A parabolic mirror with a 1-inch focal length focuses the IR light to have a beam waist of $\sim 20 \mu\text{m}$ in a 1-mm thick BBO crystal used for frequency-doubling. Efficient generation of the blue comb via frequency-doubling requires phase-matching between the input IR comb light and the desired output blue comb light. At one particular incident angle, a narrow spectral band ($\sim 15 \text{ nm}$) of the comb satisfies the phase-matching condition. For example, the blue comb spectrum centered at $\sim 420 \text{ nm}$ has an average power of 20 mW , corresponding to $\sim 5\%$ power-conversion efficiency of the 400 mW input near-IR comb light.

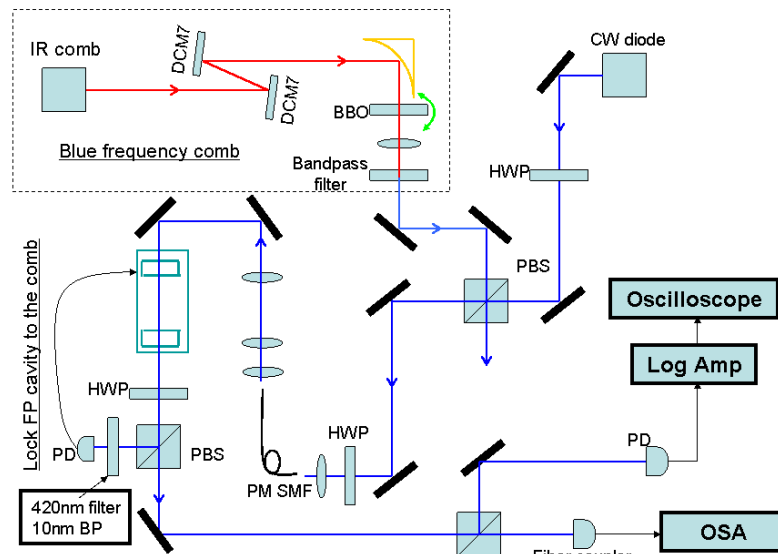


Figure 1. Block diagram of the experimental setup. The stabilized 1-GHz frequency comb emitted from a femtosecond laser passes through a BBO crystal that converts the initial IR comb to a blue comb. The comb-line spacing of this 1-GHz blue comb is increased up to 23 GHz using an FP cavity to filter out unwanted comb lines. The FP cavity is locked to the blue comb. A blue CW diode together with log amplifier, oscilloscope, and OSA quantify the FP cavity’s performance, such as its finesse, linewidth, and side-mode suppression. OSA: optical spectrum analyzer; HWP: half-wave

plate; DCM: double-chirped mirror; PM SMF: polarization-maintaining single-mode fiber; PBS: polarizing beam splitter; PD: photo-diode.

The frequency-doubled blue comb light is collimated by a lens and the residual near-IR comb light filtered by a bandpass filter. A polarization-maintaining single-mode fiber delivers the blue source-comb light to pass through a Fabry-Perot (FP) cavity that filters out unwanted comb lines and increases the line spacing from 1 GHz to 23 GHz. The FP cavity is locked and therefore stabilized to the blue source-comb. The mirrors used in the plane-parallel FP cavity have $\sim 99\%$ reflectivity and optimized group delay dispersion (GDD) ($< 2 \text{ fs}^2$) in the range of 400 nm to 440 nm. To characterize the FP cavity, a CW diode laser operating at 408 nm is combined with the blue comb light via a polarizing beam splitter. Sweeping the wavelength of the diode laser and recording its transmission through the FP using a logarithm amplifier allows us to map out the FP cavity's transmission function over one free-spectral-range. Fig. 2 (a) plots the measured transmission function within 17 GHz range. The measured single-sided suppression of extraneous comb lines of more than 25 dB is consistent with the measured FP cavity finesse of 200. Fig. 2 (b) shows the blue astro-comb spectrum with 15-nm bandwidth (full-width at half maximum) as the FP cavity is locked to the blue source-comb. It is worth noting that such a spectrum is measured with an optical spectrum analyzer that has the minimum resolution of 0.05 nm, i.e. $\sim 90 \text{ GHz}$. This resolution is not fine enough to resolve each individual astro-comb line with spacing of 23 GHz.

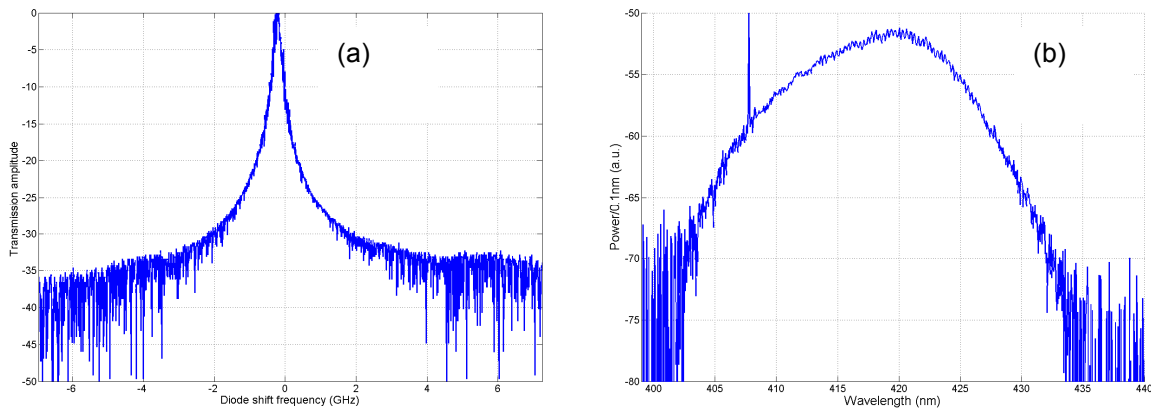


Figure 2. (a) Measured transmission function of the FP cavity. The FP cavity is tuned such that the astro-comb has a 25-GHz line spacing. (b) OSA measured optical spectrum at the output of the FP cavity. The sharp spike corresponds to the CW diode wavelength.

Future work includes: 1) resolve individual lines of the blue astro-comb using Fourier transform spectroscopy (FTS) of 3-GHz resolution, which also enables us to measure the dispersion of the FP cavity; 2) achieve broadband frequency doubling and construct a broadband FP cavity to implement an astro-comb at visible wavelength range with $> 100 \text{ nm}$ coverage; 3) deploy the blue astro-comb at Mt. Hopkins, Arizona for calibration runs to unequivocally demonstrate the use of a blue astro-comb for precise-radial-velocity measurements of solar type stars.

References

- [1] M.T. Murphy, et al., "High Precision wavelength calibration with laser frequency combs," *Mon. Not. R. Astron. Soc.* 380, 839-847 (2007).
- [2] C.H. Li et al. "A laser frequency comb that enables radial velocity measurements with a precision of 1 cm s^{-1} ," *Nature* 452, 610-612 APR 3 2008.

Erbium Fiber Laser Repetition Rate Lock to a Methane-Stabilized HeNe Reference

Sponsors: DARPA Contract HR0011-05-C-0155, AFOSR Contract FA9550-07-1-0014

Project Staff:

David Chao, Noah Chang, and Professor Erich P. Ippen

Significant progress has been made in locking the 250 MHz repetition rate (f_{rep}) of our fiber laser to a methane-stabilized HeNe reference laser. A generalized schematic of the system is depicted in Fig.1. The output of the mode-locked Erbium fiber laser (ErFL) is amplified and compressed, then sent into a short piece of highly nonlinear fiber (HNLF) to produce a spectrum broad enough to generate a difference frequency (DFG) of 3.39 μm . The 3.39 μm DFG signal is then beat with the 3.39 μm HeNe reference on a liquid-nitrogen-cooled InSb detector resulting in a RF signal which will be locked to a stable RF oscillator. Previously, we reported a beat note with ~ 15 dB SNR, which was not sufficient for locking. We have since increased the beat's SNR to ~ 25 dB by inserting a HeNe discharge tube to amplify the DFG signal (see Fig.2).

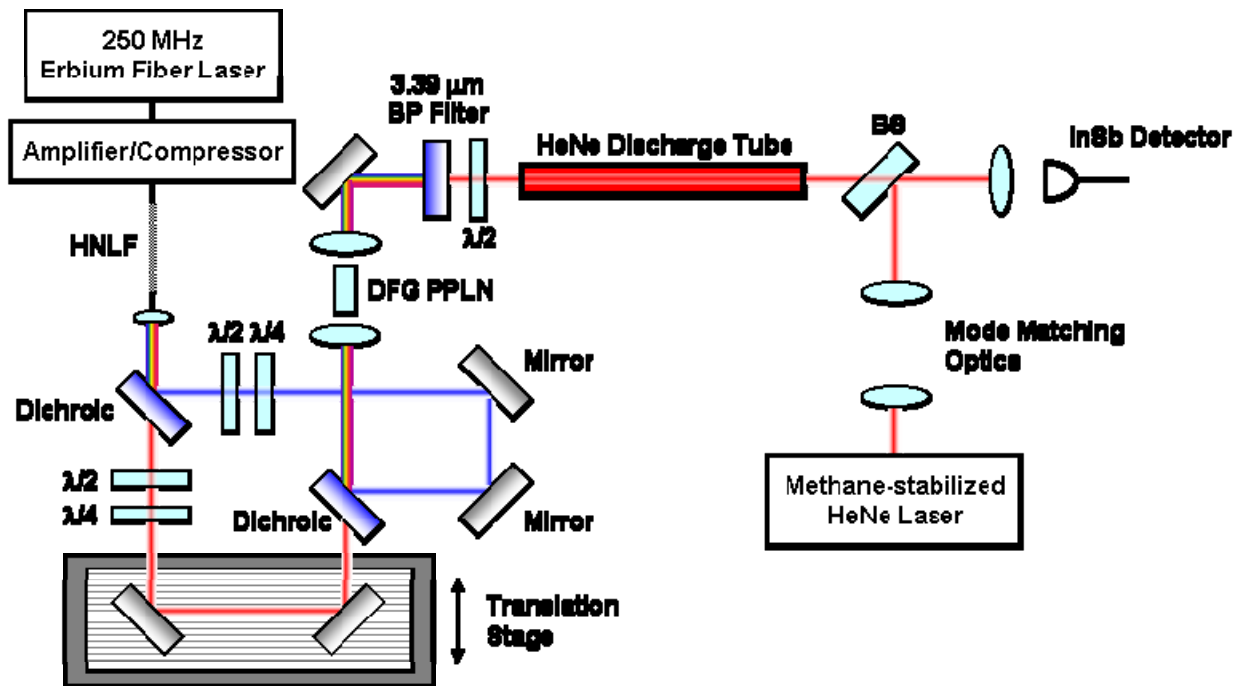


Figure 1

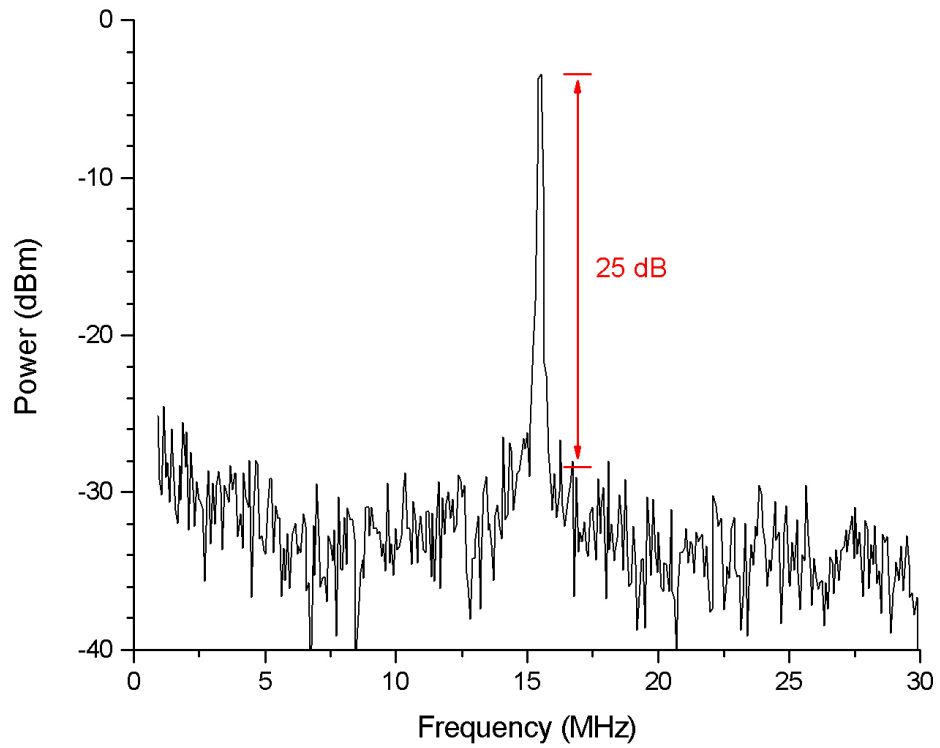


Figure 2

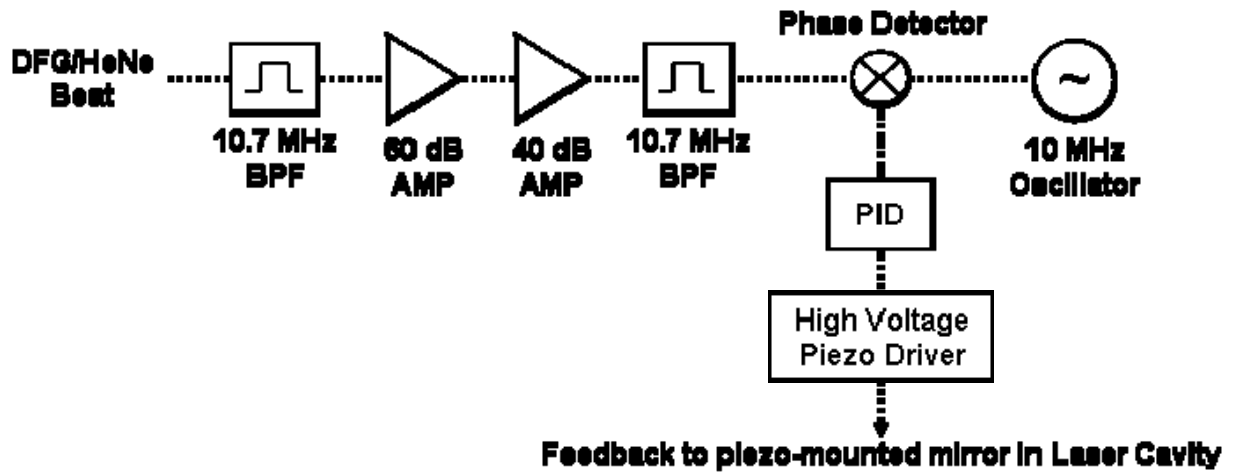


Figure 3

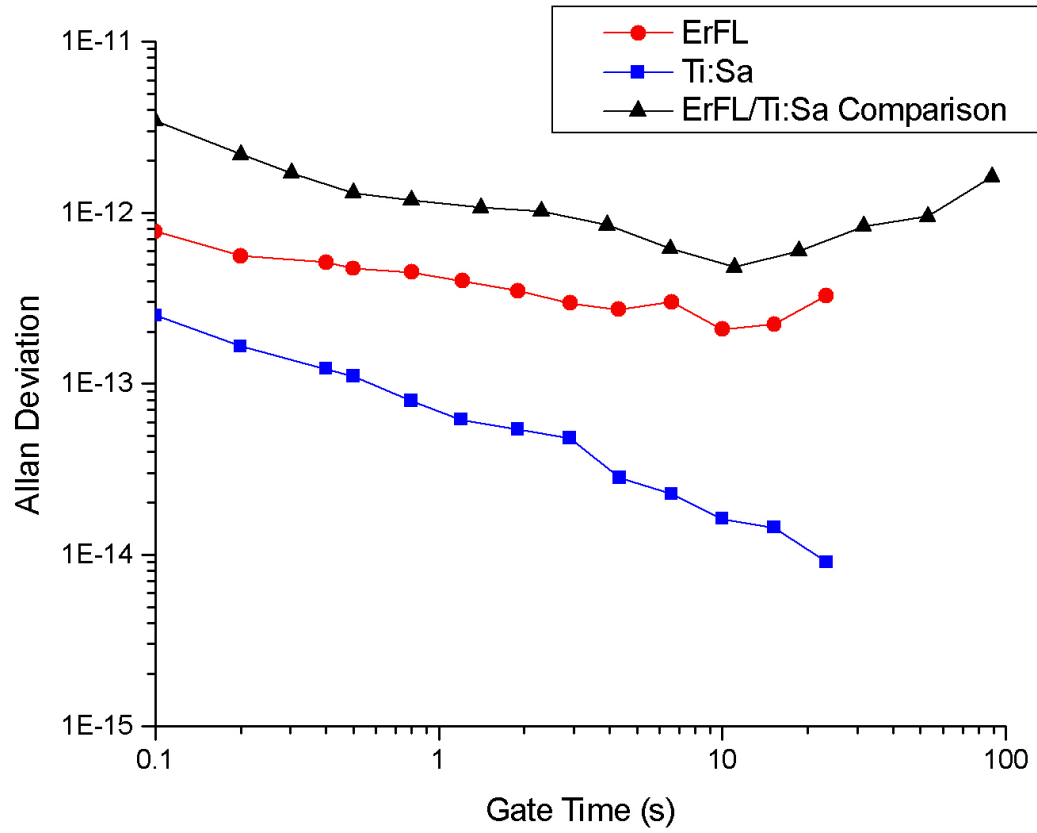


Figure 4

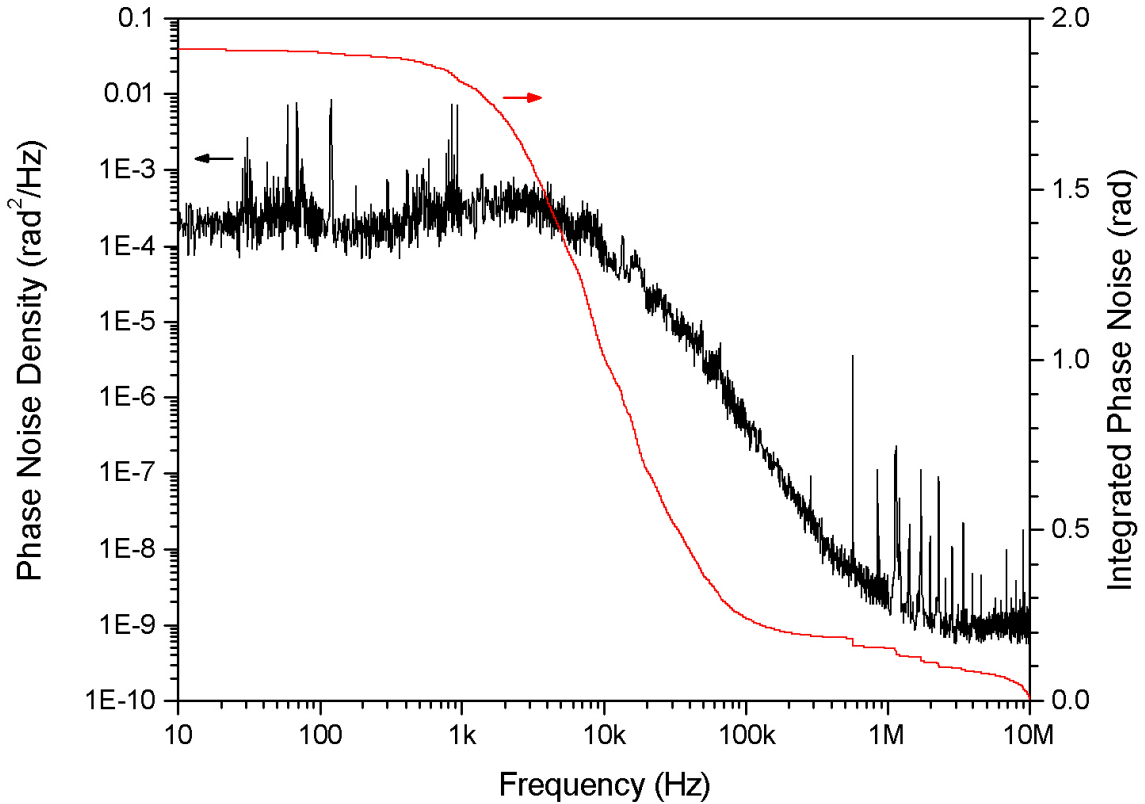


Figure 5

The resulting increase in SNR allows the beat to be locked to a stable RF oscillator (SRS DS345) using the feedback loop setup shown in Fig.3. The phase detector measures the phase difference between the beat signal and RF oscillator, and gives an error signal which is subsequently filtered and amplified so that it can drive a piezo-mounted end mirror in the laser cavity.

Since our frequency counters don't have enough precision to directly measure the stability of f_{rep} , we do so indirectly by measuring the stability of the beat signal. Fig.4. shows that the stability of the beat signal was measured to be as good as 2.1×10^{-13} at a 10 s gating period. Fig.4. also shows the stability of a similarly-locked Ti:Sa laser, and a comparison between the two lasers. Note that the carrier-envelope offset frequency (f_{ceo}) was not locked for either laser in these experiments – this in itself may be limiting the stability measurements.

Furthermore, an in-loop phase noise measurement was taken to help analyze the phase lock (see Fig.5). The integrated phase noise is ~ 1.9 rad. Note that the low frequency phase noise is suppressed up to ~ 8 kHz, which is the locking bandwidth of our feedback loop. Beyond this, the phase noise density follows that of the free-running oscillator. Future work will focus on increasing the bandwidth of this feedback loop, as we believe this to be the main limitation to obtaining a better lock. This will mean modifying the high-voltage piezo driver, and possibly the piezo/mirror assembly, to optimize their bandwidths. We expect to obtain a locking bandwidth of >40 kHz, which would correspond to an integrated phase noise of <0.69 rad. If we can achieve a locking bandwidth of >80 kHz, then the integrated phase noise would be <0.37 rad.

High-Power High-Repetition-Rate Femtosecond Fiber Amplifier Development

Sponsors: DARPA Contract HR0011-05-C-0155, AFOSR Contract FA9550-07-1-0014

Project Staff:

David Chao, Noah Chang, and Professor Erich P. Ippen

Our previous work on femtosecond pulse amplifiers focused on providing enough amplification and compression to generate octave-spanning supercontinuum at 200 MHz repetition rates, as 200 MHz was our highest repetition rate fundamentally modelocked laser at the time. These amplifiers relied on four 980 nm laser diodes (each outputting 500 mW) to provide the pump powers necessary for amplifying the 200 MHz pulse train to average powers greater than 300 mW (1.5 nJ pulse energy). Amplifiers based on this concept are close to reaching their limit, as it becomes increasingly difficult to make even small improvements (i.e. a lot of work for marginal gain). Therefore, in order to achieve octave-spanning supercontinuum at GHz repetition rates, a different pump technology will be investigated -- a Raman fiber laser operating at 1480 nm. Raman fiber lasers are typically constructed from Yb fiber lasers centered around 1 μm . The output of the Yb fiber laser is then sent through a cascade of nested fiber Bragg gratings designed to precisely shift the laser wavelength by several Raman orders up to 1480 nm. The high powers achievable with Yb fiber lasers translate to Raman fiber lasers capable of outputting tens of Watts of singlemode power at 1480 nm.

The higher pump powers provided by Raman fiber lasers allow for the development of higher power amplifiers, making octave-spanning supercontinuum possible at higher repetition rates -- the goal being to reach GHz repetition rates (since there has been tremendous progress on the development of fundamentally modelocked oscillators operating at GHz repetition rates). The current amplifier is being designed for an input pulse train with 1 GHz repetition rate. Preliminary results from the 1 GHz oscillator (which will be used to seed the amplifier) indicate output pulses with ~ 10 pJ energies and ~ 500 fs durations. These pulses will need to be amplified up to ~ 1 nJ energies and compressed down to ~ 100 fs durations in order to generate octave-spanning supercontinuum (as we previously demonstrated using OFS HNLf Type B) -- this means an amplifier providing >20 dB gain is needed (along with 5x pulse compression).

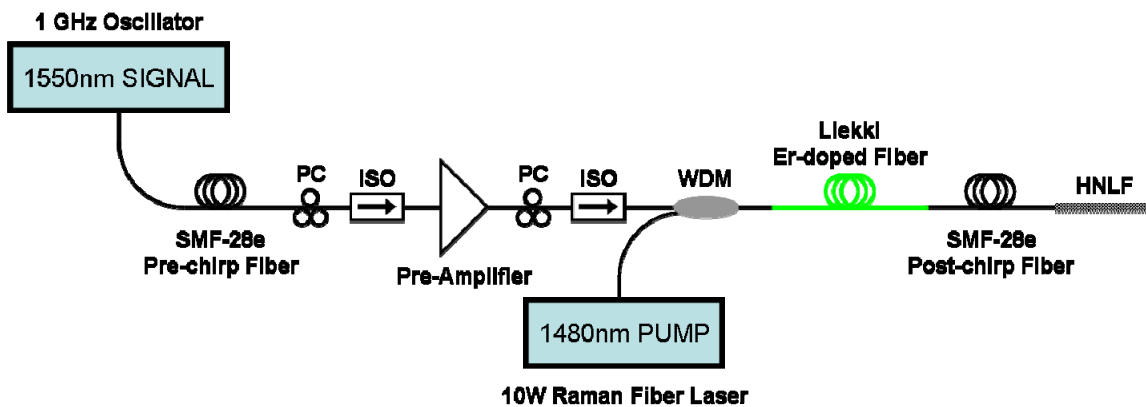


Figure 1: Femtosecond pulse amplification and compression setup for 1 GHz repetition rate pulse trains. The system is designed to output sub-100 fs pulses with nJ energies.

The amplifier/compressor setup depicted in Figure 1 is designed to output over a Watt of average power, while simultaneously compressing pulses down to sub-100 fs durations. Since the 1 GHz oscillator mentioned above is still under development, a pseudo-1-GHz source constructed from an interleaved 250 MHz pulse train is used to seed the amplifier. The amplifier section of the system consists of two stages -- a pre-amplifier followed by a power amplifier. The pre-amplifier stage amplifies the <10 mW input seed power up to ~ 60 mW using a 50 cm piece of Liakki 110

dB/m Er-doped gain fiber pumped with a single 980 nm laser diode providing 500 mW of pump power. The output of the pre-amplifier is sent into an additional 1.5 m of the same Liekki 110 dB/m Er-doped gain fiber, but this time pumped with a 1480 nm Raman fiber laser capable of providing up to 10 W of pump power. Figure 2 shows the performance of the amplifier at various pump powers, from which we observe a slope efficiency of 17%.

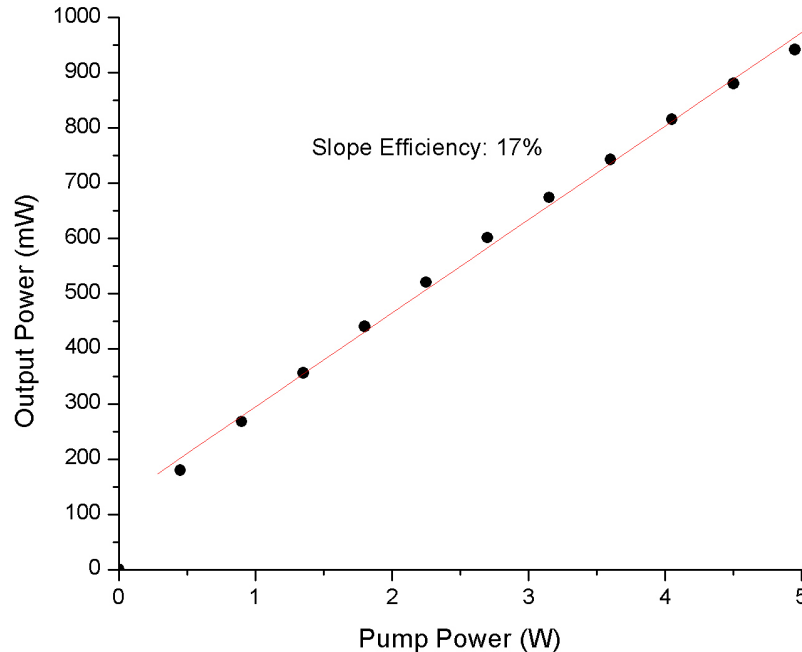


Figure 2: Output performance of the amplifier for different pump powers.

Pulse compression is accomplished through the optimization of pre- and post-chirp fiber lengths. A segment of anomalous dispersion pre-chirp fiber (SMF-28e) is inserted before the pre-amplifier to minimize nonlinearities in the beginning stages of amplification. The amount of pre-chirp is carefully optimized so that the pulses compress back to their transform limit near the end of the amplifier, where they will experience intense nonlinearities and thereby generate spectrum to compensate for gain narrowing during the amplification process. It is important that the gain fiber be chosen to have normal dispersion, as this leads to SPM-dominated spectral generation whereby the resulting chirp is linear and compressible. To compensate for the SPM-induced normal chirp (as well as the normal dispersion of the gain fiber), an appropriate length of SMF-28e post-chirp fiber is used to ensure the pulses are fully compressed before they are sent into HNLFF for supercontinuum generation (alternatively, a pair of Si prisms can be used in place of the post-chirp fiber if pulse distortion/breakup in the fiber becomes significant). Note that this approach to pulse compression is similar to that employed in our previous generation amplifier/compressor systems. And since the pulse energies generated in this amplifier/compressor are comparable to the pulse energies generated in those systems, obtaining sub-100 fs pulses should be relatively straightforward using the above-described compression scheme.

The goal of this amplifier/compressor system is to produce sub-100 fs, nJ pulses at a 1 GHz repetition rate, as pulses with similar durations and energies have been used previously to generate octave-spanning supercontinuum with UV-exposed small-core silica HNLFF from OFS (i.e. OFS HNLFF Type B). We hope to achieve octave-spanning supercontinuum at a 1 GHz repetition rate in the very near future.

Long-term, ultrafast, fiber optic timing distribution with polarization maintaining output

Sponsors

Air Force Office of Scientific Research (AFOSR) FA9550-06-1-0468

EuroFEL

Office of Naval Research (ONR) N00014-02-1-0717

University of Wisconsin

Project Staff

Jonathan A. Cox, Dr. Jungwon Kim and Professor Franz X. Kärtner

Ultrafast optical timing distribution with optical fiber allows for the precise synchronization of many distant points in space. Femtosecond-performance timing synchronization greatly aids the development of next-generation time and phase-sensitive systems, such as X-ray free electron lasers (XFEL) [1]. In particular, ultrafast timing distribution of the pulse train from a low-noise, modelocked laser transmits the entire frequency comb, providing not only an ultrafast optical signal for laser-to-laser synchronization, but also the RF harmonics for laser-to-RF synchronization. Furthermore, by using a periodically poled KTP (PPKTP) balanced cross-correlator for timing measurement, we achieve immunity to temperature- and amplitude-to-phase conversion, which is a limiting factor for direct, photodiode detection schemes. To provide continuous femtosecond-level timing distribution, we have integrated polarization maintaining fiber outputs with an intra-link polarization control feedback system. As a result, we have demonstrated an ultrafast timing distribution system with two, 300-meter long fiber links capable of long-term stable operation with precision of 2 fs rms over 24 hours of operation.

The system operates by stabilizing the total group delay of a dispersion compensated single mode fiber (SMF) link with a motorized free space delay and a piezoelectric fiber stretcher, as shown in Fig. 1. In this way, a ~ 100 fs pulse train from a 200-MHz fiber laser is delivered across 300 meters of fiber. Measurement of the optical delay is made by performing an optical cross-correlation between a new pulse entering the link from the laser and an old pulse that was reflected back from the end of the link by the 50 percent faraday rotating mirror (FRM). This cross-correlation is performed with a PPKTP balanced cross-correlator, providing a measurement of the delay between the two pulses. This error signal, in turn, drives the loop filter that controls the fiber stretcher in order to remove the fast fiber length fluctuations. The closed-loop bandwidth of this system is approximately 1 kHz, which is sufficient to eliminate the vast majority of thermal and acoustic fiber fluctuations. The motor controller monitors the loop filter output and adjusts the free space delay to keep the loop filter in range. In addition, an in-loop Erbium-doped fiber amplifier (EDFA) is implemented to overcome the link losses. The output of the EDFA is fed into a polarization controlling feedback system which maintains constant polarization into the polarization maintaining (PM) fiber that connects to the FRM outputs.

To assess the performance of the system, we built two independent and nearly identical timing links, based on the previously reported design [4]. The output of both links was then compared with a third out-of-loop cross-correlator to determine the relative timing drift and jitter between the two outputs. Fig. 2 shows the fiber spool temperature, motor delay and residual timing drift as measured by the out-of-loop cross-correlator. The motor delay reveals the actual fiber drift which the system corrects for, largely from slow thermal fluctuations. The residual timing drift between the two links remains within 11 fs pk-pk, or 2.2 fs rms for a 24 hour period.

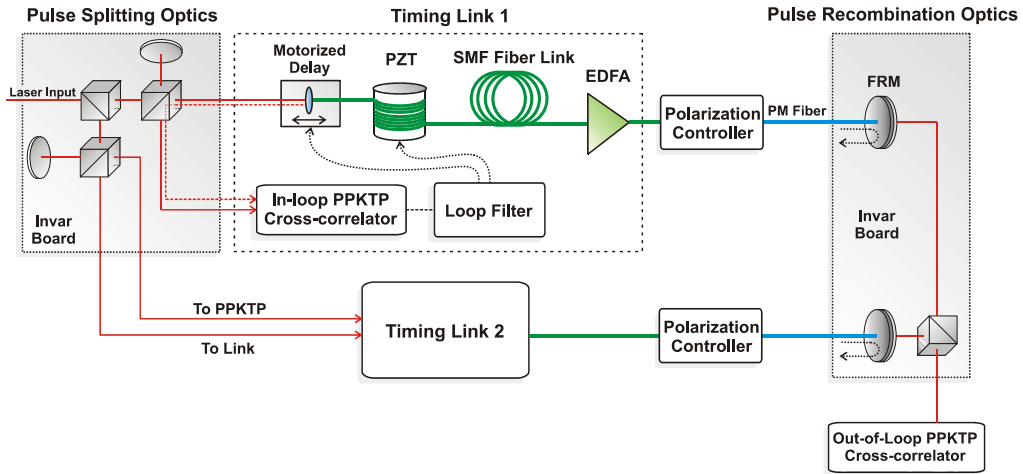


Figure 1: A schematic representation of the dual timing distribution with polarization maintaining outputs used for out-of-loop drift measurements between independent links.

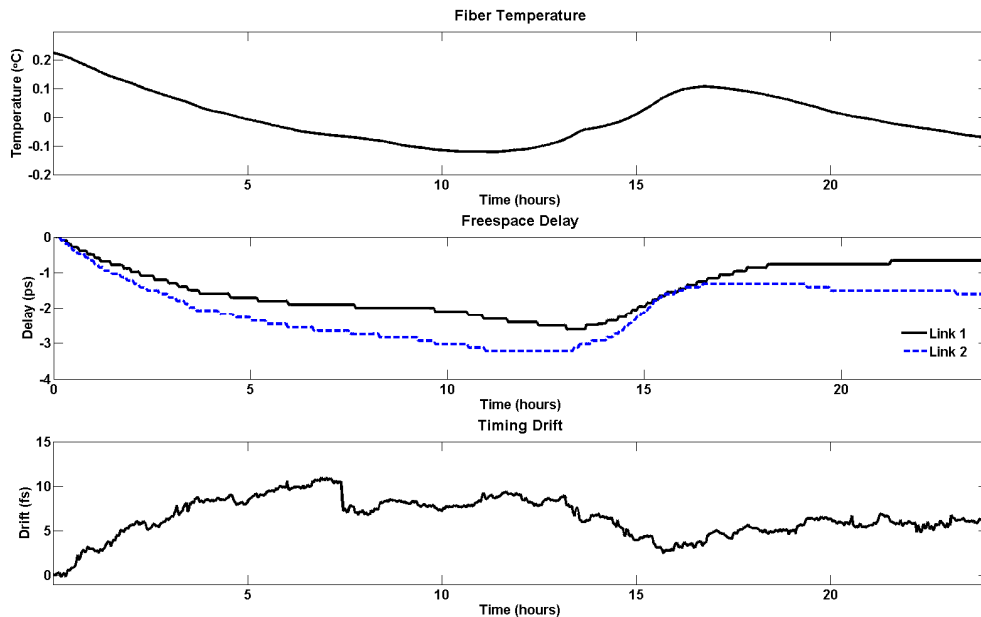


Figure 2: The experimental results of the 300 meter, polarization maintaining timing link test are shown above for 24 hours of operation. The top plot shows the temperature of the fiber spools. The center plot shows the associated group delay drift of the fiber link which was corrected for by the motors. The residual out of loop timing drift of 2.2 fs rms or 11 fs pk-to-pk, over 24 hours, is shown in the lower plot.

While non-linearity is well managed in the timing link with the aid of a high-repetition rate laser, polarization mode dispersion (PMD) is the primary limiting factor for link performance. The current system employs bare fiber wound around plastic spools. As such, fiber bending and stress is greatly exaggerated from typical operating conditions. As a result, the PMD is much greater than the nominal value specified by Corning for SMF-28e fiber of $60 \text{ fs}/\sqrt{\text{km}}$.

Figure 3 shows the PMD measured in the timing link. By inserting a birefringent element at the free-space input to the fiber link, while the link and polarization controllers are locked, we can vary the input polarization state. Concurrently, the output drift can be observed as a function of input polarization state since the polarization controllers restore linear polarization while the waveplate is rotated.

The test was performed for both elliptical and linear launched polarization states. By rotating a quarter-wave plate, the ellipticity was varied. By rotating the half-wave plate, the linear polarization was rotated. Fig. 3 shows the polarization state at the end of the fiber link, but before the polarization controller. From the observed drift for both elliptical and linear states, it is clear that the differential group delay (DGD) between polarization states is approximately 200 fs pk-pk.

The discrepancy in PMD has been positively attributed to winding bare fiber around a fiber spool. We have previously observed an approximately three-fold reduction in PMD and link-drift by more loosely winding the fiber about the spool. Furthermore, DGD measurements conducted at the Fermi in Trieste, Italy demonstrated that the piezo fiber stretcher, which consists of 43.7 meter of fiber, has 83 fs of DGD. The DGD of 14 meters of dispersion compensated fiber (DCF) was found to be 2 fs, or at the noise floor of the measurement apparatus. As such, it is clear that the predominant source of drift is PMD from the piezo fiber stretcher, which can be eliminated in favor of a free space delay, a PM fiber stretcher, or by simply reducing the amount of fiber in the stretcher.

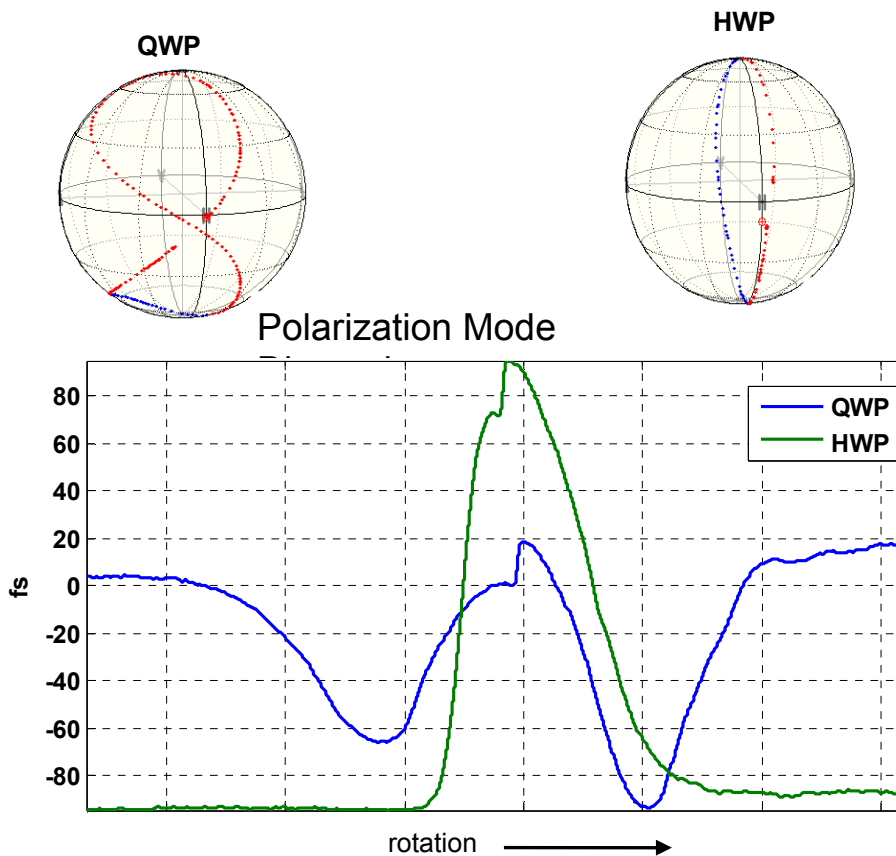


Figure 3: Timing drift due to polarization mode dispersion as a function of launched polarization state for both elliptical (QWP) and linear (HWP) states. The upper Poincaré sphere diagrams show the resulting polarization state at the end of the link, before being corrected by the polarization controller. The lower plot shows the timing drift resulting from a change in launched polarization state for both linear and elliptical states while the system is locked.

References

- J. Kim, J.A. Cox, F.X. Kaertner. "Drift-free femtosecond timing synchronization of remote optical and microwave sources," *Nat. Photon.* 2, 733-736 (2008).
 J. Kim, J. Chen, Z. Zhang, F. Wong, F. Kaertner. "Long-term femtosecond timing link stabilization using a single-crystal balanced cross correlator," *Opt. Lett.* 32, 1044 (2007).

Spatial Hole Burning in Actively Mode-locked Quantum Cascade Lasers

Sponsors: DARPA Contract HR0011-05-C-0155, AFOSR Contract FA9550-07-1-00

Project Staff

Vasileios-Marios Gkortsas, A. Gordon, C. Jirauschek, C. Wang, L. Kuznetsova, L. Diehl, M. A. Belkin, A. Belyanin, F. Capasso and Franz X. Kärtner

Short pulse generation from Quantum Cascade Lasers (QCLs) emitting in the mid-infrared wavelength region (3.5-20 μm) could serve many applications, ranging from time-resolved spectroscopy, nonlinear frequency conversion, high-speed free space communication to frequency metrology [1]. QCLs, directly electrically-pumped sources, potentially can generate sub-picosecond mid-infrared laser pulses over a wide wavelength range, due to the flexibility offered by band structure engineering. However, short pulse generation from QCLs by mode locking is difficult due to the fast gain recovery time of QCLs, typically in the few picosecond range, which acts as an inverse saturable absorber driving pulse formation inherently unstable [2]. Therefore, most recently, QCLs with a long upper state lifetime, by implementing a "superdiagonal" gain structure design [3], have been fabricated. These show upper state lifetimes of 50 ps, similar to the cavity roundtrip time (40-70 ps), and active mode locking with isolated pulses has been achieved [4]. In our work, we analyze the stability of mode locking in these lasers by numerical simulations and demonstrate that spatial hole burning (SHB), also considerably reduced in influence due to the long upper state lifetime, is still strong enough to enable multimode lasing over an increased wavelength range in comparison to the case without SHB. However, as has been observed in actively mode-locked solid-state lasers, strong SHB results in incomplete mode locking.

To demonstrate the impact of SHB, the QCL gain structure is modeled as an open two-level system described by Bloch equations and the pulse propagation through the gain medium situated in the Fabry-Perot cavity is described by a one-dimensional wave equation [2]. We assume a homogeneously broadened gain medium with energy recovery time of $T_1=50$ ps and a dipole dephasing time of $T_2=50$ fs. The cavity is 2.6 mm long (refractive index $n \approx 3.2$) and has a short, 240 μm long, electrically isolated section at the begin of the cavity. The short section and the rest of the cavity are equally strong continuously pumped (DC pumping). Active mode locking is achieved by sinusoidal modulation of the pump current injected into the small section at the round-trip frequency of the passive cavity, which is 17.86 GHz. No other nonlinear effects are included. Output coupling occurs via the front uncoated facet of the semiconductor Fabry-Perot cavity.

Fig. 1 shows the intensity profile and interferometric autocorrelation (IAC) traces for the QCL, with parameters discussed above, if SHB is neglected in the Maxwell-Bloch equations describing the laser dynamics. The DC pumping parameter is set to 1.1, 1.45 and 1.61 times the threshold current and we keep the amplitude of the modulation term constant (5 times the threshold value). Note, since the modulation frequency is already close to the inverse gain recovery time, the modulation of the population inversion is about 6 times smaller and is delayed by almost 90° . From the pulse trains depicted in Fig.1 (a), 1 (c) and 1 (e), we observe that for low DC pumping the train consists of isolated short pulses with a steady state pulse shape. As DC pumping increases, the gain with its inverse saturable absorption behavior increases and consequently the pulses lengthen. The saturable gain counteracts the pulse shaping by the modulator. This becomes even more obvious in the corresponding computed interferometric autocorrelation traces in Fig.1 (b), 1 (d) and 1 (f) shown underneath the intensity profiles. For higher DC pumping levels the IAC traces start to overlap. For the case of neglected SHB, the IAC traces and in fact the computed electric fields do not show any chirp, i.e. nontrivial phase over the pulse. This is in contrast to the experimental results [4]. Experimental results show the same trend in pulse lengthening when varying the DC pumping. However, there is a major difference. The pulses in Fig. 1 are in general longer than the pulses in the experiment. For the case of DC pumping 1.1 times the threshold, the pulse width in Fig. 1 (a) is 7 ps, while it was approximately 3 ps in the

experiment. The experimentally observed spectra are also much more broadband. This indicates that SHB is important and must be incorporated in the model. SHB is strong in Mid-IR QCLs since the strength of diffusion, which combats the carrier density modulation, scales with the square of the wave number k [2]. One can show that the strength of the carrier density modulation or gain grating is proportional to $1/(1+4k^2D T_1)$ [2], where D is the diffusion coefficient. In regular ($T_1=5$ ps) Mid-IR QCLs, $4k^2D$ is roughly the same as $1/T_1$ and SHB is strong. Even for the long upper state lifetime $T_1=50$ ps of the “superdiagonal” QCL structure, the effects of SHB cannot be neglected. Fig. 2 shows the intensity profiles and corresponding IAC traces for the same parameters as used for Fig. 1, but including SHB. For higher pump levels the pulses no longer reach a steady state and even for low pumping the pulse shape is strongly modulated. The pulse spectra (not shown) and the IAC traces become much closer to the measured IAC traces in actual devices [4]. The main peaks of the pulses do get shorter, 2 ps for the case in Fig. 2 (a). For higher levels of DC pumping, the pulses become more structured [Fig 2 (c) and 2 (e)], *i.e.*, there is nonlinear phase on the pulse, as is evident in the corresponding IAC traces. For both cases, including and not including SHB, if the DC pumping is kept constant and the amplitude of the AC modulation is increased, the pulse quality improves.

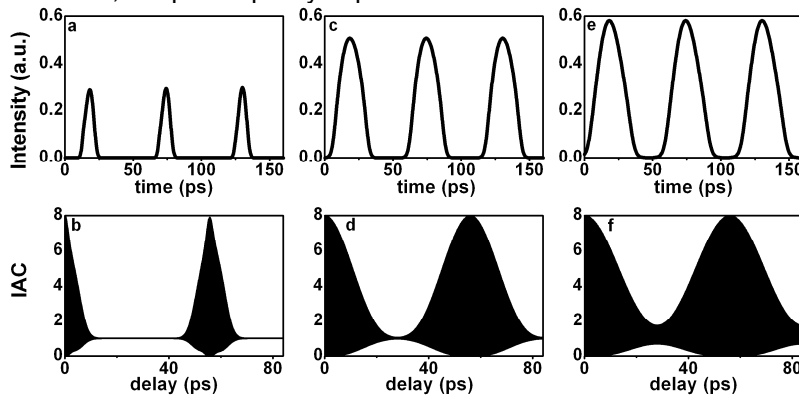


Figure 1. Top row, intensity profile and bottom row corresponding interferometric autocorrelation (IAC) of output pulse train for modulation with AC amplitude 5 times the threshold for different DC pumping levels without including SHB. a), b) for DC pumping 1.1 times the threshold; c), d) for DC pumping 1.45 times the threshold; e), f) for DC pumping 1.61 times the threshold.

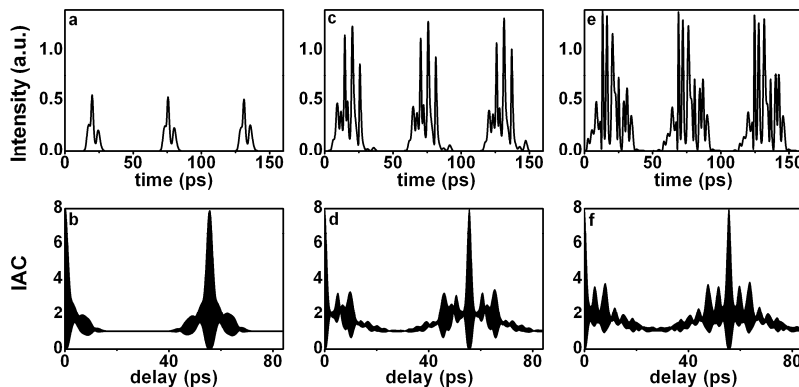


Figure 2. Top row, intensity profile and bottom row corresponding interferometric autocorrelation (IAC) of output pulse train for modulation with AC amplitude 5 times the threshold for different DC pumping levels including SHB. a), b) for DC pumping 1.1 times the threshold; c), d) for DC pumping 1.45 times the threshold; e), f) for DC pumping 1.61 times the threshold.

References

- [1] R. Paiella, *et al.* Appl. Phys. Lett. **77**, 169 (2000).
- [2] A. Gordon, *et al.* Phys. Rev. A **77**, 53804 (2008).
- [3] J. Faist, *et al.* Nature **387**, 777 (1997).
- [4] C. Wang *et al.*, CLEO CPDA11 (2008).

Ultrafast Nonlinearities in Proton-bombarded InGaAs/GaAs Saturable Bragg Reflectors

Sponsors: AFOSR Contract FA9550-07-1-0014, DARPA Contract HR0011-05-C-0155, DARPA Contract W911NF-04-1-0431

Project Staff:

Ali Motamedi, Gale S. Petrich, Professor Leslie A. Kolodziejcki, Professor Erich P. Ippen

Saturable Bragg reflectors (SBR) are critical elements for high repetition rate passively mode locked lasers. The carrier dynamics of an SBR consist of several fast and slow recovery times. The fast time constants are due to the intraband carrier dynamics and are typically in the order of 100fs – 1ps. The slow recovery times are on the order of several picoseconds to several nanoseconds and are functions of the interband relaxation and carrier recombination. The slower recovery times of an SBR can limit the repetition rate and pulsewidth that can be achieved in a mode locked laser. They can also play a helpful role in initiating modelocked pulse formation. To obtain high repetition rates and femtosecond pulses, SBRs with an optimum sequence of recovery times must be designed and fabricated.

Reduction of the carrier lifetime in an SBR can be achieved by introduction of defect states. The reduction of carrier lifetime of SBRs has been observed in the past [1]. In this research project, we study in more detail the effects of the proton bombardment on the characteristics of InGaAs/GaAs SBRs as a function of the bombardment density and optical intensity. By correlating the results of these pump-probe measurements with the operating characteristics of experimental lasers using these SBRs we will achieve an improved understanding of what is needed for optimal performance under different conditions.

The InGaAs multiple quantum well devices shown in Fig. 1 were fabricated in Professor Kolodziejcki's group for use in the 1550nm range. The structure consists of a 60 nm InGaAs absorber embedded in a half-wave cladding layer. The bragg reflector is made up of 22 pairs of GaAs/Al_{0.95}Ga_{0.05}As mirror centered at 1550nm. The devices were bombarded with 40KeV protons with density of 10¹³, 10¹⁴, and 10¹⁵ per cm².

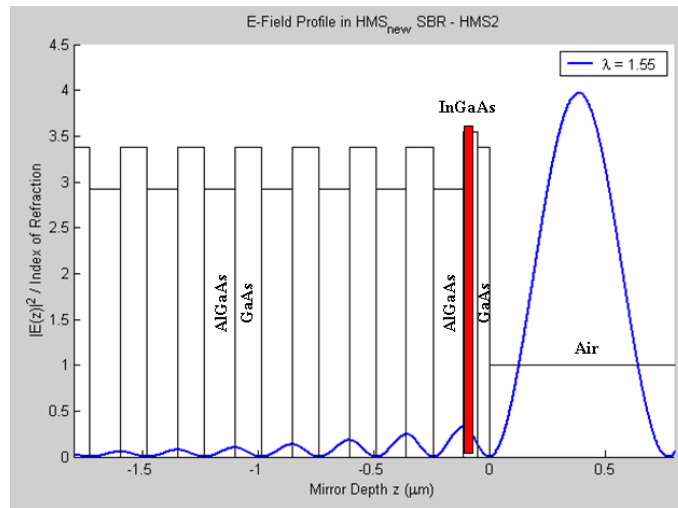


Fig. 1. InGaAs saturable absorber for 1550nm wavelength range

A degenerate cross-polarized pump probe experiment as shown in Fig. 2 is being utilized to study the effects of different proton bombardment levels on the saturation fluence and carrier recovery of times of this device. The experimental setup is comprised of an optical parametric oscillator (OPO) tunable between 1400-1600nm with a repetition rate of 80MHz and 150fs pulses. The light

from the OPO is split into two paths using a 30:70 beamsplitter with the higher power beam being used for the pump and the other for the probe signals. A delay stage is used to change the relative timing of the incident pump and probe signals. The reflected beam from the sample is then filtered using a polarizer that only passes the probe beam which is detected using a photodetector. The amplitude and phase of the photodetector signal are detected using a lock-in amplifier.

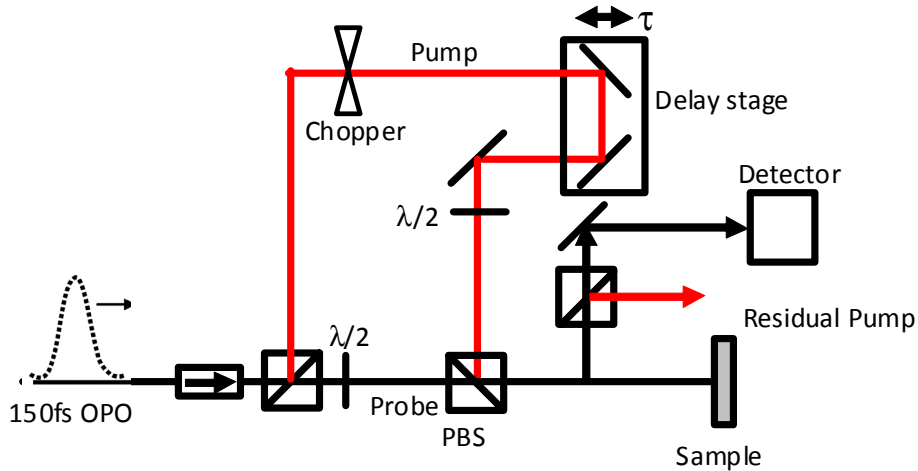


Fig. 2. Schematic of a degenerate cross-polarized pump-probe experimental setup

The results of the pump-probe experiments at a center wavelength of 1560nm are shown in Fig. 3. The long recovery time is reduced from 80 ps with no proton bombardment to 12 ps. The modulation depths of the samples vary from 2.8% with no and $10^{13}/\text{cm}^2$ proton bombardment to 1.8% with $10^{15}/\text{cm}^2$ proton bombardment.

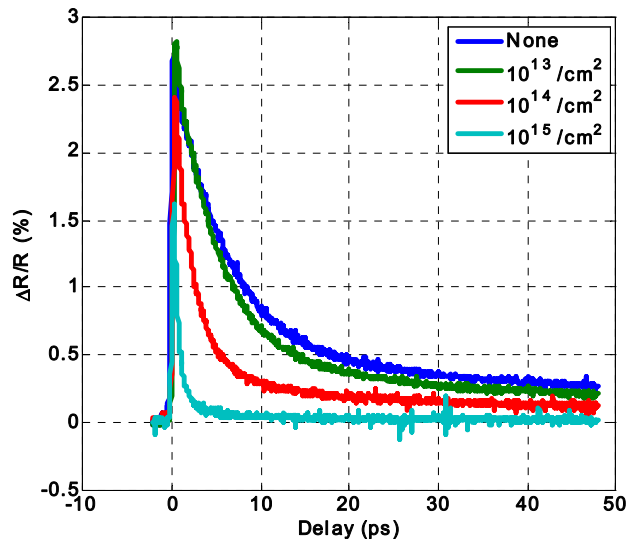


Fig. 3. Carrier recovery times as a function of proton bombardment

With a sequence of such studies made with different incident pulse powers, one achieves a measure of ultrashort pulse reflectivity from the SBRs as a function of fluence. Measured reflectivity curves for the above devices are plotted in Fig. 4. To fit these curves, we model the

absorption of an SBR by the sum of non-saturable loss, saturable loss, and two-photon absorption (TPA) as described by the following equation:

$$R = 1 - \alpha_{ns} - \frac{\alpha_0}{1 + \frac{F}{F_{sat}}} - \frac{\beta AL}{3\tau} F,$$

where α_{ns} is the non-saturable loss, α_0 is the saturable loss, F is the fluence, F_{sat} is the saturation fluence, β is the two-photon absorption (TPA) coefficient, L is the effective interaction length, τ is the pulsewidth, and A is the area of the pump beam on the sample.

The third term in the above equation is the saturable loss of the device as a function of the fluence, and the last term is the TPA loss which is the dominant term at higher fluencies and results in the roll off of the saturation fluence curves. Using this model, the saturation fluence of different samples are determined to be 30, 25, 20, and 20 $\mu\text{J}/\text{cm}^2$ for 10^{15} , 10^{14} , 10^{13} , and 0 proton bombarded samples, respectively.

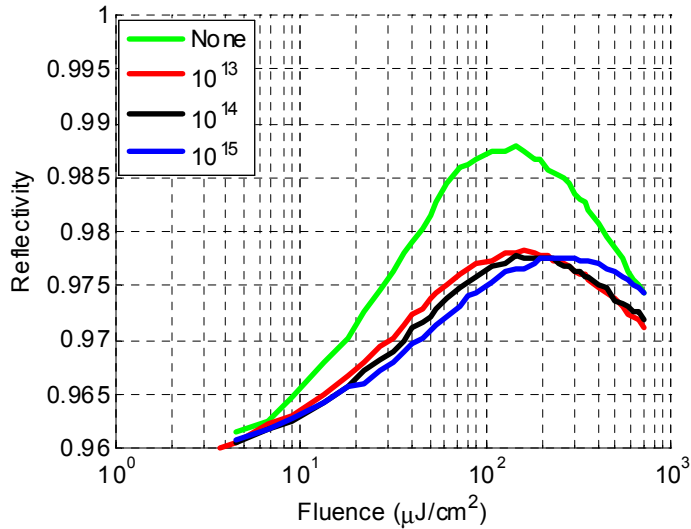


Fig. 4. Saturation fluence curves of the SBR as a function of the proton bombardment

Models to predict the saturation fluence and recovery time of the devices as a function of the proton bombardment are being developed.

References

- [1] J.T. Gopinath, et.al, App. Phys. Lett., 78, 2001.
- [2] M. Le Du, et.al, App. Phys. Lett., 88, 2006

Attosecond Science

Broadband Optical Parametric Chirped Pulse Amplification

Sponsors

Air Force Office of Scientific Research ("DARPA HRS") FA9550-06-1-0468

MIT Lincoln Laboratory 7000013535

Rocca Foundation

Project Staff

Dr. Jeffrey Moses, Dr. Kyung-Han Hong, Dr. Edilson L. Falcão-Filho, , Shu-Wei Huang, Giovanni Cirmi, A. Benedick, J. R. Birge, Cristian Manzoni, Prof. Giulio Cerullo, and Prof. Franz X. Kärtner

Since the prediction of high-yield soft X-ray photon generation through high harmonic generation (HHG) with long-wavelength drive pulses [1, 2, 3], the development of high-power, few-cycle, carrier-envelope phase- (CEP-) stabilized sources in the mid-IR has attracted great attention. Ultra-broadband optical parametric chirped pulse amplification (OPCPA) is one of the promising techniques to meet the requirement for the driving source.

In particular, our group has been developing few-cycle OPCPA at 2 μm that will eventually be used as the driving source for high harmonic generation experiments [4]. The goal is to optimize the photon yield at 500-eV for high resolution water-window X-ray microscopy. Figure 1 shows the schematic of the 2 μm OPCPA. An octave-spanning Ti:Sapphire oscillator generates passively CEP-stabilized broadband 2 μm seed pulses by intrapulse difference frequency generation (DFG) in a MgO-doped periodically-poled lithium niobate (MgO:PPLN) crystal. Once the remaining 1 μm Ti:Sapphire light is sent to the pump amplifier chain, the 2 μm seed pulses are stretched in 30 mm of bulk silicon to 6.2 ps length (full width at -10 dB) and then preamplified in an optical parameter amplifier (OPA), OPA1 (3 mm MgO:PPCLN, L=31.0 μm), to 1.5 μJ . After OPA1, an acousto-optic programmable dispersive filter (AOPDF, Fastlite) increases the signal duration to 9.5 ps, both optimizing efficiency-bandwidth product and superfluorescence (SF) suppression in the power amplifier stage [5] and compensating for higher-order dispersion mismatch between the stretcher and compressor materials. Losses from the AOPDF (~90%) and spatial filters are compensated by OPA2. The resulting 5 μJ pulse is amplified to 250 μJ in OPA3 and compressed in three passes through an antireflection-coated 10 cm, high-purity quartz glass block that introduces ~10% loss. The OPA2 and OPA3 crystals are, respectively, 3-mm- and 1.6-mm-length stoichiometric lithium tantalate (MgO:PPSLT) gratings with L=31.4 μm . In all stages, a 1° angle between pump and signal beams allows separation of signal and idler after amplification.

The pump laser system is a Nd:YLF chirped pulse amplifier with chirped fiber Bragg grating (CFBG) as the stretcher and Treacy grating pairs as the compressor. To seed the regenerative amplifier properly, two Yb-doped fiber amplifiers (YDFA) is used. The regenerative amplifier (High-Q Laser) gives a 1 kHz, 1 mJ pulse train with 0.25 nm bandwidth, which then is amplified further to 7 mJ by two three-pass MPS amplifiers (Q-Peak MPS gain modules). After the Treacy grating pair compressor, a 1 kHz, 4.5 mJ, 11 ps pulse train is available for pumping the OPCPA.

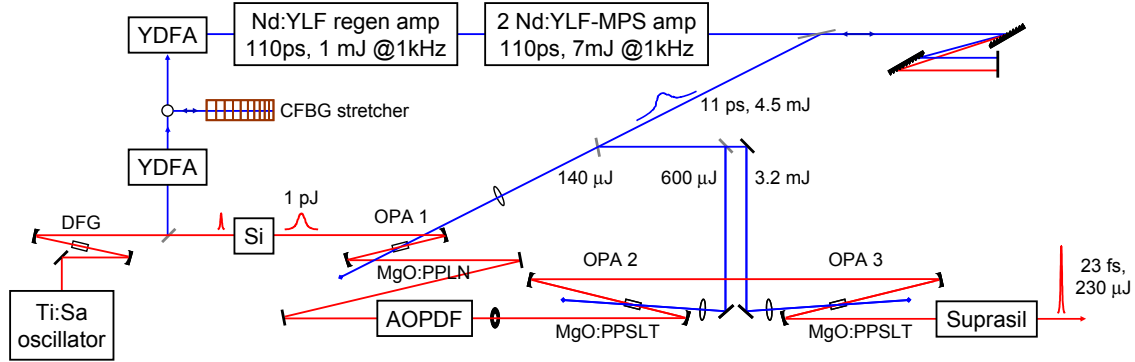


Figure 1: Schematic of the 2 μm OPCPA system.

The main difference between our work and the pioneering work by T. Fuji *et al.* and X. Gu *et al.* [6, 7] is we manage to suppress the superfluorescence by several methods. First, the stretcher/compressor scheme maximizes the 2 μm seed energy by avoiding lossy elements in the pulse stretcher. Second, we use multiple apertures after OPA1 to eliminate the phase-matched, SF-dominated high order spatial modes of the signal. In addition to a hard aperture after OPA1, by setting the pump beam width less than half the signal beam width in OPA2 and OPA3 and placing the nonlinear crystal 2–3 diffraction lengths away from the signal focus, the amplifiers act as soft apertures and spatial filters. The apertures clean the signal beam by sequentially selecting a smaller portion of the initial seed beam. This cleans the wavefront, eliminates the spatial chirp, preserves only the region of the beam with highest SNR, and impresses the clean pump beam profile on the amplified signal. Third, we carefully design the signal chirp at each stage. As discussed in [5], there is a trade-off between conversion efficiency and bandwidth/SNR as the signal chirp varies and the optimal chirp is dependent on the desired gain of the OPA stage. We use the AOPDF to introduce the additional chirp necessary between OPA1 and OPA2/3. The signal is chirped to 6.2 and 9.5 ps for OPA1 (10^6 gain) and OPA2/3 (10^2 – 10^3 gain), respectively.

Figure 2 shows the amplified spectrum (a) and the corresponding interferometric autocorrelation trace (b) of the OPCPA system. The pulse is compressed nearly to its transform limit, i.e., 23 fs, or 3 cycles in FWHM. The CEP stability is characterized using an f -to- $3f$ spectral interferometer and Fig. 1(c) shows that the rms phase fluctuation is ~ 150 mrad over 10 s, where the residual phase excursion at time = ~ 2 s is attributed to the amplitude-phase noise coupling in the f -to- $3f$ interferometer while any significant drift is not observed during 10 s.

The SF level is estimated by measuring the energy fluctuation and the intensity fluctuation, followed by statistical analysis and is about 8%. With slightly less saturation in the power amplification stage, 170 μJ signal energy with SF reduced to 2% is obtained.

In conclusion, we have demonstrated a 10-GW, 3-optical-cycle (230 μJ , 23 fs), phase-stabilized 2.2- μm OPCPA system with suppressed superfluorescence. Our current results suggest that scaling should be possible to the multi-mJ level, which will allow absorption-limited HHG.

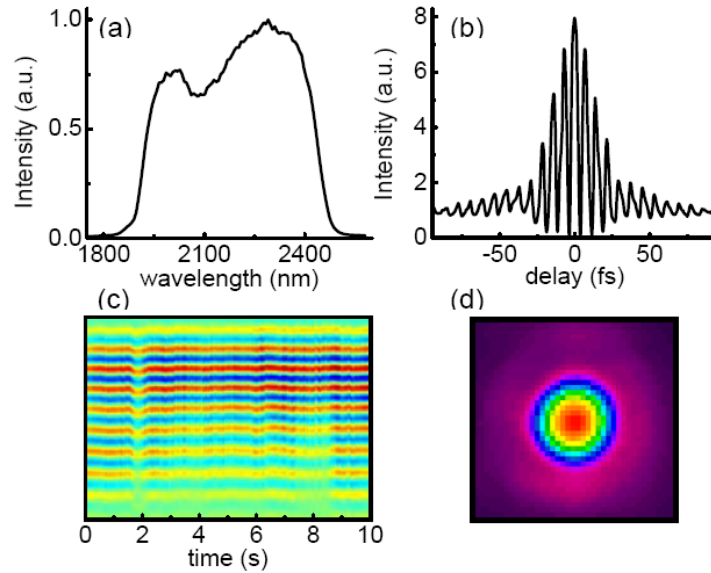


Figure 2: (a) Amplified spectrum, measuring 500-nm FWHM in bandwidth. (b) IAC of the compressed pulse, measuring 23 fs (3 cycles). (c) f - $3f$ spectral interferogram, measuring 150 mrad rms in CEP fluctuation. (d) Pyroelectric CCD image of the output beam.

References

- [1] B. Shan and Z. H. Chang, *Phys. Rev. A*, **65**, 011804 (2002).
- [2] A. Gordon and F. X. Kärtner, *Opt. Express*, **13**, 2941 (2005).
- [3] E. L. Falcão-Filho, V. M. Gkortsas, Ariel Gordon and Franz X. Kärtner, *Opt. Express*, **17**, 11217 (2009).
- [4] J. Moses, S.-W. Huang, K.-H. Hong, O. D. Mücke, E. L. Falcão-Filho, A. Benedick, F. Ö. Ilday, A. Dergachev, J. A. Bolger, B. J. Eggleton, and F. X. Kärtner, *Opt. Lett.*, **34**, 1639 (2009).
- [5] J. Moses, C. Manzoni, S.-W. Huang, G. Cerullo, and F. X. Kärtner, *Opt. Express* **17**, 5540 (2009).
- [6] T. Fuji, N. Ishii, C. Y. Teisset, X. Gu, T. Metzger, A. Baltuška, N. Forget, D. Kaplan, A. Galvanauskas, and F. Krausz, *Opt. Lett.* **31**, 1103 (2006).
- [7] X. Gu, G. Marcus, Y. Deng, T. Metzger, C. Teisset, N. Ishii, T. Fuji, A. Baltuška, R. Butkus, V. Pervak, H. Ishizuki, T. Taira, T. Kobayashi, R. Kienberger, and F. Krausz, *Opt. Express* **17**, 62 (2009).

Temporal Optimization of Ultrabroadband Optical Parametric Chirped Pulse Amplification

Sponsors

Air Force Office of Scientific Research (AFOSR), FA9550-06-1-0468

Air Force Office of Scientific Research (AFOSR), FA9550-07-1-0014

Progetto Rocca

Project Staff

Dr. Jeffrey Moses, Dr. Cristian Manzoni, Shu-Wei Huang, Dr. Giulio Cerullo and Professor Franz X. Kärtner

Today's demands on light sources for high-intensity ultrafast optics research are stringent: peak power must be maximized by scaling both to high energy and near-single-cycle duration, signal to noise contrast must be high, and often pulses at nontraditional wavelengths must be generated. These requirements have led to the rapid development of ultrabroadband optical parametric chirped pulse amplification (OPCPA) pumped by powerful picosecond pulses, in which gain bandwidth is stretched to near-octave breadths by group-velocity matching between signal and idler. In recent years, several problems in the construction of these amplifiers have become relevant. The coupling of temporal gain narrowing and spectral narrowing results in a trade-off between conversion efficiency and bandwidth. Additionally, the amplifier seed energy is often low while total gain is high, resulting in high levels of parametric superfluorescence and poor signal-to-noise ratio [1, 2]. While the effect of temporal gain narrowing on ultrabroadband OPCPA has been investigated [3], a study of simultaneous optimization of conversion efficiency, signal bandwidth and signal-to-superfluorescence ratio has not yet been presented, and several details of the temporal optimization problem have been neglected.

We have employed analytical and numerical analyses, supported by experiment, to investigate the simultaneous optimization of conversion efficiency, signal bandwidth, and signal-to-noise ratio in ultrabroadband, high-energy OPCPA [4]. We find that each of these properties is strongly tied to the ratio of seed and pump pulse durations, and that due to dependence of the optimization problem on the peak amplifier gain, the seed pulse chirp must be optimized independently in each stage of a multi-stage OPCPA system. Additionally, we find that a small reduction in signal bandwidth strongly enhances the signal-to-noise ratio and conversion efficiency. These principles have since been used to build a high-energy, 3-cycle, 2- μm amplifier with low noise and good energy stability [5].

Figure 1 illustrates the basic principle of the analysis, *i.e.*, the simultaneous dependence of conversion efficiency, amplifier bandwidth, and signal-to-noise ratio in OPCPA on the seed chirp. The panels on the left plot the signal gain profile, $G = 1 + (\Gamma/\gamma)^2 \sinh^2(\gamma L)$, for a chirped seed pulse overlapped with a Gaussian pump pulse with intensity $I_p(t)$, alongside the corresponding noise gain profile; here $\gamma^2 = \Gamma^2(\Delta k/2)^2$, Γ is the nonlinear drive (proportional to the square-root of I_p), and Δk is the wave-vector mismatch. Since noise photons produced by spontaneous parametric generation will be statistically equally distributed in time and frequency, the instantaneous noise gain is determined solely by the local pump intensity, $I_p(t)$, while the instantaneous signal gain is further reduced by the local wave-vector mismatch $\Delta k(t)$. With $\Delta t_s = \Delta t_p/3$ (small seed chirp, Fig. 1a) the signal pulse fits within a largely unvarying portion of the pump intensity profile. As a result, there is little clipping of the signal pulse at the wings, and the effective amplifier bandwidth is nearly the full phase-matching bandwidth (Fig. 1c). However, since the signal carrier frequency sweeps quickly in time, so does $\Delta k(t)$, and as a result the gain profile of the signal is much narrower than that of the noise. The narrow signal gain profile means the conversion efficiency will be small, as only a fraction of the pump pulse will be depleted, and the large area between signal and noise gain profiles means the signal-to-noise ratio will strongly degrade after amplification. At $\Delta t_s = \Delta t_p$ (large seed chirp, Fig. 1b), the slower variation in $\Delta k(t)$ allows the signal gain profile to widen relative to the noise gain profile, resulting in larger conversion efficiency and higher signal-to-noise ratio. On the other hand, since there is more spectral clipping of the signal

pulse during amplification, there is a narrower effective amplifier bandwidth. This bandwidth reduction strongly improves the robustness of signal-to-noise ratio of the amplifier; in fact, since the effective amplifier bandwidth covers only the flat, phase-matched central region of the gain bandwidth, Δk is essentially zero over the full significant gain region of the pump pulse. Therefore, there is little preferential amplification of the noise.

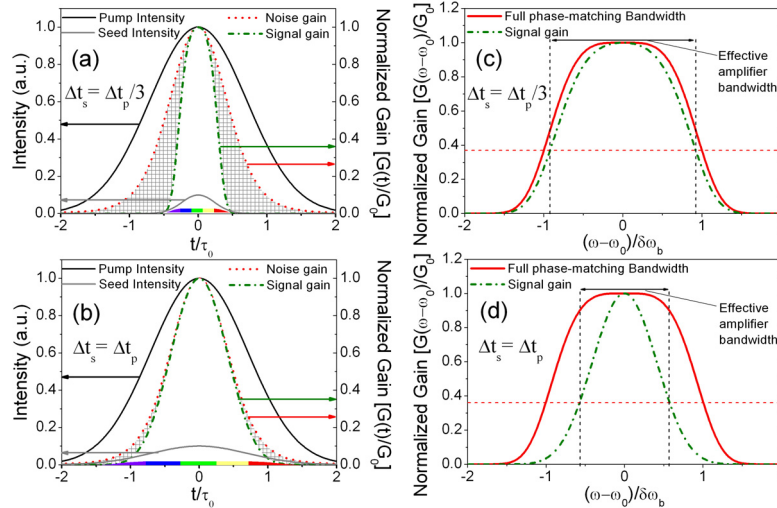


Figure 1: (a,b) Gaussian pump (black, solid) and seed (gray, solid) intensity profiles with corresponding signal gain (green, dot-dashed) and noise gain (red, dotted) profiles for different ratios of seed and pump pulse durations ($\Delta t_s, \Delta t_p$). The shaded region represents the difference between noise and signal gain. The chirp of the signal pulse is represented by colored bars. (c,d) Corresponding signal gain profiles (green, dot-dashed) in the frequency domain, plotted alongside the full phase-matching bandwidth of the amplifier (red, solid).

These predictions have been verified by means of numerical simulations solving the coupled nonlinear equations in a 3-mm long periodically poled stoichiometric lithium tantalate crystal pumped by a 9-ps pulse. Several important results are summarized in Fig. 2. The trade-off between conversion efficiency and amplifier bandwidth results in a maximum efficiency-bandwidth product, a quantity shown for three values of the amplifier peak gain, plotted as a function of seed chirp. In addition, the simulations verify the predicted reduction in superfluorescence noise (relative to signal energy) as the seed chirp is increased. We observe a strong reduction in noise level until roughly the same chirp that maximizes efficiency-bandwidth product is reached; from that point on the signal-to-noise ratio flattens out. Thus, amplifier peak power and signal-to-noise ratio can be optimized simultaneously.

Our results further suggest a need for stage-by-stage optimization of the signal chirp. The chirp that maximizes efficiency-bandwidth product and insures robustness of signal-to-noise ratio decreases with increasing gain, due to the increase in gain narrowing. We have found our simulation results to be fit well by an analytic formula for temporal signal gain profile width, $(\Delta t_s / \Delta t_p)_{\text{OPT}} \approx \alpha (-2 \ln[1 - 1/\ln(4G_0)])^{1/2}$, where G_0 is the peak signal gain. According to this result, a power amplifier stage with peak gain $G_0 = 10^2$ will have 1.5 times larger optimal chirp than a preamplifier stage with $G_0 = 10^5$. In order to prevent stage-to-stage buildup of superfluorescence noise while maintaining an ultrabroad bandwidth, the seed chirp should be readjusted at each amplification stage.

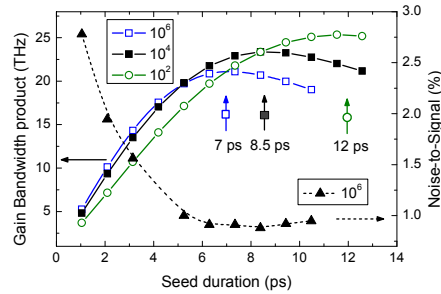


Figure 2: (a) Simulation results for conversion efficiency (signal + idler) for several values of seed pulse duration and $G = 10^4$. The squares denote where maximum pump depletion occurs. (b) Efficiency-bandwidth product (at maximum possible conversion efficiency) versus seed pulse duration for $G = 10^2$, 10^4 , and 10^6 . Triangles denote noise-to-signal ratio for $G = 10^6$.

References

- [1] F. Tavella, A. Marcinkevicius, and F. Krausz, "Investigation of the superfluorescence and signal amplification in an ultrabroadband multiterawatt optical parametric chirped pulse amplifier system," *New J. of Phys.* 8: 219 (2006).
- [2] T. Fuji, N. Ishii, C. Y. Teisset, X. Gu, T. Metzger, A. Baltuška, N. Forget, D. Kaplan, A. Galvanauskas, and F. Krausz, "Parametric amplification of few-cycle carrier-envelope phase-stable pulses at 2.1 μm ," *Opt. Lett.* 31(8): 1103-1105 (2006).
- [3] S. Witte, R. T. Zinkstok, W. Hogervorst, and K. S. E. Eikema, "Numerical simulations for performance optimization of a few-cycle terawatt NOPCPA system," *Appl. Phys. B* 87(4): 677-684 (2007).
- [4] J. Moses, C. Manzoni, S.-W. Huang, G. Cerullo, and F. X. Kärtner, "Temporal optimization of ultrabroadband high-energy OPCPA," *Opt. Express* 17(7): 5540-5555 (2009).
- [5] J. Moses, S.-W. Huang, K.-H. Hong, O. D. Mücke, E. L. Falcão-Filho, A. Benedick, F. Ö. Ilday, A. Dergachev, J. A. Bolger, B. J. Eggleton, and F. X. Kärtner, "Highly stable ultrabroadband mid-IR optical parametric chirped-pulse amplifier optimized for superfluorescence suppression," *Opt. Lett.* 34(11): 1639-1641 (2009).

High-average-power picosecond green laser based on a frequency-doubled hybrid cryogenic Yb:YAG amplifier

Sponsors

Air Force Office of Scientific Research (“DARPA HRS”) FA9550-06-1-0468
and FA9550-07-1-0014

Project Staff

Dr. Kyung-Han Hong, Chien-Jen Lai, and Prof. Franz X. Kärtner

1. Introduction

High-average-power pulsed green lasers have been widely used for both scientific and industrial applications, such as pumping near-IR ultrashort high-power lasers, laser machining, and laser material processing. Intra-cavity frequency-doubled Q-switched nanosecond Nd-doped lasers have been one of the most popular green lasers and average power levels of >300 W have been demonstrated with this technology [1]. However, this type of green lasers are in general not ideal sources for some advanced applications, such as precise micro-machining or material processing and pumping of optical parametric chirped-pulse amplifiers (OPCPAs), because of the multi-mode beam profile with large M^2 values (>10) [2] and relatively long pulse durations. The M^2 values can be significantly decreased by using external-cavity second harmonic generation (SHG) of a high-quality high-power 1- μm laser source. Recently, a high-beam-quality nanosecond green laser with an average power of 103 W was demonstrated from an external-cavity frequency-doubled Nd:YVO₄ master oscillator-power amplifier (MOPA) system [3].

High-power high-beam-quality (low- M^2) picosecond green lasers are suitable not only for the thermal-effect-free material processing, where thermal effects are minimized at <15 ps duration, but also for pumping near-IR OPCPAs usually seeded by 800-nm ultrabroadband Ti:sapphire lasers. Picosecond laser pulses also have a great advantage over femtosecond laser pulses in efficient nonlinear frequency conversion because of the narrow spectral bandwidth and negligible group-velocity mismatch (GVM). Thus, picosecond green and ultraviolet light can be efficiently generated from picosecond IR beams for the applications mentioned above. Dupriez *et al.* [4] demonstrated 80 W of average power using SHG of 20-ps 1060-nm pulses from a fiber MOPA system. More recently, >20 W of average power was obtained from a frequency-doubled picosecond Nd:YVO₄ and Nd:YAG MOPA system [5]. All the results in Refs. [3-5] showed excellent beam quality with M^2 values ranging from 1.2 to 2.5. Therefore, frequency-doubled picosecond IR MOPA systems can provide high-beam-quality high-average-power picosecond green pulses at the expense of a slightly more complex laser system.

In this report, we demonstrate a frequency-doubled picosecond hybrid cryogenic Yb:YAG laser generating 130 W average power which is the highest average power for a picosecond green laser to date. A SHG efficiency of 54% was achieved with a 240-W 8-ps IR pulse train in a noncritically phase matched LBO crystal. A measured mean M^2 value of 2.7 reveals a good focusing quality of the beam.

2. Picosecond hybrid cryogenic Yb:YAG laser system

In previous work [6], we have developed a picosecond hybrid cryogenic Yb:YAG laser system seeded by a fiber chirped-pulse amplification (CPA) chain for the generation of high-average-power <10-ps pulses at 1029 nm with a repetition rate of 78 MHz. Figure 1 illustrates the schematic of the laser system. The fiber CPA chain based on chirped volume Bragg gratings (CVBGs) provides 6 W of power to a double-pass Yb:YAG amplifier, cooled by liquid nitrogen and pumped by a total of 700 W of power from two fiber-coupled laser diodes at 940 nm. The maximum average power from this laser of 287 W was obtained with a pulse duration of 5.5 ps over a spectral bandwidth of 0.3 nm. It should be noted that the spatial chirp induced by the CVBGs limited the beam quality of this laser ($M^2 \sim 2.75$ and 1.15 for x- and y-axes, respectively).

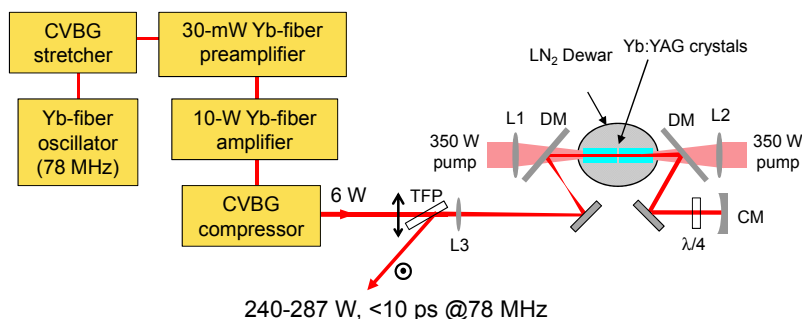


Fig. 1: High-average-power hybrid cryogenic Yb:YAG laser system seeded by a fiber CPA chain based on CVBG stretcher and compressor. CVBG, chirped volume Bragg grating; DM, dichroic mirror; CM, curved mirror; L1-L3, lenses; $\lambda/4$, quarter waveplate; TFP, thin film polarizer; LN₂, liquid nitrogen.

In recent experiments, we used different CVBGs to reduce the spatial chirp and improve the focusing quality. The efficiency of the stretcher and compressor was enhanced from 55% to 66% (7 W of power), but the spatial chirp and focusing quality of the laser pulses for the experiments discussed here are similar to those in Ref. [6] and the pulse duration lengthened to 8.0 ps. The maximum output power was limited to 240 W in the SHG experiment because of a power drop in one pump diode module. Additionally, we observed astigmatism at the maximum power of the fiber CPA chain, induced by the thermal lensing in the new compressor. The astigmatism could be removed by cooling the CVBG or by compensation with a lens, which was not attempted here. Nevertheless, overall performance of this laser source is still good enough for the generation of high-average-power green picosecond pulses with a good beam quality via SHG.

3. Experimental result and discussion

The use of LBO for SHG with high average and peak powers has the following advantages: high damage threshold, relatively high d_{eff} (0.85 pm/V), no spatial walk-off and large acceptance angle for the case of type-I noncritical phase matching condition ($\theta=90^\circ$ and $\phi=0^\circ$) at 1 μm wavelength. For 1029 nm wavelength and 195.5 $^\circ\text{C}$ crystal temperature, the acceptance angle is as large as 340 mrad $\cdot\text{cm}$ while it is only 7.8 mrad $\cdot\text{cm}$ for type-I critical phase matching at room temperature ($\theta=90^\circ$, $\phi=13.6^\circ$). In the experiment, we utilized a 15-mm-long LBO crystal mounted in a temperature-controlled oven (EKSPILA, Inc.). The calculated spectral phase matching bandwidth of this crystal is 2.0 nm in full width at half-maximum (FWHM) and 0.8 nm in full width at 90% of peak, which is broad enough to support the spectral bandwidth (<0.5 nm) of our laser source. The temperature-dependent phase matching curve is centered at 195.5 $^\circ\text{C}$ and has a bandwidth of 2.8 $^\circ\text{C}$ in FWHM, which showed a good agreement with the experimental measurement ($\sim 2.6^\circ\text{C}$) at low powers (<3.6 W of SH power). In the experiment, the phase matching was peaked at $\sim 189.1^\circ\text{C}$ rather than at 195.5 $^\circ\text{C}$, but this discrepancy can be explained by a simple calibration error arising from the difference between the internal temperature of the LBO crystal and the temperature of the crystal mount where the temperature is monitored. Our three-dimensional simulations, based on the parameters of the IR beam, indicate that a theoretical maximum SHG efficiency of >85% can be reached at a peak power of $\sim 3\text{ GW}/\text{cm}^2$ for the maximum IR power, assuming a Gaussian beam profile, perfect phase matching and negligible GVM. The actual GVM is as low as 50 fs/mm and the temporal walk-off of 0.75 ps for 15 mm is only $\sim 10\%$ of the IR pulse duration (8 ps). Therefore, the GVM will only slightly decrease the SHG conversion efficiency in the experiment. A non-ideal beam profile at each position along the propagation direction and a temperature gradient [3] produced by the high-average-power beam inside the LBO crystal are expected to further reduce the conversion efficiency in the experiment.

Figure 2(a) shows the SHG setup following the picosecond hybrid cryogenic Yb:YAG laser. We focused the 8-ps 1029-nm pulses into the LBO crystal using an $f=100\text{ mm}$ lens to achieve a peak intensity of 2.9 GW/cm^2 for the case of 240 W (IR) average power. The beam waist at focus was 65 μm averaged in horizontal and vertical directions. The output power of the green light was measured after two dichroic mirrors that completely remove the IR component. While monitoring the SH power, we carefully optimized the crystal position along the beam focusing direction and the oven temperature. It was found that the SHG efficiency was higher when the LBO center was placed slightly after the focus rather than at the focus.

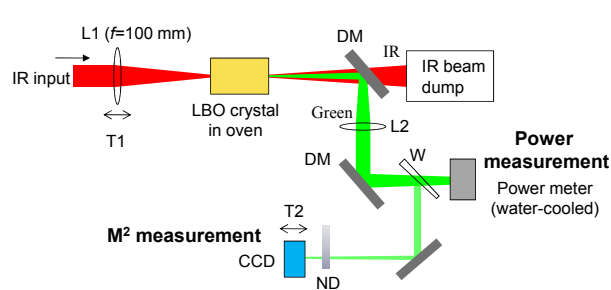
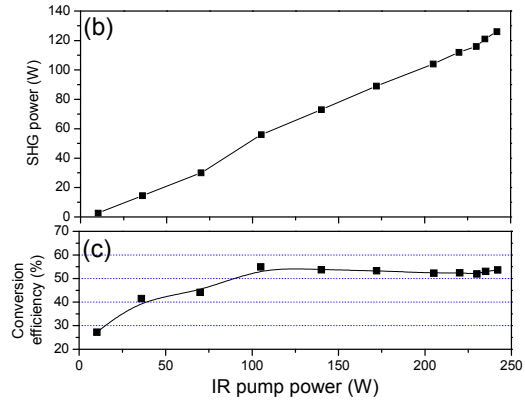


Fig. 2: Experimental setup (a), average power (b), and conversion efficiency (c) of SHG from the cryogenic hybrid Yb:YAG laser using a 15-mm-long LBO crystal. L1-L2, lenses; DM, dichroic mirror; W, wedge; T1-T2, translators.



The output power of green pulses and the conversion efficiency versus the IR input power are shown in Figs. 2(b) and (c), respectively. The LBO oven temperature was adjusted to maximize the SH power at each IR power level to compensate for the internal heating of LBO crystal by the high-power IR and green beams. The conversion efficiency of 55% ($\pm 1\%$) was almost constant in the range from 100 to 240 W of IR power due to the significant pump depletion in this power range. We obtained a maximum green output power as high as 130 W with 240 W of the IR input power. Since the conversion efficiency continuously increased from 33% to 54% at the maximum IR power as the focal length of L1 decreases from 200 mm to 100 mm, further efficiency enhancement may be possible by decreasing the focal length, which was limited by the small numerical aperture of the LBO crystal and mount. The pulse duration of the green light, which was not directly measured, was estimated to be 6.4 ps using the IR pulse duration and the GVM value, i.e., the sum of the frequency-doubled pulse duration and GVM ($8/1.414$ ps + 0.75 ps). The spectral bandwidth of the green light was measured as 0.2 nm at 514.5 nm which supports a transform-limited pulse duration of 1.9 ps.

The M^2 values in horizontal and vertical directions at 77 W of SH power were measured to be 3.6 and 1.8, respectively. The larger value for the horizontal axis still stems from the spatial chirp induced by the CVBG compressor. These values were worse than those of the IR beam, but the mean value of 2.7 still indicates a good focusing quality of the SH beam sufficient for many applications. The beam quality of both the SH-beam and IR-beam can be significantly improved to almost diffraction limited performance by using a spatial-chirp-free CVBG compressor [7] or by substitution of the CVBG compressor by a diffraction-grating compressor.

References

- [1] J. J. Chang *et al.*, "315-W pulsed-green generation with a diode-pumped Nd:YAG laser," *CLEO 1998 Tech. Digests* (OSA, Washington, D.C., 1998) CPD2.
- [2] S. Konno *et al.*, "High-brightness 138-W green laser based on an intracavity-frequency-doubled diode-side-pumped Q-switched Nd:YAG laser," *Opt. Lett.* 25, 105-107 (2000).
- [3] Q. Liu *et al.*, "103 W high beam quality green laser with an extra-cavity second harmonic generation," *Opt. Express* 16, 14335-14340 (2008).
- [4] P. Dupriez *et al.*, "80 W green laser based on a frequency-doubled picosecond, single-mode, linearly-polarized fiber laser," *CLEO 2006 Tech. Digests* (OSA, Washington, D.C., 2006) CThJ1.
- [5] R. Peng *et al.*, "43 W picosecond laser and second-harmonic generation," *Opt. Commun.* 282, 611-613 (2009).
- [6] K.-H. Hong *et al.*, "Generation of 287 W, 5.5 ps pulses at 78 MHz repetition rate from a cryogenically cooled Yb:YAG amplifier seeded by a fiber chirped-pulse amplification system," *Opt. Lett.* 33, 2473-2475 (2008).
- [7] M. River *et al.*, "200 fs, 50 W fiber-CPA system based on chirped-volume-Bragg-gratings," *CLEO 2009 Tech. Digests* (OSA, Washington, D.C., 2009) CMBB2.

Conversion efficiency scaling of high harmonic generation

Sponsors

Air Force Office of Scientific Research (“DARPA HRS”) FA9550-06-1-0468

Project Staff

Dr. Edilson Falcao, Vasileios Gkortsas, Dr. Ariel Gordon and Prof. Franz X. Kärtner

High harmonic generation (HHG) is an exciting field both from the point of view of basic science enabling the study of phenomena on an attosecond time scale but also due to the number of promising applications involving EUV and XUV generation. Comparatively to others XUV sources, HHG is unique due to its complete spatio-temporal coherence.

In our work, applying the saddle point treatment to the dipole acceleration of the improved three step model (ITSM) [1] for HHG, closed analytic formulas for the HHG conversion efficiencies for the plateau and the cutoff region including both laser and material parameters are obtained for the first time. Single-active-electron (SAE) approximation and 1D propagation effects are also included. The final expression for the efficiency at the cutoff frequency, Ω_{cutoff} , can be written as [3]:

$$\eta = 0.0236 \frac{\sqrt{2I_p} \omega_0^5 |a_{rec}|^2 |g(\Delta k, L)|^2}{E_0^{16/3} \Omega_{cutoff}^2 \sigma^2(\Omega_{cutoff})} \frac{1 - \beta^{4(N-1)}}{(1 - \beta^4)N} |1 + \beta|^2 \kappa_0 w[E(tb_{cutoff})] , \quad (1)$$

where $g(\Delta k, L) = [e^{i(\Delta k \cdot L)} - e^{-L/(2 \cdot L_{abs})}] / [1 + 2i(\Delta k \cdot L_{abs})]$ is the phase matching form factor, Δk is the phase mismatch and L_{abs} is the absorption length. N is the number of cycles of the driver pulse and $\beta = |a(\pi/\omega)|^2$ with $|a(t)|^2$ denoting the probability to find the atom in the ground state. I_p is the ionization potential, $w(E)$ is the ionization rate and a_{rec} is the recombination amplitude, as written in Eq. (7) of Ref. [2]. The intra-cycle depletion of the ground state, κ_0 , is given by $|a(tb_{cutoff}) a(ta_{cutoff})|^2$, where the respective birth and arrival times are $tb_{cutoff} \approx 1.88/\omega_0$ and $ta_{cutoff} \approx 5.97/\omega_0$.

In accordance with Eq.(1), the efficiency at the cutoff region scales with a factor of ω_0^5 . A cubic dependence with ω_0 is due to quantum diffusion. An additional factor of ω_0 comes from the fact that we are considering the conversion efficiency into a single harmonic, and the bandwidth it occupies is $2\omega_0$. The fifth ω_0 comes from the energy carried by a cycle of the driving laser field which scales with its duration $2\pi/\omega_0$ for a given electric field amplitude. On the other hand, in the plateau region, each harmonic has contributions from two trajectories and the final expression for the efficiency in the plateau region is [3]

$$\eta = 0.0107 \frac{\sqrt{2I_p} \omega_0^5 |a_{rec}|^2 |g(\Delta k, L)|^2}{E_0^4 \Omega^2 \sigma^2(\Omega)} \frac{1 - \beta^{4(N-1)}}{(1 - \beta^4)N} \left| 1 + \beta e^{i\pi \left(1 - \frac{\Omega}{\omega_0}\right)} \right|^2 \times \left| \frac{a(tb_s) a(ta_s) \sqrt{w(E(tb_s))}}{\sin(\omega_0 tb_s) [\omega_0 (ta_s - tb_s)/(2\pi)]^{3/2}} \frac{e^{-i(\bar{S}_s - \Omega ta_s)}}{\sqrt{|\partial_t^2 S_s|}} + \frac{a(tb_l) a(ta_l) \sqrt{w(E(tb_l))}}{\sin(\omega_0 tb_l) [\omega_0 (ta_l - tb_l)/(2\pi)]^{3/2}} \frac{e^{-i(\bar{S}_l - \Omega ta_l - \frac{\pi}{2})}}{\sqrt{|\partial_t^2 S_l|}} \right|^2 , \quad (2)$$

where, (tb_s, ta_s) , (tb_l, ta_l) and $\bar{S}_{s,l} = S(ta_{s,l}, tb_{s,l})$ are the pairs of birth/arrival times and the corresponding semiclassical action for the short and the long trajectory of a particular harmonic, respectively. Equation (2) is valid for harmonic energies Ω in the plateau region, satisfying the condition $1 < (\Omega - I_p)/U_p < 3.1$. Notice that Eq.(2) has an additional term related to the derivative of

the action, $\partial_t^2 S$, which is the atto-chirp, respectively, associated to the long/short trajectory. This leads to additional energy spreading over the harmonics reducing the power in each by another factor of ω_0 . Therefore, in general, the scaling of HHG efficiency with the driving frequency is ω_0^5 at the cutoff and ω_0^6 in the plateau region for fixed harmonic wavelength. However, for the complete wavelength scaling other contributions have to be taken into account. For example, the medium characteristics, recombination amplitude and absorption cross section play an important role if cutoff extension is the target. In order to illustrate this statement, absorption limited HHG from neon is considered and the optimum drive wavelength for maximum conversion efficiency in the cutoff region is determined using Eq. (1). The result is displayed in Fig. 1(a) as a function of drive wavelength and cutoff energy. A global maximum for the efficiency in Ne is clearly observed for $\lambda_0 = 1.2 \mu\text{m}$ corresponding to $\Omega_{\text{cutoff}} = 450 \text{ eV}$. Although, the maximum conversion efficiency shifts for different λ_0 , the peak efficiency does not exhibit any strong dependence with the driver wavelength, in contradiction to the $\lambda_0^{-5..6}$ scaling. This behavior is also reproduced via numerical evaluation of the ITSM at constant field amplitude E_0 while varying ω_0 , as shown in Fig. 1 (b). The reason for this unexpected behavior is that in the range from 30 to 800 eV for Ne, the recombination amplitude, a_{rec} increases and the absorption cross section, σ decreases. In particular, the absorption cross section decreases more than two orders of magnitude over that range fully compensating for the reduction in the single atom response due to quantum diffusion.

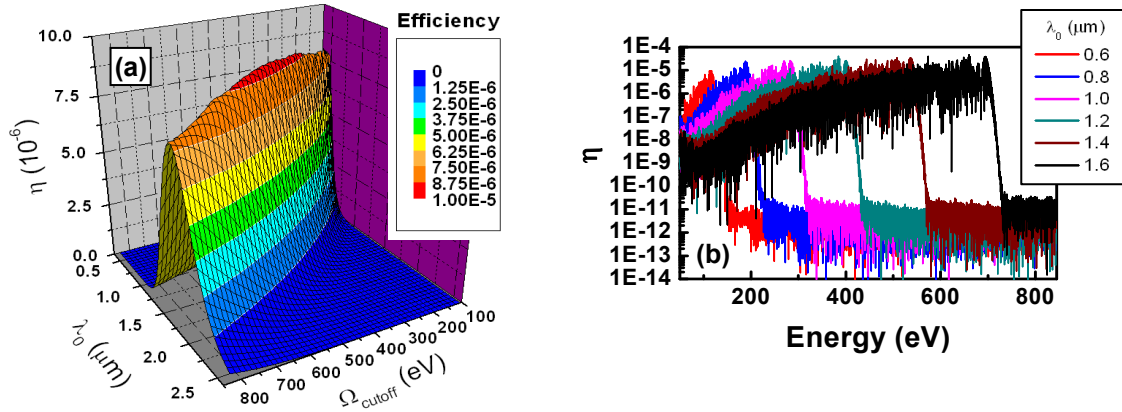


Figure 1: (a) Neon HHG efficiency at the cutoff region, as a function of the driver wavelength, λ_0 , and the cutoff energy, Ω_{cutoff} . (b) Full spectrum obtained considering a Gaussian pulse with $E_0 = 0.16$ a.u. for different driver wavelengths. For both cases absorption limited conditions and a 5-cycle-driver-pulse were assumed.

In summary, for fixed harmonic wavelength, a scaling for the HHG single atom response with the driving frequency of ω_0^5 at the cutoff and ω_0^6 at the plateau region were obtained. This result is in accordance with numerical simulations using the time dependent Schrödinger equation [4] which includes the single-atom response only, and with preliminary experimental results [5]. Besides the single-atom response, our derivation indicates that another major contribution to be considered in the wavelength scaling of the HHG efficiency is the medium characteristics, especially the absorption length, which may completely compensate for the drop in single-atom response. In this way, our derived formulas enable a complete HHG scaling analysis, simplify the HHG optimization problem and can be extremely useful in the development of any HHG based EUV and XUV sources.

References

- [1] A. Gordon and F. X. Kärtner, Phys. Rev. Lett. 95, 223901 (2005).
- [2] A. Gordon *et al.*, Phys. Rev. Lett. 96, 223902 (2006).
- [3] E. L. Falcão-Filho *et al.*, Opt. Express 17, 11217 (2009).
- [4] J. Tate *et al.*, Phys. Rev. Lett. **98**, 013901 (2007).
- [5] P. Colosimo *et al.*, Nature Physics, vol. 4, pp. 386-389, 2008.

Attosecond Photonics

Attosecond-Timing-Precision Photonics

Sponsors

Office of Naval Research (ONR), Contract N00014-02-1-0717

Air Force Office of Scientific Research (AFOSR), Contract FA9550-07-1-0014

Defense Advanced Research Projects Agency (DARPA), Contracts W911NF-04-1-0431 and HR0011-05-C-0155

Sandia National Laboratories, Contract 777117

Project Staff

Dr. Jungwon Kim, Andrew Benedick, Hyunil Byun, Jian Chen, Jonathan Cox, Umit Demirbas, Dr. Klaus Hartinger, Anatoly Khilo, Dr. Amir Nejadmalayeri, Dr. Dominik Pudo, Cheryl Sorace, and Professor Franz X. Kärtner

One of the most fascinating and interesting aspects of femtosecond mode-locked lasers is their noise properties [1]. In fact, the reason optical frequency combs and phase-controlled few-cycle pulses can be so successful is because of the excellent noise properties of mode-locked lasers. Mode-locked lasers have a unique characteristic of simultaneously generating low-noise optical and microwave signals in the form of extremely regularly spaced optical pulse trains. In particular, the ultra-low timing jitter of optical pulse trains can be used for the high-precision generation, distribution, measurement, and synchronization of optical and microwave signals. Recent measurements have shown that optical pulse trains generated from standard, passively mode-locked Er-fiber lasers can easily achieve sub-10-fs and sub-fs timing jitter for offset frequencies above 10 kHz and 100 kHz, respectively [2]. Such ultra-low-jitter optical pulse trains can not only improve the performance of existing systems that require higher timing precision and accuracy (such as analog-to-digital converters), but also reveal entirely new applications that were not previously possible (such as femtosecond timing synchronization for next generation light sources).

Here, we present a simple intuitive picture of the timing jitter scaling into the attosecond regime when transitioning from the traditional case of a microwave oscillator to the case of a mode-locked laser [3]. Fig. 1 shows the time-domain picture of microwave signals and optical pulse trains when emitted from an ensemble of microwave oscillators and mode-locked lasers, respectively. The zero crossings of the microwave signal and the pulse positions of the optical pulse train undergo a random walk due to the fundamental noise sources in the signal generation processes. For the microwave oscillator, the noise energy added to the cavity field within a cavity decay time due to the losses is equal to kT in thermal equilibrium. For the case of a lossy optical resonator, the equivalent noise energy added during a cavity decay time is $\hbar\omega_c$, instead of kT .

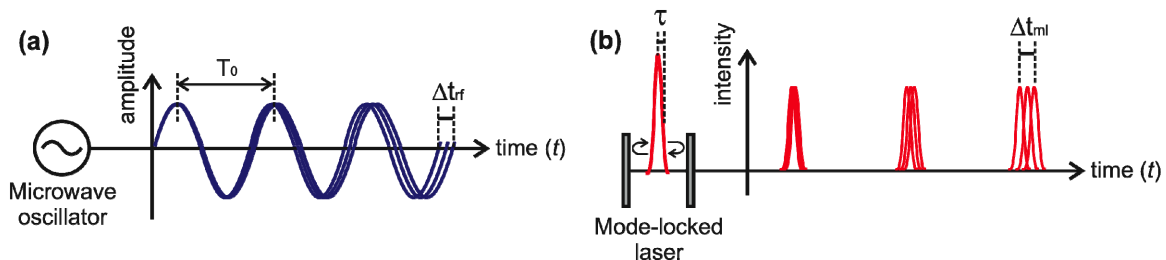


Figure 1: Random walk of (a) the phase of a microwave signal generated from a microwave oscillator and (b) the pulse position of an optical pulse train generated from a mode-locked laser.

The addition of thermal white noise leads to a random walk in the phase of the microwave oscillator or, equivalently, in the timing jitter of the zero crossings of the microwave signal. The timing jitter variance will then increase linearly over time. One can derive that the rate of increase (diffusion coefficient) of the timing jitter variance can be expressed as

$$\frac{d}{dt} \langle \Delta t_{rf}^2 \rangle = \frac{1}{(2\pi)^2} \cdot T_0^2 \cdot \frac{1}{W_{mode}} \cdot \frac{kT}{\tau_{cav,rf}} \quad (1)$$

where $\langle \Delta t_{rf}^2 \rangle$ is the timing jitter variance of the microwave signal, T_0 is the period of the microwave signal, W_{mode} is the intra-cavity energy stored in the resonator mode, kT is the thermal energy, and $\tau_{cav,rf}$ is the cavity decay time.

For optical pulse trains generated from mode-locked lasers, the timing jitter of the pulse position exhibits a similar relationship with the laser parameters as

$$\frac{d}{dt} \langle \Delta t_{ml}^2 \rangle = \frac{\pi^2}{6} \cdot \tau^2 \cdot \frac{1}{W_{pulse}} \cdot \frac{h\omega_c}{\tau_{cav,ml}} \quad (2)$$

where $\langle \Delta t_{ml}^2 \rangle$ is the timing jitter variance of the optical pulse train, τ is the pulse width (when the pulse intensity has $\text{sec}^2(t/\tau)$ -shape), W_{pulse} is the intra-cavity pulse energy, $h\omega_c$ is the photon energy, and $\tau_{cav,ml} (= T_{rt}/2g_s)$ is the cavity decay time (T_{rt} is the cavity round-trip time and g_s is the saturated gain).

Since the laser operates at optical frequencies, the noise energy added within the cavity decay time is $h\omega_c$ rather than thermal noise kT . This is, in fact, a disadvantage for the noise performance of the optical oscillator, because the added quantum noise is much larger than the thermal noise. At 1550-nm center wavelength and room temperature (300 K), the photon energy is ~30 times greater than the thermal energy. However, the winning factor for the mode-locked laser is its ultra-short pulse duration. By concentrating a large number of photons in an ultra-short pulse duration, e.g. ~100 fs and below, the pulse position is robust against perturbations caused by photon noise (such as spontaneous emission noise). For example, a mode-locked laser generating a 100-fs pulse width has a scaling factor of 10^6 when compared to a 10-GHz microwave oscillator with a period of 100 ps. Assuming that the mode/pulse energy and the cavity decay times are similar, the mode-locked laser can easily achieve two orders of magnitude less timing jitter when compared to the microwave oscillator. Using Eq. (2), the quantum-noise-limited timing jitter of mode-locked lasers can be theoretically evaluated. A numerical example using parameters of a typical stretched pulse Er-fiber laser, center wavelength = 1550 nm, $W_{pulse} = 2$ nJ, $T_{rt} = 20$ ns, $g_s = 0.05$, and $\tau = 100$ fs, shows that the quantum-noise-limited timing jitter integrated from 10 Hz to 25MHz (Nyquist bandwidth) is only 116 as. In reality, however, mode-locked lasers have additional noise sources and nonlinear dynamics that may further increase the timing jitter beyond the simple quantum noise limit derived here. Examples are mechanical vibrations, the coupling of intensity noise to timing noise, and the coupling of center frequency fluctuations to timing noise. Recent timing jitter measurements of various types of mode-locked lasers have shown ~10- to 30-fs jitter level. Although these are impressive results when compared to most commercially available, high-quality microwave oscillators, there is still much room for improvements in timing noise by suppressing 'technical' noise sources to reach the predicted attosecond-jitter performance.

At MIT Optics and Quantum Electronics Group, a wide range of research has been conducted in optimizing the timing jitter of mode-locked lasers and developing attosecond-precision, chip-scale signal processing systems based on mode-locked lasers. In this year's Report, progresses in (a) timing jitter measurement using PPKTP-waveguide devices, (b) high-speed Si modulator design, (c) Si/SiN filter design, and (d) integrated Er-waveguide mode-locked lasers are introduced.

References

- [1] H. A. Haus and A. Mecozzi, "Noise of mode-locked lasers," *IEEE J. Quantum Electron.* 29(3): 983-996 (1993).
- [2] J. Kim, J. Chen, J. Cox and F. X. Kärtner, "Attosecond-resolution timing jitter characterization of free-running mode-locked lasers," *Opt. Lett.* 32(24): 3519-3521 (2007).
- [3] J. Kim and F. X. Kärtner, "Attosecond-precision ultrafast photonics," to appear at *Laser & Photonics Reviews* (2009).

Attosecond resolution timing jitter measurements with periodically poled KTP waveguides

Sponsors

Defense Advanced Research Program Agency, Contract HR0011-05-C-0155
Air Force Office of Scientific Research (AFOSR), FA9550-07-1-0014

Project Staff

Dr. Amir H. Nejadmalayeri, Dr. Franco N. C. Wong, Dr. Tony D. Roberts, Dr. Philip Battle, and Professor Franz X. Kärtner

Mode locked lasers can inherently generate pulse trains with very low timing jitter—down to the attosecond level or even lower [1]. As a result, they are excellent candidates for applications where timing accuracy is of extreme importance, such as high speed analog/digital conversion and precise synchronization.

Although the measured jitter has been very low in all of these studies, theoretical limits are still much lower, indicating that either there are unmodeled additional sources of noise, or the measurement techniques lack resolution. As a result, in order to verify the ultralow timing fluctuation property of mode locked lasers, and to exploit it for timing purposes one has to be able to precisely evaluate their jitter performance.

A variety of methods have been devised for this purpose. Optical cross correlation is one of them [2]. Recently, it was experimentally demonstrated that a balanced optical cross correlator could show unprecedented precision in measuring the timing jitter of optical pulse trains [4]. The technique works based on type-II second harmonic generation (SHG) between two pulses whose relative timing fluctuation is of interest.

The orthogonality of the polarizations (type-II operation) is essential to ensure that the electrical signal will vanish whenever one of the signals ceases to exist, henceforth background free operation. Moreover, large phase matching (PM) bandwidth is crucial to guarantee efficient SHG of ultrashort laser pulses. In this regard, periodically poled potassium titanyl phosphate (PPKTP) is the nonlinear material of the choice, since it has a large type-II PM bandwidth in the telecom C band at room temperature.

In Ref. 11, using bulk PPKTP, a SHG conversion efficiency of 0.4% was obtained in the telecom band. The cross correlation method was later applied to measure the timing jitter of free running mode locked lasers down to a resolution of 470 attosecond (as) for an offset frequency range of 10 kHz–10 MHz [4]. However, obtaining resolutions at the attosecond level requires two orders of magnitude improvement in SH signal detection, which is currently not feasible with the typical tens of milliwatts fundamental harmonic (FH) power levels. As a result, we seek to use waveguides instead of bulk crystals to significantly improve the efficiency of the SHG process.

Although guided wave SHG has previously been demonstrated in KTP, those studies were either of type-I, or in segmented waveguides. To our knowledge, this is the first time that continuous waveguides in electric field poled KTP are utilized to demonstrate type-II SHG. The SHG process in the non-segmented devices studied in this work exhibits an overall pulse mode efficiency of 36%, a 90-fold improvement over previous bulk crystal results [3]. This will pave the way to few and eventually sub-attosecond resolution in timing jitter measurements of optical pulse trains, as well as precision timing distribution in large scale facilities.

The measured SH power (PSH) versus total (both polarizations) FH power (PFH) at the output of the waveguide are depicted in Figure 2 that are related together by $P_{SH} \approx 0.029P_{FH}^2$, as determined by a quadratic fit to the measurement results.

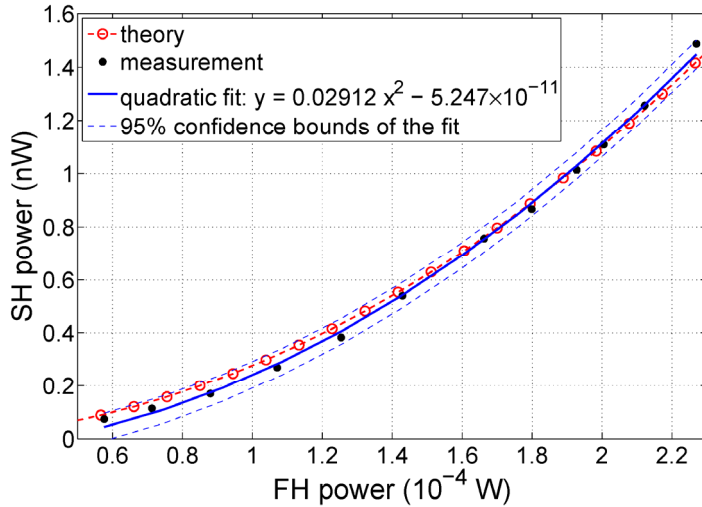


Figure 2: Type-II SHG in a 1-cm long PPKTP Waveguide

To evaluate the timing precision of the optical cross correlator that can be built based on the PPKTP waveguide presented here, we consider the photo-detection process when the device operates in the pulsed mode.

For the SH detection process, we designed a balanced trans-impedance amplifier (TIA) based photoreceiver. The TIA has a trans-impedance gain of 2 M Ω over the band of DC–23 MHz. The bandwidth enables complete noise measurement—up to Nyquist frequency—of mode locked lasers with repetition rates as high as 44 MHz. The SPICE simulations of our designed TIA show an integrated output referred rms voltage noise of \approx 19 mV over the frequency range of 1 Hz–23 MHz.

As an example, an Erbium doped fiber laser (EDFL) that generates a train of $\tau = 200$ fs optical pulses at a repetition rate of $f_r = 44$ MHz, with an average power of 15 mW, leads to $P_{av} = 5$ mW of excited FH in the waveguide. At 1560 nm wavelength, a length of $L \approx 2$ mm is needed for the two orthogonally polarized pulses to walk through each other, as described elsewhere [5]. If coupled mode equations are solved for the 2 mm length using the experimental parameters [5], a normalized conversion efficiency of $\eta_0 = 1.6\%/(\text{W cm}^2)$ will be obtained. For the above laser parameters, this translates to $\eta \approx \eta_0 L^2 P_{av} / (\tau f_r) = 36\%$ conversion efficiency in the pulsed operating mode, which is 90 times larger than the previous bulk results [3]. There, a zero crossing slope of ≈ 25 V/ps was measured. As a result, the 2 mm long guided wave device will have an estimated slope of larger than 2.25 V/fs. Dividing the 19 mV output noise of the TIA by the 2.25 V/fs slope, the timing resolution of the apparatus is estimated to be ≈ 8 as.

References

- [1] H. A. Haus and A. Mecozzi, “Noise of mode-locked lasers,” *IEEE J. Quantum Electron.* 29, 983–996 (1993).
- [2] L. A. Jiang, S. T. Wong, M. E. Grein, E. P. Ippen, and H. A. Haus, “Measuring timing jitter with optical cross correlations,” *IEEE J. Quantum Electron.* 38, 1047–1052 (2002).
- [3] J. Kim, J. Chen, Z. Zhang, F. N. C. Wong, F. X. Kärtner, F. Loehl, and H. Schlarb, “Long-term femtosecond timing link stabilization using a single-crystal balanced cross correlator,” *Opt. Lett.* 32, 1044–1046 (2007).
- [4] J. Kim, J. Chen, J. Cox, and F. X. Kärtner, “Attosecond-resolution timing jitter characterization of free-running mode-locked lasers,” *Opt. Lett.* 32, 3519–3521 (2007).
- [5] A. H. Nejadmalayeri, F. N. C. Wong, T. D. Roberts, P. Battle, and F. X. Kärtner, “Guided wave optics in periodically poled KTP: quadratic nonlinearity and prospects of attosecond jitter characterization,” *Opt. Lett.*, accepted for publication (2009).

High-Speed Silicon Electro-Optic Mach-Zender Modulators

Sponsors

Defense Advanced Research Projects Agency (DARPA) under Grant W911NF-04-1-0431

Project Staff

Cheryl Sorace, Dr. Stephen Spector, and Professor Franz X. Kaertner

As transistor density in integrated circuits increases, power density and interconnect latency become more and more problematic. CMOS compatible silicon photonics has emerged as a promising contender for overcoming these problems. In particular, when seeking to transmit data between multiple processing cores and memory modules, photonic links are likely to be faster, have higher bandwidth, and use less power than traditional, purely electronic solutions [1]. A crucial part of any photonic link would be the optical modulator by which the desired signal is converted from digital to optical form.

There are many types of optical modulator, each of which have their own benefits and drawbacks. Because we wish our modulator to be CMOS compatible, we work in silicon. Modulators can be made in either ring or Mach-Zender configurations. Ring modulators have a smaller footprint and require less power, but have smaller bandwidth and are sensitive to temperature and fabrication variations. Mach-Zender modulators require more power and space, but have larger bandwidth and are more robust to variations. [2]

We design a Mach-Zender modulator that exploits the plasma dispersion effect in a PN-junction silicon diode—that is the change in optical index of refraction with carrier density—to modulate our light. This change is governed by Soref's equation [3]:

$$\Delta n = -8.8e-22 \cdot \Delta N_e - 8.5e-18 \cdot (\Delta N_h)^{0.8}$$

To accomplish this modulation the number of carriers inside the device needs to be changed either through injection or depletion of carriers. Injection of carriers leads to modulators with high sensitivity (that is lower $V_{pi}L$), but lower operation frequencies, because modulator speed is ultimately limited by carrier lifetime—usually on the order 2 ns [4]. High speed modulation requires a movement to depletion modulators where speed is no longer limited by carrier lifetime.

In a PN junction modulator, moving to depletion operation requires movement to reverse bias. This requires higher voltage operation and dramatically decreases sensitivity [1]. The DC sensitivity can be improved by improving the overlap of the mode with the modulated part of the depletion region. Previous work in the group involved modulators with a vertical pn-junction near one side (see Figure 1a). Movement to a horizontal junction can increase the mode overlap (Figure 1b). Below we simulate a reversed biased modulator using a horizontal junction. We optimize the height and the doping of the waveguides and we compare the design's DC performance to that of our group's previous design in Figure 2. As can be seen, the performance is significantly improved. We expect about a seven fold increase in device sensitivity ($V_{pi}L$) [5].

In reverse bias, the operating frequency is limited by the RC time constant of the diode. (Movement of carriers occurs on the time scale of the dielectric relaxation time, which would limit performance to on the order of THz if the RC time constant did not reduce it first). We note that, because the internal resistance of the modulators is quite low (below about 0.3 Ω -cm), we can ignore it in comparison to the 50 Ω load from the measurement set up [5]. It is then the capacitance of the device that dominates the frequency cutoff of operations. This capacitance is dominated by the diode junction capacitance and increases as the area of the junction increases and as the equilibrium width of the depletion region decreases (that is, as the doping level rises). Turning the junction from vertical to horizontal thus increases the capacitance, as does increasing the doping level to achieve better sensitivity. Therefore, we predict that our new device will only work up to 10GHz, and not the 26GHz we achieved before [5]. We note that if we could reduce

the resistance present in our measurement probes we would be able to operate our devices at significantly higher frequencies.

One downside of the plasma dispersion effect is that the same carriers that create the desired index change also introduce loss into the device. The carrier-induced losses are given by [3]:

$$\Delta\alpha = 9.1e-22 \cdot (\Delta N_e)^{1.22} + 2.5e-20 \cdot (\Delta N_h)^{1.13}$$

We choose a doping level of $1e18 \text{ cm}^{-3}$ for the n-type and $6e17 \text{ cm}^{-3}$ for the p-type regions of our modulator in order to balance the increase in index change against the increase in optical loss. In conclusion, the switch to a horizontal junction in a reversed biased PN junction MZ silicon modulator can significantly improve device sensitivity, allowing lower operating voltages to be used in devices capable of achieving desired high modulation frequencies. However, when designing a device it may be necessary to trade off sensitivity for better optical loss characteristics.

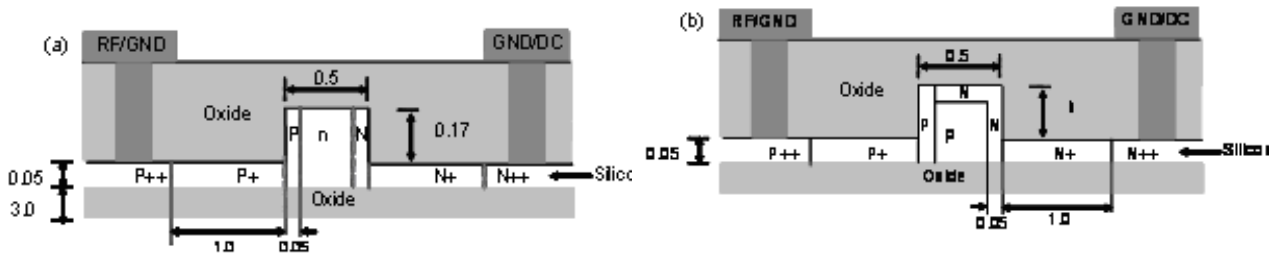


Figure 1. a. Old modulator design with vertical PN junction. b. New modulator design with horizontal junction. [6]

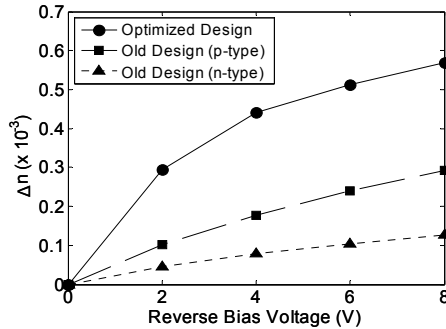


Figure 2. Simulation results comparing old and new modulator design in reverse biased operation. Old design is plotted with the center of the waveguide doped both n-type and p-type. The p-type doping shows a greater change in effective index because each hole causes a larger change in refractive index than each electron. In the new design the center of the waveguide is doped p-type. [6]

References:

[1] F. Gan, High-Speed Silicon Electro-Optic Modulator for Electronic Photonic Intergrated Circuits, Ph.D. thesis, Massachusetts Institute of Technology, June 2007.
 [2] D. Marris-Morini, L. Vivien, J. M. Fédéli, E. Cassan, P. Lyan, S. Laval, "Low loss and high speed silicon optical modulator based on a lateral carrier depletion structure," *Optics Express*, Vol, 16, pp. 334-339, Jan. 2008
 [3] R. A. Soref and B. R. Bennet, "Electrooptical Effects in Silicon", *IEEE Journ. of Quantum Elec.*, vol QE-23, pp. 123-129, Jan. 1987.
 [4] G.-R. Zhou, M. W. Geis, S. J. Spector, F. Gan, M. E. Grein, R. T. Schulein, J. S. Orcutt, J. U. Yoon, D. M. Lennon, T. M. Lyszczarz, E. P. Ippen, and F. X. Kärtner, "Effect of carrier lifetime on forward-biased silicon Mach-Zehnder modulators," *Optics Express*, Vol, 16, pp. 5218-5226, Apr. 2008.
 [5] S.J. Spector, C.M. Sorace, M.W. Geis, M.E. Grein, J.U. Yoon, T.M. Lyszczarz, E.P. Ippen, F.X. Kärtner, "Operation and Optimization of Silicon-Diode-Based Optical Modulators" accepted by *JSTQE*

Silicon Microring Resonator Filter Banks for Photonic Analog-To-Digital Conversion

Sponsors

Defense Advanced Research Projects Agency (DARPA) under Grant W911NF-04-1-0431

Project Staff

Anatol Khilo, Charles W. Holzwarth, Marcus S. Dahlem, Prof. Henry I. Smith, Prof. Erich P. Ippen and Prof. Franz X. Kärtner

In optically-sampled frequency-demultiplexed analog-to-digital converters, high sampling rate is achieved by splitting the modulated pulse train into several channels in frequency domain, and processing these channels independently [1]. Frequency-demultiplexing can be achieved using an array of microring resonator filters, which allows to achieve high spectral efficiency, high suppression of adjacent channels, low insertion loss, as well as small footprint on a chip.

We have previously worked on implementing the filter bank with silicon-rich nitride as the core material [2-3]; the results were promising, however, there was inconsistency in material loss which resulted in an increased drop loss of about 6 dB in the fabricated 20-channel SiN filter bank. We have therefore switched to silicon as the core material. In addition to consistently low loss (drop loss of ~ 0.5 dB), using silicon is preferable in terms of integration with the rest of the ADC components, such as carrier-injection Si modulators and Si or germanium photodiodes and eventually electronics, on the same chip. To overcome high sensitivity of silicon microring filters to fabrication errors, an error-tolerant design of Si waveguides was used [4]. Figures 1(a) and (b) show the transmission characteristics of the fabricated 2-channel and 20-channel Si microring resonator filter banks, respectively [5, 6]. The characterization of the 20-channel filter bank is still in progress, therefore only 4 channels are shown in Figure 1(b). Thermal tuning with microheaters fabricated on top of the filters was used to compensate for frequency misalignments. The 3dB-bandwidth of the filters is about 21GHz, channel spacing is 80GHz, drop loss is about 0.5-1.5dB, and crosstalk with the adjacent channel is less than -30dB. These performance characteristics satisfy the requirements of the 40Gsa/s photonic ADC which is being pursued in the DARPA EPIC program [5].

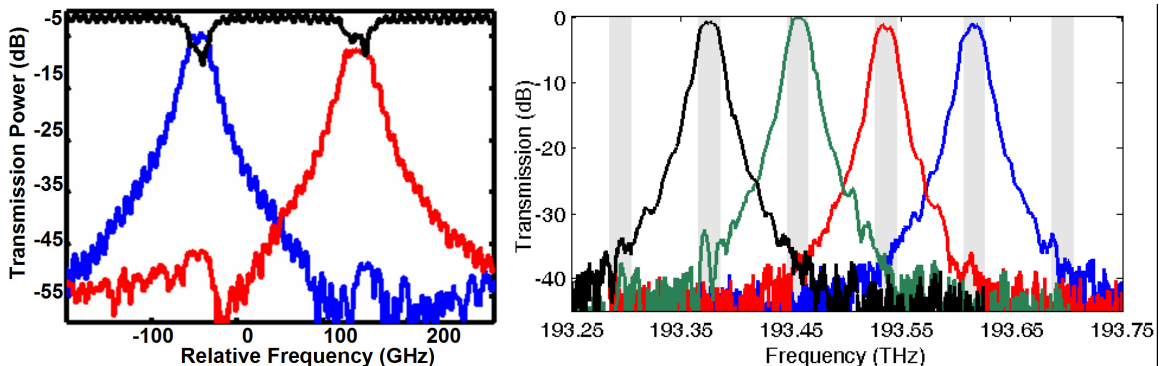


Figure 1: Measured frequency responses of (a) 2-channel Si bank, without frequency tuning, and (b) 20-channel Si bank (only 4 channels are shown), with thermal frequency tuning.

Using Si as the waveguide core material has one drawback, namely, the possibility of nonlinear effects due to two-photon absorption (TPA) in Si impacting ADC accuracy. In microring resonator filters, TPA results in signal-dependent absorption, because carriers generated due to TPA change the refractive index and thus resonance frequency of the filters. Figure 2 shows the change in drop loss and resonance frequency of a two-ring filter as a function of pulse energy. The filters were assumed to have 25GHz bandwidth and 80GHz channel spacing, and 1THz FSR; the pulse power enhancement inside the ring was 10. The pulse duration at the output and inside the ring resonator was 50ps (corresponding to 25GHz filter bandwidth). The pulse energies needed to achieve 8, 9, and 10 bits, as limited by shot noise, are shown with vertical lines. The

levels of drop loss and filter frequency variations limiting ENOB to 6, 8, and 10 bits are shown with horizontal lines. These levels were calculated for the case of 10GHz applied RF signal assuming 50% modulation depth. We see that for this system, the accuracy limitations due to Si nonlinearities are negligible at 8 bit energy level but start to limit the accuracy at 9 bit energy level. At energy level required for 10 bits accuracy goes below 6 bits primarily due to TPA inside the ring filters. To eliminate the impact of nonlinearities at high powers required for achieving 10 bits, an improved filter designs with smaller internal power enhancement can be used. Alternatively, digital error correction algorithms can be used to compensate for the nonlinear distortions.

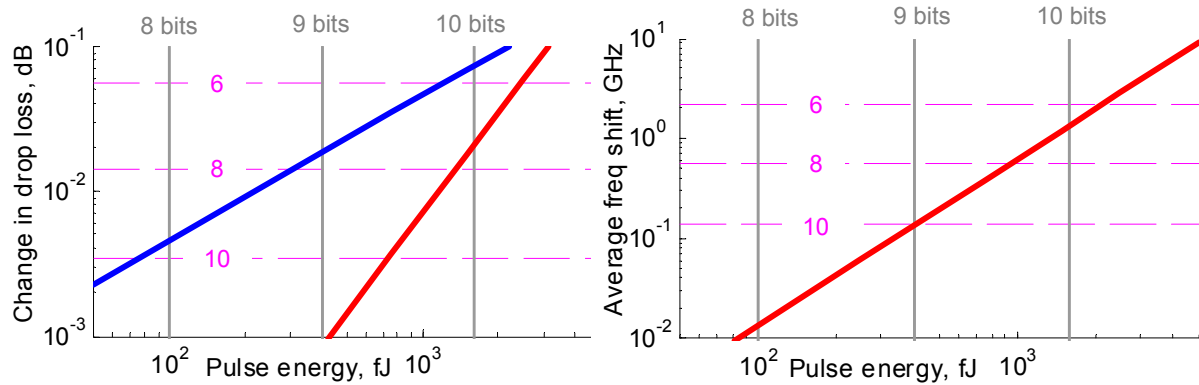


Figure 2. Change in drop loss (left) and ring resonance frequency (right) due to two-photon absorption (blue line) and free carrier dispersion (red line). The horizontal lines show levels necessary to achieve 6, 8, and 10 effective bits; the vertical lines show power needed to 8, 9, and 10 bits.

References

- [1] M.Y. Frankel, J.U. Kang, R.D. Esman, "High-performance photonic analogue-digital converter," *Electron. Lett.* 33(25): 2096–97 (1997).
- [2] C. W. Holzwarth, T. Barwicz, M. A. Popovic, P. T. Rakich, E. P. Ippen, F. X. Kartner, and H. I. Smith, "Accurate resonant frequency spacing of microring filters without postfabrication trimming," *J. Vac. Sci. Technol. B* 24(6): 3244–3247 (2006).
- [3] C.W. Holzwarth, R. Amatya, M. Dahlem, A. Khilo, F. X. Kaertner, E. P. Ippen, R. J. Ram and Henry I. Smith, "Fabrication strategies for filter banks on microring resonators," *J. of Vac. Sci. and Technol. B* 26(6): 2164–2167 (2008).
- [4] M. A. Popovic, T. Barwicz, E. P. Ippen and F. X. Kärtner, "Global design rules for silicon microphotonic waveguides: Sensitivity, polarization and resonance tunability," paper CTuCC1, *Conference on Lasers and Electro-Optics (CLEO)*, May 2006.
- [5] C.W. Holzwarth, "Material Selection and Nanofabrication Techniques for Electronic Photonic Integrated Circuits," PhD. Thesis, Massachusetts Institute of Technology, Cambridge MA (2009).
- [6] C. W. Holzwarth, R. Amatya, M. Araghchini et. al., "High speed analog-to-digital conversion with silicon photonics," *Proc. SPIE* 7220, 72200B (2009).

Nanophotonics

Design of Silicon Photonic Microcavities for Optical Switching

Sponsors

BM Zurich Research Laboratory, NSF MRSEC, AFOSR FA9550-07-1-0014

Project Staff

M. S. Dahlem, S. Schönenberger, T. Stöferle, N. Moll, R. F. Mahrt, B. J. Offrein, T. Wahlbrink, J. Bolten, T. Plötzing, M. Waldow, M. Först, H. Kurz, S. Götzinger, V. Sandoghdar, and Professor E. P. Ippen

Silicon photonics is a fast growing research field, and the compatibility with standard CMOS technology offers innumerable advantages over traditional optical communication solutions with respect to size, cost and power.

The increasing integration density enables fabrication of chip-to-chip and on-chip optical components, such as optical interconnects [1], and photonic crystal (PhC) microcavities [2-4]. These microcavity structures open up the feasibility of highly integrated ultrafast electro-optical modulators due to their small active optical volume. One of the limiting factors for the quality factor Q of such structures is the mode mismatch between the waveguide region and the periodic structure. This mode mismatch can be reduced by tapering the structure adiabatically [5,6].

Our proposed structure for the optical switch is based on a chirped-holes approach to the photonic crystal microcavity, where each tapered region is formed by 4 holes of decreasing size. A silicon-on-insulator (SOI) wafer is used as a platform to build the device, and the electro-optic modulation is performed through a carrier-injection-based p-i-n junction. Figure 1 illustrates the layout of the structure. The PhC microcavity and the p-i-n junction are built in the silicon layer ($n_{\text{Si}} = 3.44$), with silica undercladding ($n_{\text{SiO}_2} = 1.46$) and polymethyl methacrylate (PMMA) or hydrogen silsesquioxane (HSQ) overcladding ($n = 1.46$).

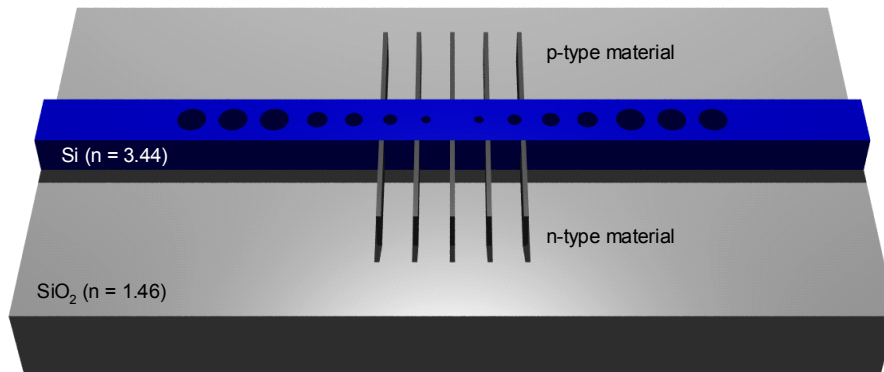


Figure 1 – Layout of the proposed electro-optic modulator, built on a SOI platform. The p-i-n junction is formed by doping the adjacent silicon with n-type and p-type materials.

The intrinsic region of the p-i-n junction is the PhC waveguide itself, and the n- and p- type regions are formed by doping the adjacent silicon regions. Our approach consists in fabricating cross waveguides, perpendicular to the main PhC microcavity waveguide, that can minimize the

perturbation of the optical mode inside the cavity. These cross waveguides are therefore placed at the nulls of the electric field and do not change the overall Q factor of the structure. The microcavity structure is designed by optimizing the quality factor Q of the isolated cavity using a 3D finite difference time-domain (FDTD) package [7]. Additional in- and out-coupling waveguides will limit the Q factor to a few thousands, allowing optical switching times in the order of a few picoseconds [8].

The structure is optimized to have a resonant wavelength around 1550nm. Simulations are performed for TE-like radiation, i.e., with the electric field parallel to the wafer surface. The quality factor Q of the structure is about 1700, with a modal volume $V_m \sim 0.55 (\lambda_0/n)^3$. The top view electric field distribution inside this structure is represented in Figure 2. As seen, the field extends beyond the center cavity limits into the tapered region, changing adiabatically from the cavity mode into the PhC mode.

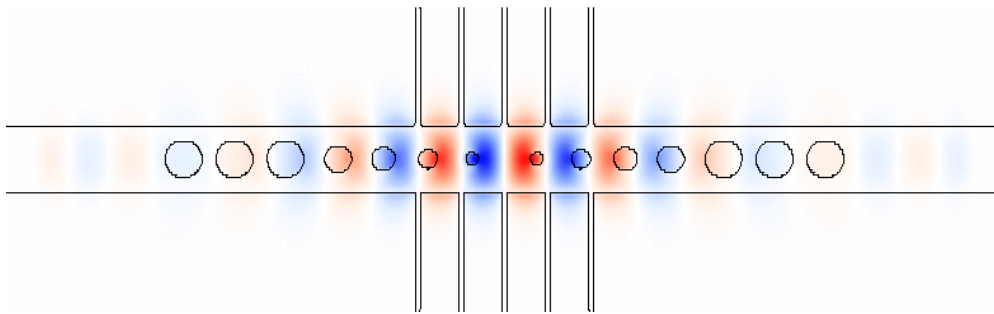


Figure 2 – Top view of the electric field pattern inside the active structure.

The transmission spectrum of this structure is illustrated in Figure 3, and shows a strong resonant mode around 1550 nm, right in the middle of the bandgap.

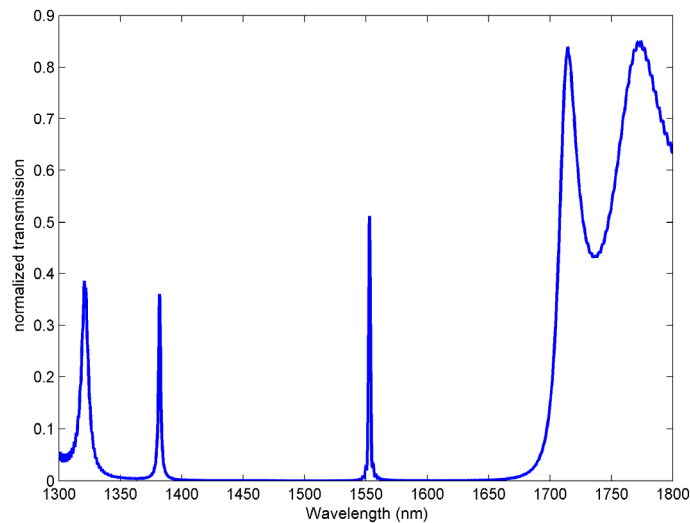


Figure 3 – Transmission spectrum of the active structure.

In order to operate as an optical switch, small refraction index changes will be induced in the cavity. For small changes, the resonant frequency shifts with the index of refraction according to the following relation:

$$\frac{\delta\nu}{\nu} = -\sigma \frac{\delta n}{n}$$

where σ is the confinement factor. In addition to the frequency shift, loss is induced in the cavity, reducing the quality factor. This by itself will “turn off” the resonant mode. Additional modeling on this effect is being considered. In addition, initial test structures have been fabricated – Figure 4 shows a SEM of one of such structures.

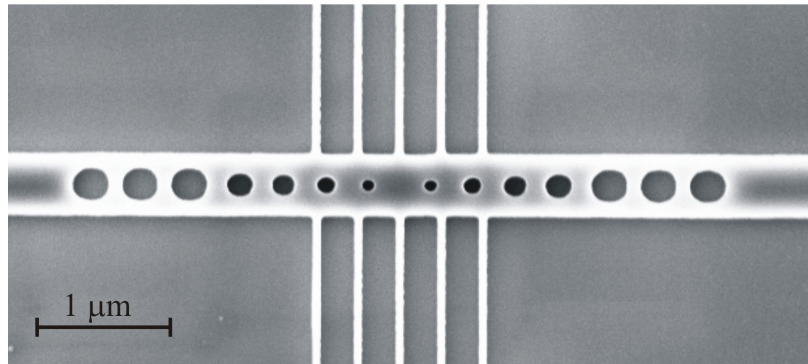


Figure 4 – SEM image of a PhC microcavity with waveguides for future doping and electrical contacts.

References

- [1] P. T. Rakich, M. S. Dahlem, S. Tandon, M. Ibanescu, M. Soljacic, G. S. Petrich, J. D. Joannopoulos, L. A. Kolodziejski, and E. P. Ippen, “Achieving centimetre-scale supercollimation in a large-area two-dimensional photonic crystal,” *Nature Materials* 5(2), 93-96 (2006).
- [2] P. R. Villeneuve, D. S. Abrams, S. Fan, and J. D. Joannopoulos, “Single-mode waveguide microcavity for fast optical switching,” *Optics Letters* 21, 2017-2019 (1996).
- [3] J. S. Foresi, P. R. Villeneuve, J. Ferrera, E. R. Thoe, G. Steinmeyer, S. Fan, J. D. Joannopoulos, L. C. Kimerling, H. I. Smith, and E. P. Ippen, “Photonic-bandgap microcavities in optical waveguides,” *Nature* 390, 143-145 (1997).
- [4] D. J. Ripin, Kuo-Yi Lim, G. S. Petrich, P. R. Villeneuve, S. Fan, E. R. Thoen, J. D. Joannopoulos, E. P. Ippen, and L. A. Kolodziejski, “Photonic band gap airbridge microcavity resonances in GaAs/AlxOy waveguides,” *Journal of Applied Physics* 87, 1578-1580 (2000).
- [5] C. Sauvan, G. Lecamp, P. Lalanne, and J. Hugonin, “Modal-reflectivity enhancement by geometry tuning in Photonic Crystal microcavities,” *Optics Express* 13, 245-255 (2005).
- [6] P. Velha, J. C. Rodier, P. Lalanne, and J. P. Hugonin, D. Peyrade, E. Picard, T. Charvolin, and E. Hadji, “Ultracompact silicon-on-insulator ridge-waveguide mirrors with high reflectance,” *Applied Physics Letters* 89, 171121 (2006).
- [7] <http://ab-initio.mit.edu/wiki/index.php/Meep>
- [8] R. Harbers, N. Moll, D. Erni, G. Bona, and W. Bächtold, “Efficient coupling into and out of high-Q resonators,” *Journal of the Optical Society of America A* 21(8), 1512-1517 (2004).

Post-Fabrication Thermal Trimming of an Eleven-Channel Second-Order Silicon Microring Resonator Filterbank

Sponsors: DARPA Contract W911NF-04-1-0431, NSF MRSEC, AFOSR Contract FA9550-07-1-0014

Research Staff:

M. S. Dahlem, C. W. Holzwarth, M. A. Popović, A. Khilo, Professor F. X. Kaertner, Professor H. I. Smith, and Professor E. P. Ippen

Multi-channel high-order microring resonators are essential components for enabling low-cost highly integrated wavelength division multiplexing (WDM) systems and photonic integrated circuits. Silicon-on-insulator (SOI) platforms allow low-loss single-mode propagation in submicron structures and micron-sized bending radii at wavelengths of $1.5\ \mu\text{m}$ [1]. High dimensional control and sidewall quality are required to correctly meet the device parameters, and post-fabrication trimming may be needed. This can effectively be achieved by thermal tuning, due to the high thermo-optic coefficient of silicon [2,3]. In silicon, multi-channel single-ring filters have been demonstrated [4], as well as tunable single-channel high-order filters [5]. Previous work reports progress in fabricating a multi-channel second-order silicon filterbank [6], and we have also demonstrated similar work in silicon-rich silicon nitride [7]. Here we demonstrate a successfully aligned second-order silicon filterbank with eleven channels, channel-bandwidth of 20 GHz and channel-spacing of 124 GHz.

The filterbank was designed to have a ~ 20 GHz channel-bandwidth and $>30\text{dB}$ of extinction at an adjacent channel spaced by $>80\text{GHz}$. The silicon waveguides were designed to reduce sensitivity to sidewall roughness and dimensional variations [8], with cross-sections of $\sim 600 \times 100\text{nm}$. The filterbank was fabricated on a SOI wafer with a $3\ \mu\text{m}$ -thick oxide undercladding, and a 106nm silicon layer (thinned from 220nm), similar to our previous works [5,9]. The device was spin coated with a $1\ \mu\text{m}$ -thick hydrogen silsesquioxane (HSQ) layer [10], and titanium microheaters were fabricated on top of the HSQ for thermal tuning, resulting in typical heater-resistance values between 1 and 2 k Ω .

The fabricated individual rings show Q factors of $\sim 250\text{k}$ and $\sim 130\text{k}$, without and with the titanium heaters. This corresponds to propagation losses of about 2-2.5dB/cm and 4.5dB/cm, respectively. To demonstrate the wide and precise thermal tuning capabilities, we used a filterbank with extensive fabrication mismatches. Fig. 1(a) shows the drop-port responses of the eleven channels before any thermal trimming, overlaid with a targeted 124 GHz-spaced 20 GHz-bandwidth grid. Most of the channels are misaligned, and the spacing is non-uniform. Both rings of an individual channel are carefully tuned, and then the whole channel is shifted to its targeted frequency. The measured tuning efficiency is $\sim 28\ \mu\text{W}/\text{GHz}/\text{ring}$. Fig. 1(b) shows the tuned drop-port responses. The channel-bandwidth is $\sim 20\text{GHz}$, and the extinction at the adjacent channels is $>35\text{dB}$. The thru-port response (not shown) gives a drop loss of about 2dB. In order to achieve this result, 22 microrings need to be precisely tuned. This is done with a multi-channel DAC board which controls the power of each heater individually. Several channels were tuned simultaneously, limited by the number of control ports available from the DAC only. Cross-talk between adjacent rings and adjacent channels is low and can easily be compensated for. Precise tuning of any individual channel can be particularly challenging if any of the resonant wavelengths of a different channel naturally coincides with the targeted one. The total power needed for complete tuning of the eleven channels at the specific 124 GHz-spaced grid is about 180 mW.

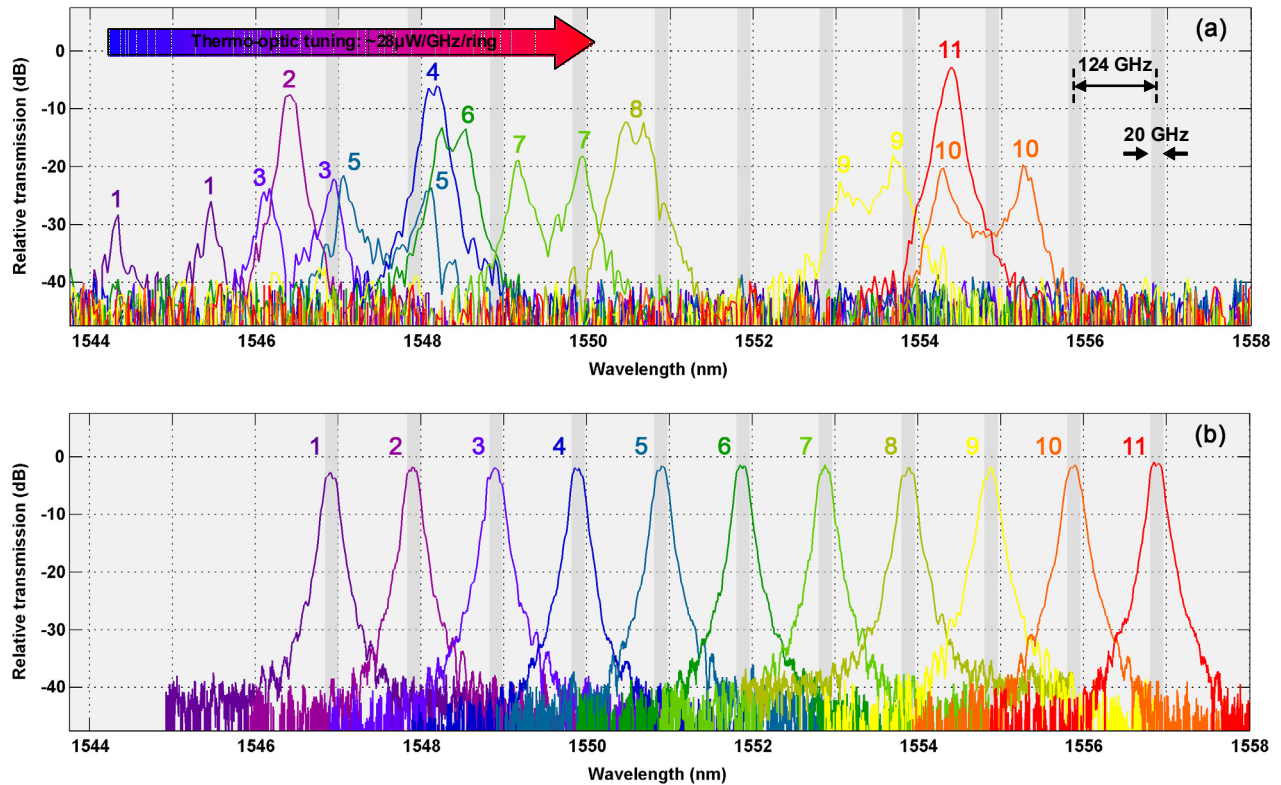


Fig.1. Drop-port response of an eleven-channel second-order silicon filterbank (a) before and (b) after thermal trimming. The targeted channel spacing is 124 GHz, and the measured channel bandwidth is 20GHz. Extinction of any channel is over 35dB at the adjacent channels.

We demonstrated a wide thermo-optic trimming of an eleven-channel second-order filterbank fabricated on a SOI platform. The demonstrated filterbank has a 124 GHz channel spacing, and a single channel bandwidth of about 20 GHz. The tuning efficiency was measured to be $\sim 28 \mu\text{W}/\text{GHz}/\text{ring}$, and the total power dissipated on the chip is estimated to be close to 180 mW.

References

- [1] Y. A. Vlasov and S. J. McNab, "Losses in single-mode silicon-on-insulator strip waveguides and bends," *Optics Express*, vol. 12, pp. 1622-1631 (2004).
- [2] F. Gan, T. Barwicz, M. A. Popović, M. S. Dahlem, C. W. Holzwarth, P. T. Rakich, H. I. Smith, E. P. Ippen, and F. X. Kärtner, "Maximizing the Thermo-Optic Tuning Range of Silicon Photonic Structures," TuB3.3, *IEEE/LEOS Photonics in Switching 2007 Conference*, San Francisco, CA, August 2007
- [3] M. A. Popović, T. Barwicz, M. S. Dahlem, F. Gan, C. W. Holzwarth, P. T. Rakich, M. R. Watts, H. I. Smith, F. X. Kärtner, and E. P. Ippen, "Hitless-Reconfigurable and Bandwidth-Scalable Silicon Photonic Circuits for Telecom and Interconnect Applications," OTuF4, *Optical Fiber Communication (OFC) Conference*, San Diego, CA, February 2008.

- [4] M. H. Khan, H. Shen, Y. Xuan, S. Xiao, and M. Qi, "Eight-Channel Microring Resonator Array with Accurately Controlled Channel Spacing," CTuNN6, *Conference on Lasers and Electro Optics (CLEO)*, San Jose, CA, May 2008.
- [5] M. A. Popović, T. Barwicz, M. S. Dahlem, F. Gan, C. W. Holzwarth, P. T. Rakich, H. I. Smith, E. P. Ippen, and F. X. Kärtner, "Tunable, Fourth-Order Silicon Microring-Resonator Add-Drop Filters," *European Conference on Optical Communication*, Berlin, Germany, Sept. 2007.
- [6] F. X. Kärtner, R. Amataya, M. Aranghini, H. Byun, J. Chen, M. Dahlem, N.A. DiLello, F. Gan, C. W. Holzwarth, J. L. Hoyt, E. P. Ippen, A. Khilo, J. Kim, A. Motamedi, J. S. Orcutt, M. Park, M. Perrott, M. A. Popović, R. J. Ram, H. I. Smith, G. R. Zhou, S. J. Spector, T. M. Lyszczarz, M. W. Geis, D. M. Lennon, J. U. Yoon, M. E. Grein, and R. T. Schuelein, "Photonic Analog to Digital Conversion with Electronic-Photonic Integrated Circuits", *SPIE Photonics West Conference*, San Jose, CA, January 2008.
- [7] C. W. Holzwarth, R. Amatya, M. Dahlem, A. Khilo, F. X. Kärtner, E. P. Ippen, R. J. Ram, and H. I. Smith, "Fabrication Strategies for Filter Banks based on Microring Resonators," *J. Vac. Sci. & Technol. B*, vol. 26, pp 2164-2167 (2008).
- [8] M. A. Popović, T. Barwicz, E. P. Ippen and F. X. Kärtner, "Global Design Rules for Silicon Microphotonic Waveguides: Sensitivity, Polarization and Resonance Tunability," CTuCC1, *Conference on Lasers and Electro Optics (CLEO)*, Long Beach, CA, May 2006.
- [9] M. A. Popović, T. Barwicz, F. Gan, M. S. Dahlem, C. W. Holzwarth, P. T. Rakich, H. I. Smith, E. P. Ippen, and F. X. Kärtner, "Transparent wavelength switching of resonant filters," paper CPDA2, *Conference on Lasers and Electro-Optics (CLEO)*, Baltimore, MD, May 2007.
- [10] C. W. Holzwarth, T. Barwicz, and H. I. Smith, "Optimization of Hydrogen Silsesquioxane for Photonic Applications," *J. Vac. Sci. & Technol. B*, vol. 25, pp. 2658-2661 (2007).

Frequency Swept Lasers

Frequency Swept Lasers and Fourier Domain Mode Locking (FDML)

Sponsors

National Institutes of Health – R01-CA075289-12 and R01-EY11289-24

National Science Foundation – BES-0119494 and ECS-0900901

Air Force Office of Scientific Research – FA9550-07-1-0014 and FA9550-07-1-0101

Natural Sciences and Engineering Research Council of Canada (NSERC Canada) – CGS D2-331643-2006

National Science Council of Taiwan

Center for Integration of Medicine and Innovation Technology (CIMIT)

Project Staff

Dr. Desmond C. Adler, Dr. Vivek J. Srinivasan, Dr. Chao Zhou, Dr. Yueli Chen, Tsung-Han Tsai, Prof. James G. Fujimoto

1. Frequency-Swept Lasers and Fourier Domain Mode Locking (FDML)

Frequency swept lasers are a key technology for many applications including biomedical imaging using optical coherence tomography (OCT). Our group has recently developed a new approach for high speed frequency swept lasers, known as Fourier domain modelocking (FDML). This new laser technology enabled OCT imaging with higher acquisition speeds, better phase stability and greater imaging sensitivity [1-12]. OCT imaging using swept lasers is called “swept source / Fourier domain OCT” or “optical frequency domain imaging (OFDI)”. The measurement concept is similar to optical frequency domain reflectometry (OFDR), although the requirements for the laser are more demanding for OCT applications. Swept source / Fourier domain OCT imaging and the experimental imaging setup are described in more detail in the chapter on Laser Medicine and Biomedical Imaging. In this section, we will discuss progress on laser technology development for swept source / Fourier domain OCT.

1.1 Principle of Fourier Domain Mode Locking

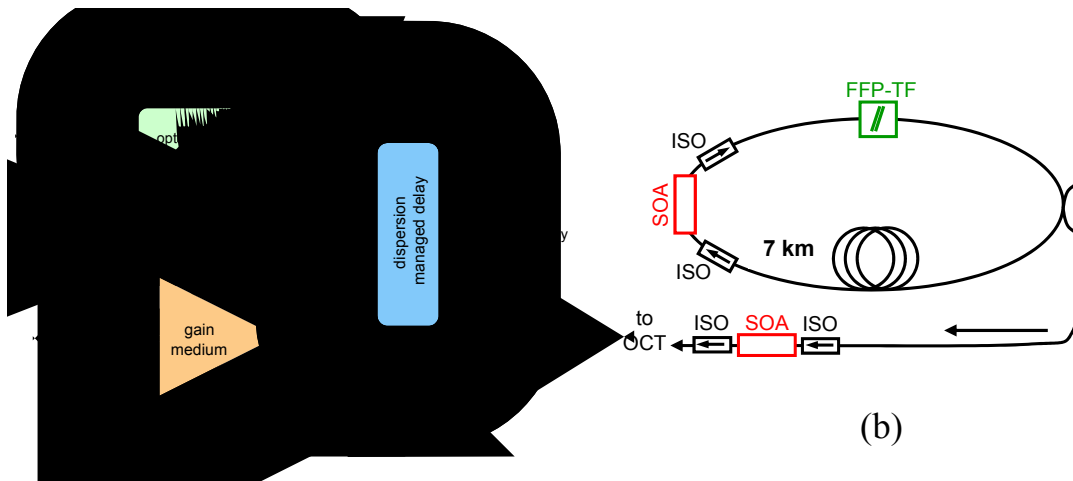


Figure 1. (a) Operation of Fourier domain modelocked (FDML) laser – the entire swept frequency optical waveform is stored within the cavity. (b) Experimental setup of FDML laser.

Standard frequency swept lasers consist of a broadband gain medium with a tunable optical bandpass filter in the cavity. The tunable filter is swept so that the transmission frequency varies in time and sufficient time is needed to allow lasing in the transmission bandwidth to build up from spontaneous emission inside the cavity. This limits the maximum tuning rate of the laser and also

results in lower power, broader instantaneous linewidth or shorter instantaneous coherence length when the laser is rapidly tuned. To overcome many of the limitation of conventional swept lasers, we developed a new technique known as Fourier domain mode locking (FDML)[13]. An FDML laser uses a cavity with a long fiber delay line and a fiber Fabry-Perot tunable filter (FFP-TF) whose sweep rate is synchronized with the round-trip time of light inside the cavity, or at a harmonic (Figure 1 (a)). The long fiber delay line stores the entire frequency sweep inside the laser and the different frequencies in the sweep return to the Fabry-Perot tunable filter at the time when the filter is tuned to transmit them. The laser generates a sequence of optical frequency sweeps at the cavity repetition rate.

Standard mode-locked lasers have longitudinal modes locked with constant phase, which corresponds to the generation of a train of short pulses at a repetition rate equal to the cavity round-trip time. Fourier domain mode-locked lasers have modes locked with a different phase relationship. The laser output is not a train of short pulses but instead is a train of frequency sweeps or highly chirped, very long pulses.

Figure 1 (b) shows an example schematic diagram of an FDML laser. The laser is based on a fiber-ring geometry with a semiconductor optical amplifier as a gain medium and a fiber Fabry-Perot filter as the tunable, narrowband optical bandpass filter. The FDML laser can operate at much higher sweep speeds than standard lasers, without degradation of output power or sweep bandwidth [7].

1.2 Performance of FDML Lasers

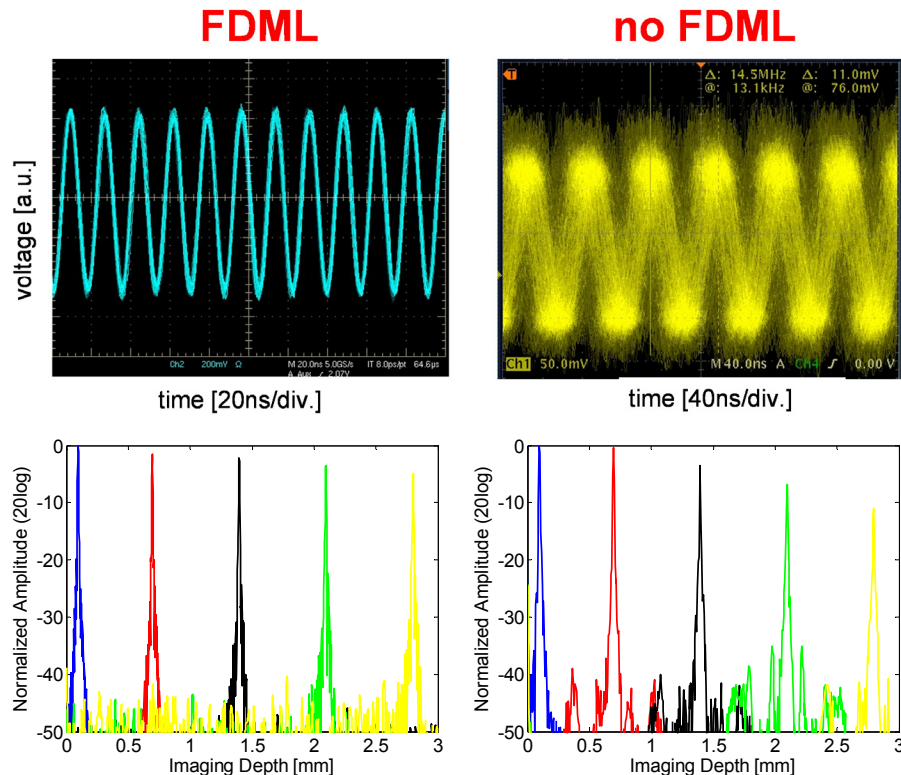


Figure 2: FDML lasers provide improved stability compared to conventional wavelength-swept lasers, resulting in a narrower instantaneous linewidth and larger ranging depth. Top: time-lapse view of interference fringes from a Mach-Zehnder interferometer acquired with an FDML (left) and conventional swept laser (right). Bottom: OCT point spread functions versus ranging depth for an FDML (left) and conventional swept laser (right).

Since FDML lasers operate in a quasi-stationary regime, because the swept waveform is circulated within the cavity, they are inherently less noisy and thus have higher signal to noise ratio (SNR) than conventional swept lasers. Figure 2 (top) shows the RF interferometric fringe traces produced by an asymmetric Mach-Zhender interferometer when an FDML and a conventional swept laser are used as the light source. Figure 2 (bottom) shows examples of measured point spread functions from an OCT system. Due to the narrow instantaneous linewidth of the FDML laser, the OCT point spread functions roll off more slowly with imaging depth than the conventional swept laser case. Imaging depth of up to 7 mm are possible using FDML lasers, whereas a considerable drop in sensitivity is observed over only 3 mm with the conventional swept laser. From the roll off of the point spread functions, a linewidth of 0.06 nm can be calculated for the FDML laser. This is much narrower than the filter bandwidth of 0.25 nm, and underlines the fact that in FDML the instantaneous linewidth is decoupled from the filter width. Much broader spectral filters can therefore be applied, reducing component costs and losses in the cavity. By integrating the frequency comb technology in the laser cavity, the instantaneous linewidth of the laser can be much narrower and can achieve better sensitivity when imaging deeper region, which is discussed in below.

2. Buffered FDML for Ultrahigh Speed Operation

To achieve high sweep rate fiber Fabry-Perot filters are driven sinusoidally and produce an alternating series of forward and backward frequency sweeps (bidirectional sweeping). However, unidirectional and more linear frequency sweeps are often preferred in order to improve performance at very high sweep speeds and reduce data processing requirements. Our group demonstrated a “buffered FDML” laser which provides unidirectional sweep [14] and also demonstrated a FDML laser with double buffering stages with sweep rate of 240 kHz, as shown in Fig. 3 [15, 16]. In this configuration, two or more output couplers (Fig. 3 (a)) are placed inside the cavity to generate time delayed copies of the optical waveform inside the cavity. These copies are then combined externally. Afterwards, the copies are routed to an external buffering stage consisting of an unbalanced Mach-Zehnder interferometer that provides another time delay. In the external stage, two additional copies of the cavity output are created. Two copies are time-shifted and all four copies are recombined in a final fiber-optic coupler. An oscilloscope screen capture of the laser output is shown in Fig. 3 (b).

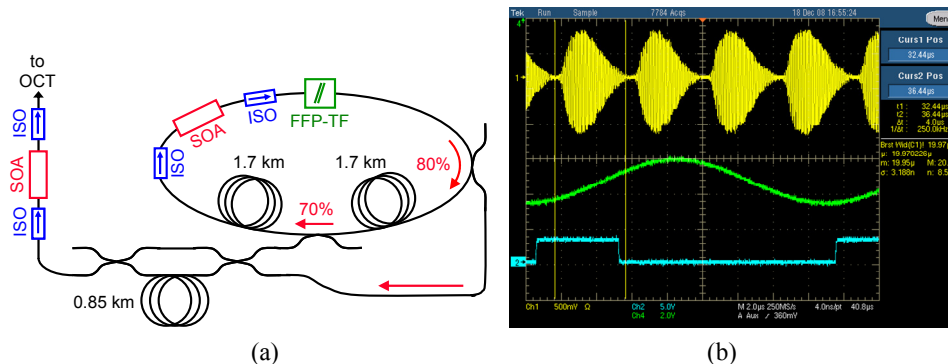


Figure 3. (a) Setup of double-buffered FDML laser with sweep rate of 240 kHz. (b) Screen capture of interference fringes and drive waves for the double-buffered FDML laser. Yellow: interference signal with 240 kHz repetition rate; Green: FFP-TF drive waveform; Blue: SOA modulation signal.

The time-averaged output spectrum of the double-buffered buffered FDML laser is shown in Fig. 4 (a). The total tuning range is 178 nm and the full width at half maximum (FWHM) is 117 nm. The average output power is 70 mW with a duty cycle of 91%. OCT point spread functions (PSF's) measured at increasing ranging depths are shown in Fig. 4(b). The sensitivity decreases by 5 dB at a ranging depth of 2 mm in air and by 23 dB at a ranging depth of 6 mm. This laser design achieves very high sweep repetition rates which enable very high OCT imaging speeds.

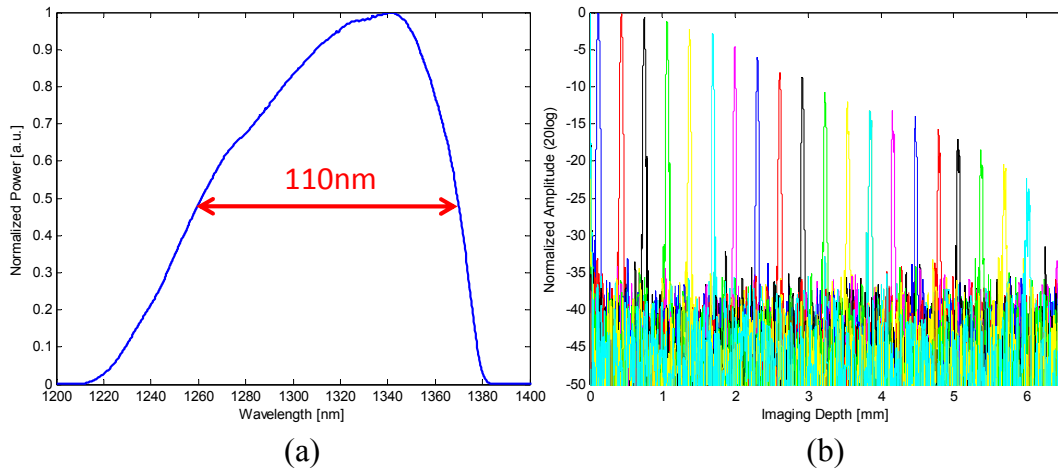


Figure 4. (a) Integrated output spectrum for double-buffered FDML laser, with a tuning range of 180 nm and a full-width-half-maximum bandwidth of 110 nm. (b) OCT point spread functions measured at increasing ranging depths.

3. FDML Operation with a Dispersive Cavity

To date, most of FDML lasers demonstrated were operated at 1310 nm because the chromatic dispersion in SMF-28 single-mode fiber is near zero. Wavelength-dependent variations in fiber birefringence are also low at 1310 nm and are negligible when the cavity length is shorter than 4 km. This wavelength region is also well suited for OCT applications in highly scattering media, as it represents a good compromise between water absorption and scattering in most biological tissues.

However, many future applications would benefit from other wavelength ranges. For ophthalmic imaging, where increased water absorption plays a key role, a swept source covering the transmission window of water between 1000 nm and 1100 nm is highly desirable [17, 18]. In this wavelength range, the long cavity of FDML laser has significant drawbacks that limit the tuning range of the laser. Chromaticity in the birefringence properties of the fiber makes it impossible to linearly polarize the entire sweep prior to entering the intra-cavity SOA to make the use of the optimal amplification. At 1060 nm, additional issues arise due to chromatic dispersion. Our group demonstrated 1060 nm FDML laser with sigma-ring configuration which utilizes a fiberoptic Faraday mirror (FM) to cancel out birefringence effects in the fiber cavity [19]. Partial dispersion compensation was also obtained in the FDML laser by introducing a Mach-Zehnder interferometer into the cavity to generate a time-multiplexing which provides two possible paths for photons traveling in the cavity [19]. Since the chromatic dispersion causes the light with different wavelength traveling with different speed, for a given sweep rate, a path with a different roundtrip length will have a different synchronized wavelength due to the chromatic dispersion. Therefore, this method can increase the tuning range of FDML laser, which was originally limited by the chromatic dispersion.

Figure 5 (a) shows a schematic of the FDML laser used for this study. A fiber optic Fabry-Perot tunable filter (FFP-TF) with a linewidth of 0.08 nm is used to filter the light propagating in the cavity. A semiconductor optical amplifier is used as the gain element. An 825 m length of HI1060 fiber is used to set the cavity round trip time. The fiber is on a spool and the entire laser can be made compact. The filter is tuned at the round-trip frequency, which is approximately 124.5 kHz. The SOA is modulated off during the forward (short to long wavelength) sweep to achieve a unidirectional sweep, and an extra-cavity unbalanced Mach-Zehnder is used to double the repetition rate [14]. Using this novel laser scheme, we have demonstrated ophthalmic OCT imaging with 8 μm axial resolution, 91 dB sensitivity, with an incident power of 1.2 mW. As shown in Fig. 5 (b), the 3 dB FWHM bandwidth of the laser is

about 68 nm, compared favorably to the 38 nm bandwidth in a FDML system [20] without polarization and dispersion management.

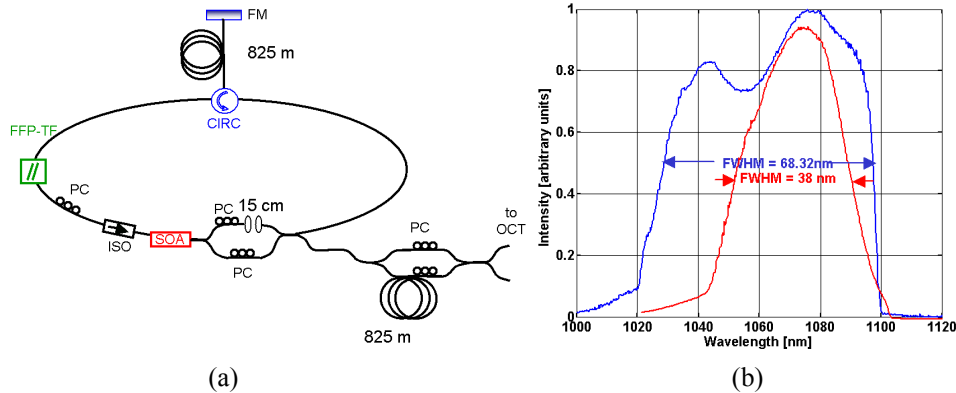


Figure 5. (a) Schematic for a 1060 nm “sigma ring” FDML laser with unbalanced intracavity Mach-Zehnder component for dispersion compensation. The laser also has an external buffering Mach-Zehnder stage to multiply the sweep rate to 249 kHz. (b) Average integrated output spectrum. The blue curve shows spectrum from this dispersion compensated laser scheme where a 68 nm bandwidth and 8 μm imaging resolution in the eye has been obtained. The red curve is from a regular FDML cavity without dispersion compensation and has a 38 nm bandwidth and a resolution of 13.7 μm in the eye.

4. Frequency Comb Swept Lasers

Our group has demonstrated frequency comb (FC) lasers, a new type of swept laser incorporating a fixed narrowband frequency comb fiber Fabry-Perot (FFP-FC) filter inside the cavity of conventional swept lasers and FDML lasers. FC swept lasers generate a sweep of discrete steps in frequency, rather than a continuous sweep. The extremely narrow bandwidth of the frequency steps generated by FC lasers improves the sensitivity roll off in OCT compared to conventional swept source and FDML lasers, enabling imaging over a longer depth range. The comb frequencies are equally separated in k-space, providing a clock signal which can be used to trigger the OCT interference fringe acquisition. This self-clocking method outperforms standard frequency calibration methods using reference Mach-Zehnder interferometer signals.

4.1 Concept of FC generation

In an FC laser, a fixed frequency comb filter (FFP-FC) with small free spectral range and narrow transmission bandwidth is used in the cavity in addition to a tunable filter (FFP-TF). The transmission function of the fixed frequency comb filter is defined as:

$$T = \frac{(1-R)^2}{1-2R \cdot \cos(2k \cdot L) + R^2}$$

Where R is the reflection coefficient, L is the cavity length in the Fabry-Perot resonator and k is the wavevector of the incident light. This filter thus provides a series of transmission peaks with an equal frequency spacing of $\Delta f = c/2nL$, also known as the free spectral range (FSR). However it is important to note that if the material n in the Fabry-Perot resonator has dispersion, the transmission resonances will no longer be uniformly spaced. Figure 6 shows the operating principle of FC lasers. During operation, the fixed frequency comb filter is continuously tuned across the sweep range and frequency components which pass through both the tunable filter and fixed frequency comb filter can be amplified by the gain medium, while other frequency components are suppressed. The laser operates at frequencies given by the product of the transmissions of these two cascaded filters. As the tunable filter is swept in time, the laser generates a series of fixed frequency steps with varying amplitudes. If the bandwidth of the tunable filter is less than the FSR of the fixed frequency comb filter, the laser will generate only a

single frequency at a time and the intensity output will be strongly modulated. If the bandwidth of the tunable filter is comparable to the FSR of fixed frequency comb filter, then the laser can operate in a superposition of fixed frequency comb filter frequencies and is partially modulated in intensity (Fig. 6 bottom left).

The instantaneous linewidth of the FC laser is determined by the bandwidth of fixed frequency comb filter, which is much narrower than the tunable filter bandwidth. This produces a longer coherence length output, yielding less sensitivity roll-off over large imaging depths compared to conventional swept lasers. Moreover, since the peaks in the intensity modulation are equally spaced in frequency, they can be used as a clock signal to sample the OCT interference signal. This results in a calibrated OCT interference signal which is equally sampled in k-space and can be directly Fourier transformed to obtain axial scan information. The OCT interferometric signal obtained using an FC laser can be considered as a discrete version of interferometric signal obtained using a standard FDML laser, and the discrete spacing is determined by the FSR of FFP-FC because it determines the frequency comb spacing of the laser.

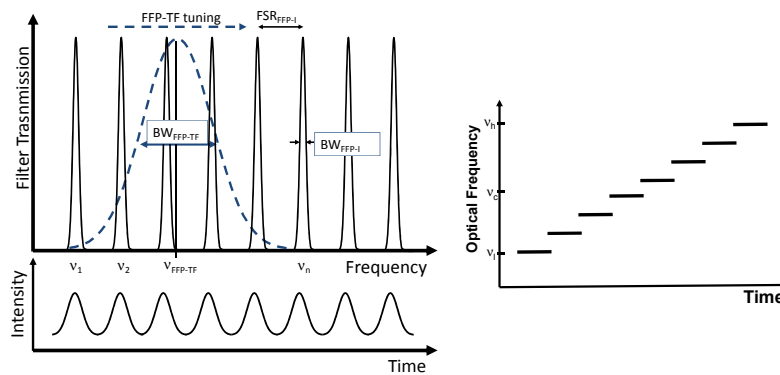


Figure 6: Frequency comb generation concept.

Figure 7 (a) shows a schematic diagram of the FC swept laser. The laser is based on a ring resonator geometry with a semiconductor optical amplifier (SOA) as the gain medium, a tunable filter (FFP-TF), and a fixed frequency filter (FFP-FC) in a cavity with 15 m physical path length. The laser output is amplified with a second SOA outside the cavity which serves as a booster amplifier. The ratio of the bandwidth of the tunable filter to the FSR of the fixed frequency filter is 0.67. The FSR of fixed frequency comb filter is ~25 GHz, corresponding to a maximum imaging depth of 3 mm. A sinusoidal waveform of 1 kHz was used to drive the tunable filter. Figure 7 (b) shows a schematic diagram of the FC-FDML laser, using the same tunable and fixed frequency filters. The tunable filter is driven with a sinusoidal waveform at 60 kHz. A single buffered geometry [14] was used to double the frequency sweep. To compare performance, the frequency comb filter FFP-FC was removed from the cavities in Figs. 7 (a) and (b) to obtain conventional swept source and FDML laser operation.

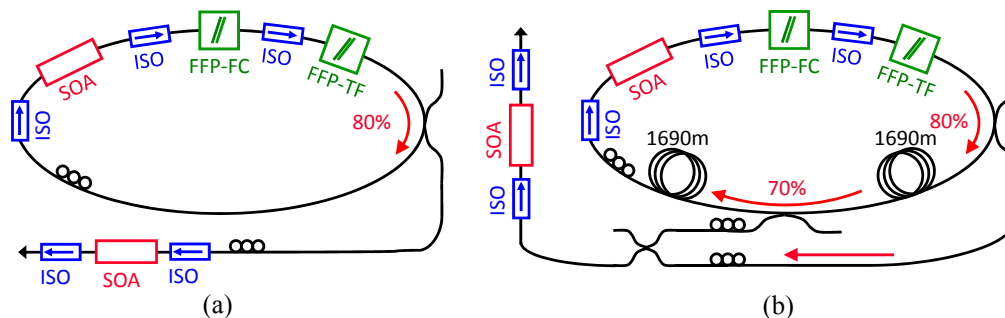


Figure 7: Schematic diagrams of the frequency comb (FC) swept laser (a) and frequency comb Fourier domain mode-locked (FDML) laser (b).

4.2 Performance of FC Swept Lasers

Figure 8 shows the output spectra of the FC swept laser. The total tuning range of the spectrum is 130 nm, with full width half maximum (FWHM) of 70 nm. The zoomed view in Fig. 8 (b) shows the ~ 0.15 nm spacing between each frequency step, corresponding to the FSR of the frequency comb filter. The background underneath the frequency modulation is produced by the amplified spontaneous emission (ASE) of the booster SOA.

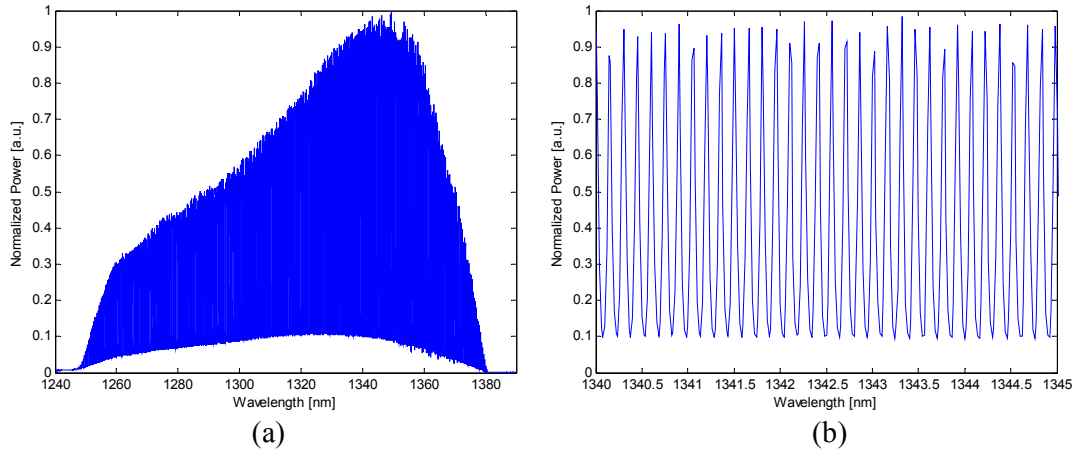


Figure 8: (a) Output spectrum of the FC swept laser. (b) Zoomed in view from 1340nm to 1345 nm.

Figure 9 compares transient intensity outputs of the conventional swept source, FDML and FC swept lasers. The zoomed view in Fig. 9 (c) and (f) is similar to that predicted by Fig. 6. The frequency comb filter in the cavity generates a modulated intensity output. Each peak in the modulation represents an individual frequency step. The time spacing between each peak in the intensity is determined by the instantaneous tuning speed of the tunable filter. The time between peaks in central part of the frequency sweep is smaller than that in the edge of the sweep because the tunable filter is driven sinusoidally. Figure 10 shows an example OCT interferometric signal using the FC and FC-FDML lasers at a delay of 0.7 mm. The modulation in the laser output intensity can be seen superposed on the OCT interferometric signals. Each peak in the modulation represents an individual frequency step, indicating that the interference traces can be precisely calibrated to frequency (linear in k -space) if they are sampled at the peaks of the modulations.

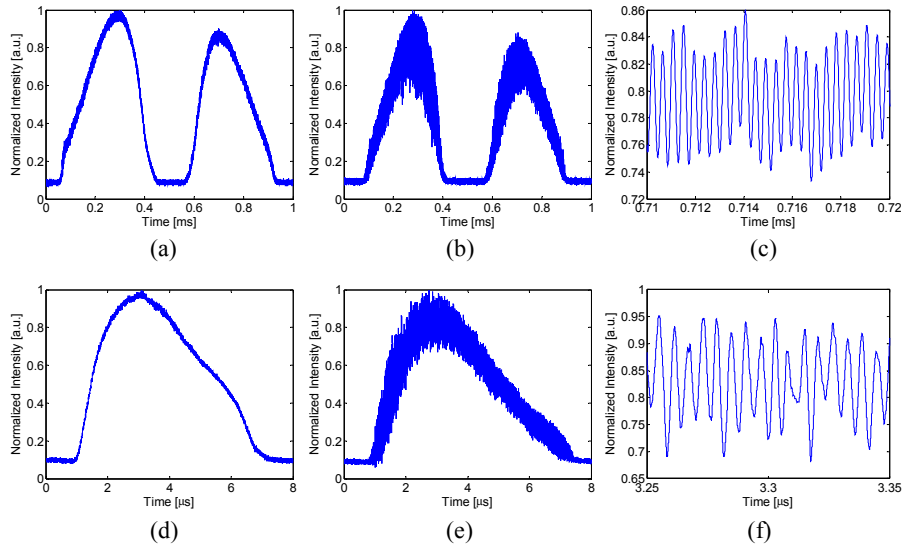


Figure 9: Transient intensity output traces of different lasers: (a) conventional swept laser; (b) FC swept laser; (c) zoomed view from 0.71 μs to 0.72 μs of (b); (d) FDML laser; (e) FC-FDML laser; (f) zoom-in view from 3.25 μs to 3.35 μs of (e).

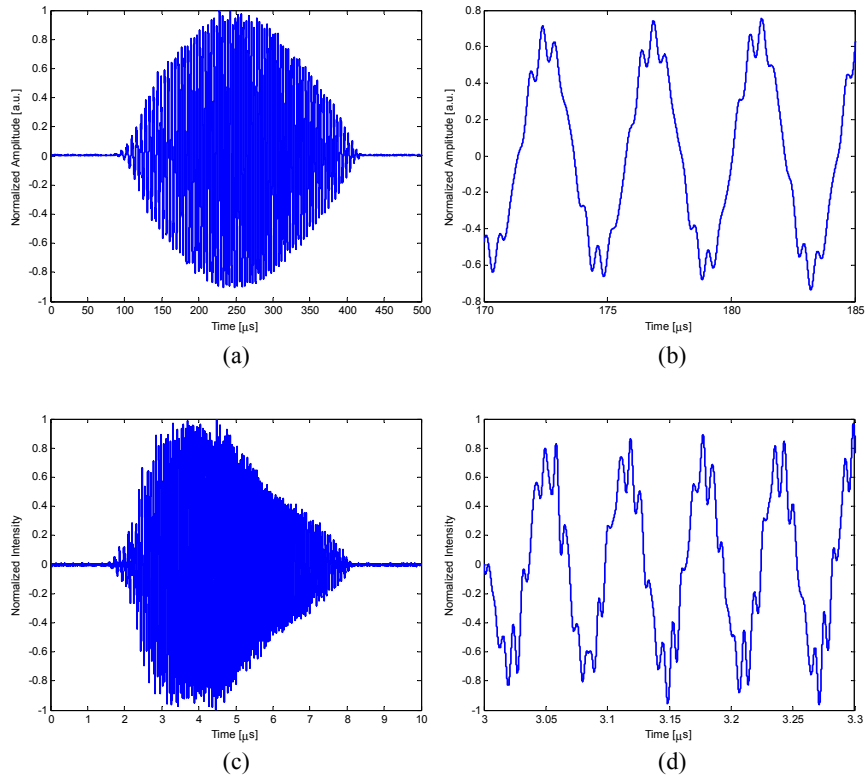


Figure 10: OCT interferometric traces at 0.7 mm imaging depth using a (a) FC swept laser and (c) FC-FDML laser. (b) and (d) are the zoomed views of (a) from 170 μs to 185 μs and (c) from 3 μs and 3.3 μs respectively.

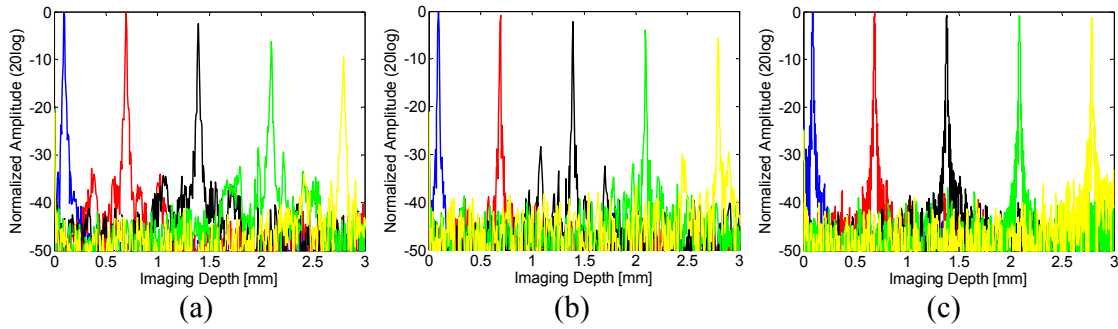


Figure 11: OCT point spread functions comparison from 0.1 mm to 2.8 mm imaging depth: (a) conventional swept laser; (b) FC swept laser with MZI calibration; (c) FC swept laser with self-clocking calibration.

Figure 11 shows an example of the sensitivity roll off comparison of a conventional swept laser and a FC laser with the same operation parameters. The FC laser shows less sensitivity roll off compared with the conventional swept laser, indicating the instantaneous coherence length of the frequency steps in the FC laser are longer. Furthermore, the self-clocking method calibrates the interference data to linear k-space more accurately compared to the MZI recalibration method, achieving much less sensitivity roll off over the 2.8 mm imaging depth [21]. The same comparison was also performed between a FDML and FC-FDML laser. Figure 12 shows the sensitivity roll off over 2.8 mm depth for an FDML laser, a FC-FDML laser with MZI recalibration, and a FC-FDML laser with self-clocking. The sensitivity using the FDML laser rolls off by -5dB which shows that the instantaneous linewidth of FDML laser is narrower than conventional swept laser. Using MZI recalibration, the sensitivity roll off of FC-FDML laser is -3 dB, which is slightly improved compared to the standard FDML laser. However, using the self-clocking method, a sensitivity roll off of only -1.3 dB can be achieved using the FC-FDML laser. This result is consistent with previous section and shows that FC lasers have superior linewidth and coherence length performance compared with standard swept lasers or FDML lasers [21]. Table 1 summarizes the sensitivity roll offs for all of the lasers [21].

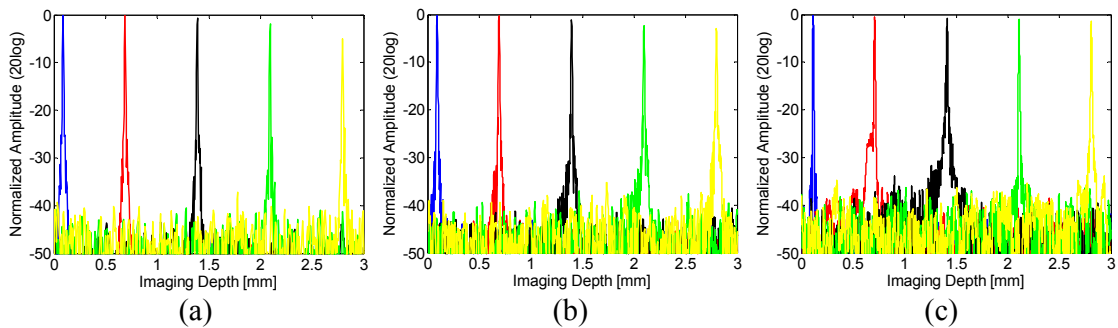


Figure 12: OCT point spread functions comparison from 0.1 mm to 2.8 mm imaging depth: (a) FDML laser; (b) FC-FDML laser with MZI calibration; (c) FC-FDML laser with self-clocking calibration.

Laser	No FC filter	FC + MZI calibration	FC + Self-clocking
Swept laser (1 kHz)	-10 dB	-5 dB	-1.2 dB
FDML laser (120 kHz)	-5 dB	-3 dB	-1.3 dB

Table 1: Summary of sensitivity roll off at 2.8mm imaging depth of different lasers.

4.3 Extended depth ranging

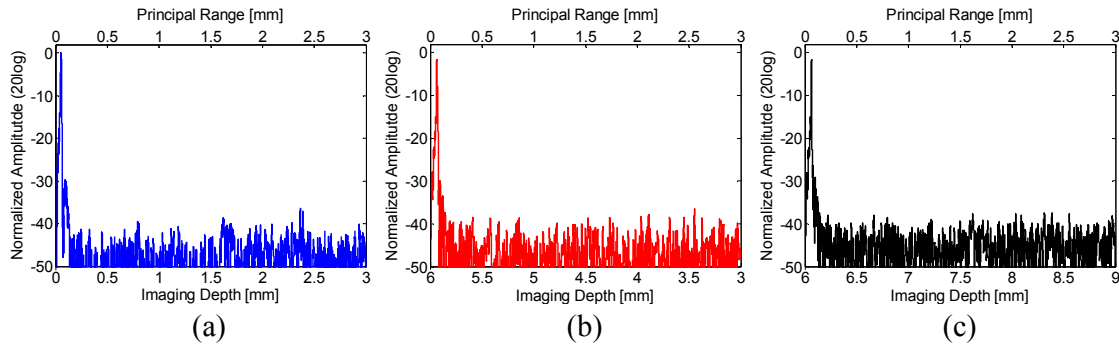


Figure 13: OCT point spread functions at imaging depth deeper than the principal imaging range. (a) Reflection is at 0.06 mm depth. (b) Reflection is at 5.94 mm depth. (c) Reflection is at 6.06 mm. Each amplitude is normalized by the peak value in (a).

Aliasing occurs if the OCT signal is outside the principal measurement range set by the frequency comb filter. Figure 13 (a) shows the point spread function (PSF) when reflection is at 0.06 mm depth. Figure 13 (b) shows a reflection from a depth of 5.94 mm, which appears in the measurement as if it is at 0.06 mm delay. Reflections which are at position z between 3 mm to 6 mm range appear in the measurement as if they are between 3 mm to 0 mm, at a position $(3 \text{ mm} - z)$, mirrored about the 3 mm position. When the reflection at the edge of the principal measurement range, 3 mm in this case, the corresponding PSF and its mirror PSF would overlap and it would not be possible to distinguish if the reflection were from the edge of the imaging range or near zero delay. Figure 13 (c) shows the PSF when the reflection is at 6.06 mm. Because of the FSR of the fixed frequency comb filter, the signal from a reflection at 6.06 mm appears as if it is at 0.06 mm depth because the measurement range repeats every 6 mm. Reflections which are at a position z between 6 mm to 9 mm range appear as if they are between 0 mm and 3 mm, at a position $(z - 6 \text{ mm})$. Note that the sensitivity for the reflection at 6.06 mm delay is decreased by only -1.5 dB, demonstrating the narrow linewidth of the frequency steps generated by the FC laser. Although the aliasing occurs at deeper depths, this implies that it is possible to see signals at very long delays with very little loss of sensitivity. This property could be very useful for applications such as profilometry, where the measured signals can be easily de-aliased.

In conclusion, FC swept lasers can provide narrower linewidth for both conventional swept lasers and FDML lasers. The characteristic of discrete frequency steps and intensity modulation can precisely calibrate the fringe signal into linear k -space using self-clocking method. Using frequency comb operation with self-clocking, the sensitivity roll off at 2.8 mm delay is improved from -10 dB to -1.2 dB for the swept laser and from -5 dB to -1.3 dB for the FDML laser. Since the frequency steps in the laser output are precisely determined by the frequency comb filter, the use of frequency combs should improve the performance of SS- OCT for phase measurement and Doppler applications.

References

- [1] D. Huang, E. A. Swanson, C. P. Lin, J. S. Schuman, W. G. Stinson, W. Chang, M. R. Hee, T. Flotte, K. Gregory, C. A. Puliafito, and J. G. Fujimoto, "Optical Coherence Tomography," *Science*, vol. 254, pp. 1178-1181, Nov 22 1991.
- [2] S. R. Chinn, E. A. Swanson, and J. G. Fujimoto, "Optical coherence tomography using a frequency-tunable optical source," *Optics Letters*, vol. 22, pp. 340-342, Mar 1 1997.
- [3] M. A. Choma, K. Hsu, and J. A. Izatt, "Swept source optical coherence tomography using an all-fiber 1300-nm ring laser source," *Journal of Biomedical Optics*, vol. 10, p. no. 044009 Jul-Aug 2005.

- [4] M. A. Choma, M. V. Sarunic, C. Yang, and J. Izatt, "Sensitivity advantage of swept source and Fourier domain optical coherence tomography," *Optics Express*, vol. 11, pp. 2183-2189, 2003.
- [5] A. F. Fercher, C. K. Hitzenberger, G. Kamp, and S. Y. Elzaiat, "Measurement of Intraocular Distances by Backscattering Spectral Interferometry," *Optics Communications*, vol. 117, pp. 43-48, MAY 15 1995.
- [6] B. Golubovic, B. E. Bouma, G. J. Tearney, and J. G. Fujimoto, "Optical frequency-domain reflectometry using rapid wavelength tuning of a Cr⁴⁺:forsterite laser," *Optics Letters*, vol. 22, pp. 1704-1706, Nov 15 1997.
- [7] R. Huber, K. Taira, T. H. Ko, M. Wojtkowski, V. Srinivasan, and J. G. Fujimoto, "High-speed, amplified, frequency swept laser at 20 kHz sweep rates for OCT imaging," in *Conference on Lasers and Electro-Optics/Quantum Electronics and Laser Science and Photonic Applications, Systems and Technologies 2005*, Baltimore, 2005, p. JThE33.
- [8] R. Huber, M. Wojtkowski, J. G. Fujimoto, J. Y. Jiang, and A. E. Cable, "Three-dimensional and C-mode OCT imaging with a compact, frequency swept laser source at 1300 nm," *Optics Express*, vol. 13, pp. 10523-10538, Dec 22 2005.
- [9] F. Lexer, C. K. Hitzenberger, A. F. Fercher, and M. Kulhavy, "Wavelength-tuning interferometry of intraocular distances," *Applied Optics*, vol. 36, pp. 6548-6553, Sep 1 1997.
- [10] Y. Yasuno, V. Madjarova, S. Makita, M. Akiba, A. Morosawa, C. Chong, T. Sakai, K. Chan, M. Itoh, and T. Yatagai, "Three-dimensional and high-speed swept-source optical coherence tomography for in vivo investigation of human anterior eye segments," *Optics Express*, vol. 13, pp. 10652-10664, 2005.
- [11] S. H. Yun, C. Boudoux, G. J. Tearney, and B. E. Bouma, "High-speed wavelength-swept semiconductor laser with a polygon-scanner-based wavelength filter," *Optics Letters*, vol. 28, pp. 1981-1983, Oct 15 2003.
- [12] J. Zhang and Z. P. Chen, "In vivo blood flow imaging by a swept laser source based Fourier domain optical Doppler tomography," *Optics Express*, vol. 13, pp. 7449-7457, Sep 19 2005.
- [13] R. Huber, M. Wojtkowski, and J. G. Fujimoto, "Fourier Domain Mode Locking (FDML): A new laser operating regime and applications for optical coherence tomography," *Optics Express*, vol. 14, pp. 3225-3237, Apr 17 2006.
- [14] R. Huber, D. C. Adler, and J. G. Fujimoto, "Buffered Fourier domain mode locking: unidirectional swept laser sources for optical coherence tomography imaging at 370,000 lines/s," *Opt. Lett.*, vol. 31, pp. 2975-2977, 2006.
- [15] D. C. Adler, Y. Chen, R. Huber, J. Schmitt, J. Connolly, and J. G. Fujimoto, "Three-dimensional endomicroscopy using optical coherence tomography," *Nature Photonics*, vol. 1, pp. 709-716, Dec 2007.
- [16] D. C. Adler, S.-W. Huang, R. Huber, and J. G. Fujimoto, "Photothermal detection of gold nanoparticles using phase-sensitive optical coherence tomography," *Opt. Express*, vol. 16, pp. 4376-4393, 2008.
- [17] E. C. W. Lee, J. F. de Boer, M. Mujat, H. Lim, and S. H. Yun, "In vivo optical frequency domain imaging of human retina and choroid," *Optics Express*, vol. 14, pp. 4403-4411, May 15 2006.
- [18] B. Povazay, K. Bizheva, B. Hermann, A. Unterhuber, H. Sattmann, A. F. Fercher, W. Drexler, C. Schubert, P. K. Ahnelt, M. Mei, R. Holzwarth, W. J. Wadsworth, J. C. Knight, and P. S. Russel, "Enhanced visualization of choroidal vessels using ultrahigh resolution ophthalmic OCT at 1050 nm," *Optics Express*, vol. 11, pp. 1980-1986, Aug 25 2003.
- [19] V. J. Srinivasan, D. C. Adler, Y. Chen, I. Gorczynska, R. Huber, J. S. Duker, J. S. Schuman, and J. G. Fujimoto, "Ultrahigh-Speed Optical Coherence Tomography for Three-Dimensional and En Face Imaging of the Retina and Optic Nerve Head." vol. 49, 2008, pp. 5103-5110.
- [20] R. Huber, D. C. Adler, V. J. Srinivasan, and J. G. Fujimoto, "Fourier domain mode locking at 1050 nm for ultra-high-speed optical coherence tomography of the human retina at 236,000 axial scans per second," *Opt. Lett.*, vol. 32, pp. 2049-2051, 2007.
- [21] T.-H. Tsai, C. Zhou, D. C. Adler, and J. G. Fujimoto, "Frequency Comb Swept Lasers," *Submitted to Optics Express*, 2009.

Journal Articles

1. J. Chen, J. W. Sickler, T. Wilken, P. Fendel, R. Holzwarth, T. W. Hänsch, E. P. Ippen and F. X. Kärtner, "Generation of Low Jitter Femtosecond Pulse Trains with 1~2 GHz repetition rate via external Fabry-Perot Cavities, *Opt. Lett.* 33:(9), pp.959-961 (2008).
2. H. M. Crespo, J. R. Birge, E. L. Falcao-Filho, M. Y. Sander, A. Benedick, and F. X. Kärtner, "Non-intrusive phase-stabilization of sub-two-cycle pulses from a prismless octave-spanning Ti:sapphire Laser," *Opt. Lett.* 33:(8), 833-835 (2008).
3. G.-R. Zhou, M. W. Geis, S. J. Spector, F. Gan, M. E. Grein, R. T. Schulein, J. S. Orcutt, J. U. Yoon, D. M. Lennon, E. P. Ippen, Th. M. Lyszczarz and F. X. Kärtner, "Effect of Carrier Lifetime on Forward-biased Silicon Mach-Zehnder Modulators," *Opt. Express* 16:(8), 5218-5226 (2008).
4. U. Demirbas, A. Sennaroglu, A. Benedick, A. Siddiqui, F. X. Kärtner, and J. G. Fujimoto, "Highly efficient, low-cost femtosecond Cr³⁺:LiCAF laser pumped by single-mode diodes," *Opt. Lett.* 33:(6), pp.590-592 (2008).
5. H. M. Crespo, J. R. Birge, M. Y. Sander, E. L. Falcao-Filho, A. Benedick, and F. X. Kärtner, "Phase-stabilization of sub-two-cycle pulses from prismless octave-spanning Ti:sapphire Lasers," *JOSA B* 25:(7), pp. B147-B154 (2008).
6. S. J. Spector, M. W. Geis, G.-R.Zhou, M. E. Grein, R. T. Schulein, F. Gan, M. Popović, J. U. Yoon, D. M. Lennon, T. M. Lyszczarz, E. P. Ippen and F. X. Kärtner, "CMOS-Compatible Dual Output Silicon Modulators for Analog Signal Processing," Vol. 16, Issue 15, pp. 11027-1103 (2008).
7. J. Kim, J. A. Cox, J. J. Chen, and F. X. Kärtner, "Drift-free femtosecond timing synchronization of optical and microwave sources over long distances with 10⁻¹⁹ stability," *Nature Photonics* 2, 733 (2008).
8. C. E. Cramer, C-H. Li, A. Benedick, A. G. Glenday, D. Phillips, D. Sasselov, A. Szentgyorgyi, F. X. Kärtner and R. Walsworth, "Astro-Comb: Revolutionizing precision spectroscopy in astrophysics," *J. Mod. Opt.* submitted.
9. J. Kim, M. J. Park, M. H. Perrott, and F. X. Kärtner, "Photonic subsampling analog-to-digital conversion of microwave signals at 40-GHz with higher than 7-ENOB resolution," *Optics Express* 16:(21) pp.16509-16515 (2008).
10. K. H. Hong, A. Siddiqui, J. Moses, J. Gopinath, J. Hybl, F. O. Ilday, T.Y. Fan and F. X. Kaertner, "Generation of 287-W, 5.5-ps pulses at 78-MHz repetition rate from a cryogenically-cooled Yb:YAG amplifier seeded by a fiber chirped-pulse amplification system," *Optics Letters* 33:(21), pp.2473-2475 (2008).
11. H. Byun, D. Pudo, J. Chen, E. P. Ippen and F. X. Kärtner, "High repetition rate, 491 MHz, femtosecond fiber laser with low timing jitter," *Optics Letters* 33:(1)9, pp.2221-2223 (2008).
12. S. Rausch, Th. Binhammer, A. Harth, N. Meiser, R. Ell, F. X. Kärtner, and U. Morgner, "Controlled Waveforms on the Single-cycle Scale from a Femtosecond Oscillator," *Opt. Express* 16:(13), pp. 9739-9745 (2008).
13. L.-J. Chen, A. J. Benedick, J. R. Birge, M. Y. Sander and Franz X. Kärtner, "Octave-spanning, dual-output 2 GHz Ti:sapphire laser with a carrier-envelope beat note of >50dB," *Opt. Express* 16:(25), pp. 20699-20705 (2008)
14. U. Demirbas, A. Sennaroglu, F. X. Kärtner, and J. G. Fujimoto, "Comparative investigation of diode pumping for low-cost Cr³⁺:LiCAF lasers," to appear in *JOSA B*.
15. F. X. Kärtner, J.Kim, J. Chen and A. Khilo, "Photonic Analog-to-Digital Conversion with Femtosecond Lasers," *Frequenz* pp. 171-174, (2008).

16. M. Y. Sander, J. Birge, A. Benedick, H. Crespo and F. X. Kärtner, "Dynamics of Octave-Spanning Titanium: Sapphire Lasers," *Journal of the Optical Society of America, JOSA B* 26:(4) pp. 743-749 (2009).
17. U. Demirbas, A. Sennaroglu, F. X. Kärtner, and J. G. Fujimoto, "Generation of 15-nJ pulses from a highly efficient, low-cost multipass-cavity Cr³⁺:LiCAF laser," *Optics Letters* 34:(4), pp.497-499 (2009).
18. D. Pudo, H. Byun, J. Chen, J. Sickler, F. X. Kärtner, E. P. Ippen, "Scaling of passively mode-locked soliton erbium waveguide lasers based on slow saturable absorbers," *Opt. Express* 16:(23), pp.19221-19231 (2008).
19. C. W. Holzwarth, R. Amatya, M. Dahlem, A. Khilo, F. X. Kärtner, E. P. Ippen, R. J. Ram, and Henry I. Smith, "Fabrication strategies for filter banks based on microring resonators," *J. Vac. Sci. Technol. B* 26, 2164-2167, (2008).
20. J. R. Birge and F. X. Kärtner, "Measuring Sub-Two-Cycle Laser Pulses with Two-Dimensional Spectral Shearing Interferometry," *Laser Focus World*, March 2009, p. 61 (2009).
21. E. L. Falcão-Filho, V. M. Gkortsas, A. Gordon and F. X. Kärtner, "Analytic scaling of high harmonic generation conversion efficiency," *Opt. Express* 17:(13) pp. 11217-11229 (2009).
22. S. Rausch, Th. Binhammer, A. Harth, F. X. Kärtner, and U. Morgner, "Few-cycle Scale Femtosecond Field Synthesizer," *Opt. Express* 16:(22), pp.17410-17419 (2008).
23. J. Moses, C. Manzoni, S-W Huang, G.Cerullo, and F. X. Kärtner, "Temporal Optimization of Ultrabroadband High-Energy OPCPA," *Opt. Express* 17:(7), pp 5540-5555 (2009).
24. H. Byun, D. Pudo, J. Chen, S. Frolov, A. Hanjani, J. Shmlovich E. P. Ippen and F. X. Kärtner, "Integrated low-jitter 400 MHz femtosecond waveguide laser," *Photonics Technology Letters, IEEE*, 21:(12), pp.763-765 (2009).
25. J. Kim, F. X. Kärtner, "Attosecond Precision Ultrafast Photonics," to appear in *Laser & Photonics Review*, John Wiley, 2009.
26. J. Moses, S.-W. Huang, K.-H. Hong, O. D. Mücke, E. L. Falcao-Filho, A. Benedick, F. Ö. Ilday, A. Dergachev, J. A. Bolger, B. J. Eggleton, and F. X. Kärtner, "Highly stable ultrabroadband mid-infrared optical parametric chirped pulse amplifier optimized for superfluorescence suppression," *Opt. Lett.* 34, 1639-1641 (2009).
27. A. Benedick, D. Tyurikov, M. Gubin, R. Shewmon, I. Chuang, and F. X. Kärtner, "Compact, Ti:sapphire based methane-stabilized optical molecular frequency comb and clock," to appear in *Opt. Lett.*
28. A. H. Nejadmalayeri, F. N. C. Wong, T. D. Roberts, P. Battle, and F. X. Kärtner, "Guided wave optics in periodically poled KTP: quadratic nonlinearity and prospects of attosecond jitter characterization," to appear in *Optics Letters*
29. S. J. Spector, Ch. M. Sorace, M. W. Geis, M. E. Grein, J. U. Yoon, T. M. Lyszczarz, E. P. Ippen, and F. X. Kärtner, "Operation and Optimization of Silicon-Diode- Based Optical Modulators," to appear in *JSTQE*.
30. Ch. Y. Wang, L. Kuznetsova, V. M. Gkortsas, L. Diehl , F. X. Kärtner, M. A. Belkin, A. Belyanin, X. Li, D. Ham, H Schneider, P. Grant, C. Y. Song, S. Haffouz, Z. R. Wasilewski, H. C. Liu and Federico Capasso, "Mode-locked pulses from mid-infrared Quantum Cascade Lasers," submitted to *Opt. Express*.
31. U. Demirbas, K.-H. Hong, A. Sennaroglu, F. X. Kärtner, and J. G. Fujimoto, "A low-cost cavity-dumped Cr³⁺:LiSAF laser producing >100 nJ pulses," in preparation for *Opt. Letters*.
32. K.-H. Hong, Ch.-J. Lai, A. Siddiqui, J. Gopinath, T. Y. Fan, and F. X. Kärtner, "130-W picosecond green laser based on a frequency-doubled hybrid cryogenic Yb:YAG amplifier," submitted to *Opt. Express*.

33. W. S. Graves, W. Brown, F. X. Kaertner, and D. E. Moncton, "MIT Inverse Compton Source Concept," NIM

Conference Proceedings

1. H. Byun, J. Sickler, J. Morse, J. Chen, D. Pudo, E. P. Ippen, and F. X. Kärtner, "Femtosecond passively mode-locked fiber lasers using saturable Bragg reflectors", Paper THU11c.1, Ultrafast Phenomena Conference 2008, Stresa, Italy, June 2008.
2. M. Y. Sander, H. M. Crespo, J. R. Birge, and F. X. Kärtner, "Modeling of Octave-Spanning sub-two-cycle Titanium:sapphire Lasers: Simulation and Experiment, Paper THU11c.8, Ultrafast Phenomena Conference 2008, Stresa, Italy, June 2008.
3. U. Demirbas, A. Sennaroglu, F. X. Kärtner, and J. G. Fujimoto, "Highly Efficient, Low Cost, Diode-Pumped Femtosecond Cr³⁺:LiCAF Laser", Ultrafast Phenomena Conference 2008, Stresa, Italy, June 2008.
4. J. A. Cox, J. Kim, and F. X. Kärtner, "10-femtosecond Precision, Long-term Stable Timing Distribution Over Multiple Fiber Links," Ultrafast Phenomena Conference 2008, Stresa, Italy, June 2008.
5. J. Moses, C. Manzoni, S-W Huang, G. Cerullo, and F. X. Kärtner, "Temporal Optimization of Ultrabroadband Optical Parametric Chirped Pulse Amplification," Ultrafast Phenomena Conference 2008, Stresa, Italy, June 2008.
6. S. Rausch, Th. Binhammer, A. Harth, J. Kim, R. Ell, F. X. Kärtner, and U. Morgner, "Controlled Waveforms on the Single-cycle Scale from a Femtosecond Oscillator," Ultrafast Phenomena Conference 2008, Stresa, Italy, June 2008.
7. H. Byun, J. Sickler, J. Morse, J. Chen, D. Pudo, E. P. Ippen, F. X. Kärtner, "Femtosecond passively mode-locked fiber lasers using saturable Bragg reflectors," Paper THU11c.1, Ultrafast Phenomena Conference 2008, Stresa, Italy, June 2008.
8. J. Moses, O. D. Mücke, S.-W. Huang, A. Benedick, E. L. Falcão-Filho, K.-H. Hong, A. M. Siddiqui, J. R. Birge, F. Ö. Ilday and F. X. Kärtner, "Optimized 2-micron Optical Parametric Chirped Pulse Amplifier for High Harmonic Generation," Ultrafast Phenomena Conference 2008, Stresa, Italy, June 2008.
9. J. Chen, J. Sickler, H. Byun, E. P. Ippen, S. Jiang and F. X. Kärtner, "Fundamentally Mode-locked 3 GHz Femtosecond Erbium Fiber Laser," Postdeadline Paper, Ultrafast Phenomena Conference 2008, Stresa, Italy, June 2008.
10. P.T. Rakich and M.A. Popović, "Generalized Treatment of Optically Induced Forces and Potentials in Optomechanically Variable Photonic Circuits," Paper ITuC6, OSA Topical Meeting on Integrated Photonics and Nanophotonics Research and Applications (IPNRA), Boston, MA, July 15, 2008.
11. S.J. Spector, M.W. Geis, G.-R. Zhou, M.E. Grein, R.T. Schulein, F. Gan, M.A. Popović, J.U. Yoon, D.M. Lennon, E.P. Ippen, F.X. Kärtner and T.M. Lyszczarz, "CMOS-Compatible Wideband Silicon Modulator," Paper IMC3, OSA Topical Meeting on Integrated Photonics and Nanophotonics Research and Applications (IPNRA), Boston, MA, July 15, 2008.
12. Ch. Batten, A. Joshi, J. Orcutt, A. Khilo, B. Moss, Ch. Holzwarth, M. A. Popović, H. Li, H. Smith, J. Hoyt, F. Kärtner, R. Ram, V. Stojanović, K. Asanović, "Building Manycore Processor-to-DRAM Networks with Monolithic Silicon Photonics," Proceedings of the 2008 16th IEEE Symposium on High-Performance Interconnects, Stanford, CA, August 2008
13. H. Byun, J. Sickler, J. Morse, J. Chen, D. Pudo, E. P. Ippen, and F. X. Kärtner, "Integrated, low-jitter, 400 MHz femtosecond passively mode-locked waveguide laser", Annual Meeting of the IEEE Laser and Electro-Optics Society LEOS, Newport Beach, CA, 2008.
14. F. X. Kärtner, "High repetition rate octave spanning lasers and frequency combs," SIAM 2008, Rome, Italy, July 21-24, 2008.

15. F. X. Kärtner, J. Kim, J. Cox, and J.Chen, "Femtosecond Synchronization of Large Scale X-ray Free Electron Lasers," International Conference on Free Electron Lasers, FEL 2008, Postech, Korea, August 26-30, 2008.
16. F. X. Kärtner, J. Kim, J. Cox, and J.Chen, "Large Scale, Femtosecond Timing Distribution for X-ray Free Electron Lasers," ASIL 4, Gwangju, Korea, Nov. 1-4, 2008.
17. F. X. Kärtner, "Instabilities and Mode Locking in Quantum Cascade Lasers," IQCLSW, ETH Zurich, September 13-19, 2008
18. F. X. Kärtner, "Photonic Analog to Digital Conversion with Femtosecond Lasers," TU Munich, October 10, 2008.
19. C. W. Holzwarth, R. Amatya, M. Araghchini, J. Birge, H. Byun, J. Chen, M. Dahlem, N.A. DiLello, F. Gan, J. L. Hoyt, E. P. Ippen, F. X. Kärtner, A. Khilo, J. Kim, M. Kim, A. Motamedi, J. S. Orcutt, M. Park, M. Perrott, M. A. Popović, R. J. Rama, H. I. Smith and G. R. Zhou, "High Speed Analog-to-Digital Conversion with Silicon Photonics," SPIE Conference Photonic West, San Jose, January 2008., SPIE Conference Photonic West, San Jose, January 2009.
20. K. H. Hong, A. Siddiqui, J. Moses, J. Gopinath, J. Hybl, F. O. Ilday, T.Y. Fan and F. X. Kaertner, "Generation of 287-W, 5.5-ps pulses at 78-MHz repetition rate from a cryogenically-cooled Yb:YAG amplifier for OPCPA amplification," Advanced Solid-State Photonics, OSA Topical Meeting, Denver, CO, February 1-5, 2009.
21. S. Rausch, Th. Binhammer, A. Harth, F. X. Kärtner, and U. Morgner, "Femtosecond Field Synthesizer," Advanced Solid-State Photonics, OSA Topical Meeting, Denver, CO, February 1-5, 2009.
22. (*) F. X. Kärtner, "Large Scale, Femtosecond Timing Distribution for X-ray Free Electron Lasers," CFC Workshop, University of California at Los Angeles, UCLA, May 17-20, 2008.
23. J. R. Birge, and F. X. Kärtner, "Design of Optimal Dispersive Mirrors for Femtosecond Enhancement Cavities and Compressors by Minimizing Phase Distortion Power," Conference on Lasers and Electro Optics (CLEO), Baltimore, MD, June 1-5, 2009.
24. J. A. Cox, J. Kim, J. Chen, and F. X. Kärtner, "Long-Term Stable Timing Distribution of an Ultrafast Optical Pulse Train over Multiple Fiber Links with Polarization Maintaining Output," Conference on Lasers and Electro Optics (CLEO), Baltimore, MD, June 1-5, 2009.
25. E. L. Falcão-Filho, V. M. Gkortsas, A. Gordon and F. X. Kärtner, "Conversion efficiency, scaling and global optimization of high harmonic generation," Conference on Lasers and Electro Optics (CLEO), Baltimore, MD, June 1-5, 2009.
26. V.-M. Gkortsas, A. Gordon, C. Jirauschek, C.Wang, L. Kuznetsova, L. Diehl, M. A. Belkin, A. Belyanin, F. Capasso and F. X. Kärtner, "Spatial Hole Burning in Actively Mode-Locked Quantum Cascade Lasers," Conference on Lasers and Electro Optics (CLEO), Baltimore, MD, June 1-5, 2009.
27. K. H. Hong, J. Gopinath, A. Siddiqui, J. Moses, Ch.-J. Lai, J. Hybl, T.Y. Fan and F. X. Kärtner, "High-average-power cryogenically-cooled picosecond Yb:YAG amplifier seeded by a fiber CPA system," Conference on Lasers and Electro Optics (CLEO), Baltimore, MD, June 1-5, 2009.
28. S.-W. Huang, J. Moses, K.-H. Hong, E. L. Falcao-Filho, A. Benedick, J. A. Bolger, B. J. Eggleton, and F. X. Kärtner, "High-Power, Few-Cycle, Phase-Stabilized 2.2- μm Optical Parametric Chirped Pulse Amplifier," Conference on Lasers and Electro Optics (CLEO), Baltimore, MD, June 1-5, 2009.
29. J. Morse, J. Sickler, J. Chen, F. X. Kärtner, and E. P. Ippen, "High Repetition Rate, High Average Power, Femtosecond Erbium Fiber Ring Laser," Conference on Lasers and Electro Optics (CLEO), Baltimore, MD, June 1-5, 2009.

30. J. Moses, C. Manzoni, S-W Huang, G.Cerullo, and F. X. Kärtner, "Multi-Stage Optimization of Ultrabroadband High-Energy Optical Parametric Chirped Pulse Amplification," Conference on Lasers and Electro Optics (CLEO), Baltimore, MD, June 1-5, 2009.
31. A. H. Nejadmalayeri, F. N. C. Wong, T. D. Roberts, P. Battle, and F. X. Kärtner, "Efficient second harmonic generation in the optical telecom S-band using non-segmented PPKTP waveguides," Conference on Lasers and Electro Optics (CLEO), Baltimore, MD, June 1-5, 2009.
32. M. Y. Sander, E. P. Ippen and F. X. Kärtner, "Carrier-Envelope Phase Dynamics of Octave-Spanning Titanium:sapphire Lasers," Conference on Lasers and Electro Optics (CLEO), Baltimore, MD, June 1-5, 2009.
33. A. M. Siddiqui, J. Moses, K.-H. Hong, and F. X. Kärtner, "Strong Bandwidth and Efficiency Improvement by Passive Pulse Shaping in Cavity-Enhanced OPCPA," Conference on Lasers and Electro Optics (CLEO), Baltimore, MD, June 1-5, 2009.
34. H. Byun, D. Pudo, S. Frolov, A. Hanjani, J. Shmulovich, E. P. Ippen, F. X. Kärtner, "Femtosecond passively mode-locked fiber lasers using saturable Bragg reflectors," International Laser Physics Workshop, Barcelona, Spain, July 13 –17, 2009.
35. Edilson L. Falcão-Filho, V. M. Gkortsas, Ariel Gordon and Franz X. Kärtner, "Conversion efficiency and scaling for high harmonic generation: an analytical approach," Conference on Attosecond Science, Kansas State University, Manhattan, KS, July 28 – August 1, 2009.
36. F. X. Kärtner, Tutorial on "Carrier-Envelope Phase Control, Conference on Ultrafast Optics and High Fields Short Wavelength," (UFO VII – HFSW XIII), Arcachon, France, August 31 – September 4, 2009.
37. F. X. Kärtner, "Octave-Spanning Ti:sapphire Lasers and Carrier-Envelope Phase Control," Conference on Attosecond Science, Kansas State University, Manhattan, KS, July 28 – August 1, 2009.
38. F. X. Kärtner, "High Power Ultrafast Laser Systems for EUV and X-ray Sources," Keynote presented at Directed Energy Professional Society Workshop, Newton, MA, June 30 – July 2, 2009.

Theses

1. J. Birge, Methods for Engineering Sub-Two-Cycle Mode-Locked Lasers, PhD Thesis, Dept. of Electrical Engineering and Computer Science, MIT, 2009.
2. G. Abraham, Theory and design of high-index-contrast microphotonic circuits, Ph.D. Thesis, MIT, 2008.